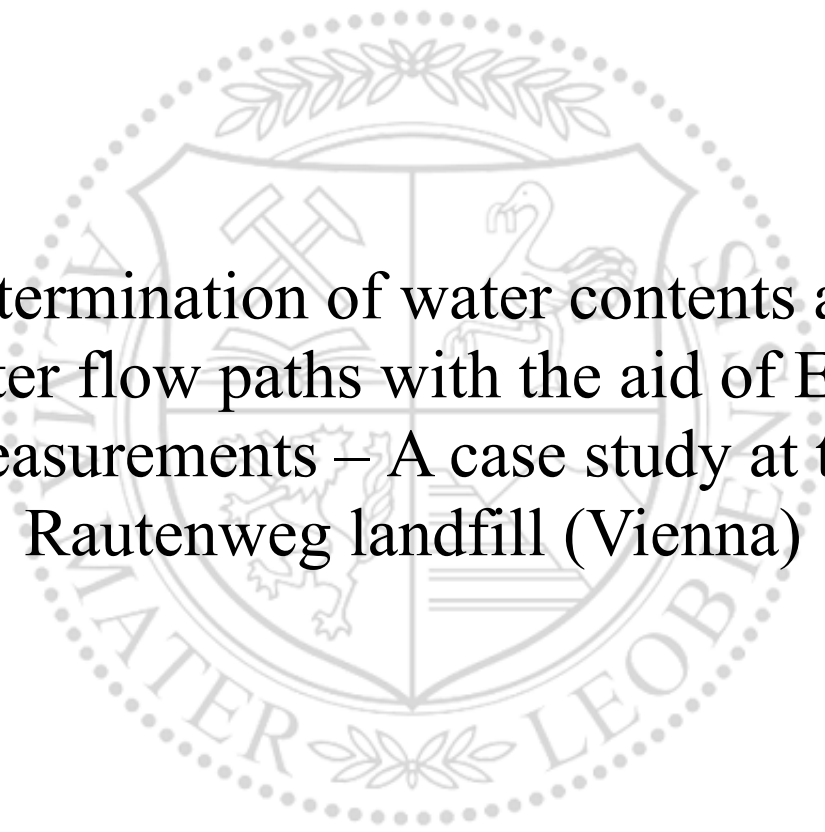




Chair of Applied Geophysics

Master's Thesis



Determination of water contents and
water flow paths with the aid of ERT
measurements – A case study at the
Rautenweg landfill (Vienna)

Oliver Pöschl, BSc

March 2019

EIDESSTATTLICHE ERKLÄRUNG

Ich erkläre an Eides statt, dass ich diese Arbeit selbständig verfasst, andere als die angegebenen Quellen und Hilfsmittel nicht benutzt, und mich auch sonst keiner unerlaubten Hilfsmittel bedient habe.

Ich erkläre, dass ich die Richtlinien des Senats der Montanuniversität Leoben zu "Gute wissenschaftliche Praxis" gelesen, verstanden und befolgt habe.

Weiters erkläre ich, dass die elektronische und gedruckte Version der eingereichten wissenschaftlichen Abschlussarbeit formal und inhaltlich identisch sind.

Datum 08.03.2019



Unterschrift Verfasser/in
Oliver, Pöschl
Matrikelnummer: 01235248

Acknowledgment

During my Master thesis project, several people supported me to whom I wish to express my gratitude in this way.

First, I would like to thank my supervisor Ao. Prof. Dr. Robert Scholger, which supported me in the measurements, in the evaluation of the data and lend always a sympathetic ear to me. Further, I would like to say thank you to all people of the Chair of Applied Geophysics at the “Montanuniversität Leoben” who supported me during my field measurements, with organizational matters and all other things.

Other thanks go to the Chair of Waste Processing Technology and Waste Management at the “Montanuniversität Leoben” and to the staff of the MA 48, which made the measurements at the Rautenweg landfill possible.

Special thanks go to my entire family for their support throughout my studies. Here I would like to thank in particular my grandparents, where I have lived during my time at the university.

Finally, a heartfelt thanks to Vanessa and Alexander, who proofread my work with much patience.

Kurzfassung

Das Ziel dieser Masterarbeit ist es den Wassergehalt auf Mülldeponien, sowie die Ausbreitung der Wasserwegigkeiten bei gleichzeitigem Einbringen von Wasser in den Untergrund zu ermitteln. Zu diesem Zweck wurde das Messverfahren der Geoelektrik (ERT – electrical resistivity tomography) gewählt.

Der erste Teil der Messungen erfolgte auf dem Gelände des Paläomagnetiklabors der Montanuniversität Leoben in Gams. Aufgrund der Kenntnis über die Zusammensetzung des Untergrundes, eignet es sich ideal für die Messungen. Mittels dieser Messungen konnte die optimale Elektrodenanordnung und Messsystemparameterkonfiguration ermittelt werden, welche bei den weiteren Messungen auf der Mülldeponie Rautenweg Verwendung fand. Mit diesen sollte die ursprüngliche Fragestellung, nämlich die Bestimmung des Wassergehaltes und die Verfolgbarkeit von Wasserwegigkeiten, beantwortet werden.

Die Ergebnisse aus Gams zeigen, dass die Wenner Elektroden Anordnung die am besten geeignetste ist. Auch die ursprünglichen Ziele dieser Masterarbeit konnten, mit kleinen Einschränkungen, mittels der Messungen auf der Deponie Rautenweg erreicht werden. Diese Einschränkungen brachten weitere Erkenntnisse über die Wichtigkeit verschiedener Einflussfaktoren für die qualitative Bestimmung des Wassergehaltes und Wasserwegigkeiten für zukünftige Projekte. Die Kenntnis über die Temperatur und Leitfähigkeit innerhalb des Deponiekörpers, ein Vorhandensein von in-situ Müllproben und eine ausreichend große Differenz zwischen der Leitfähigkeit des Deponiekörpers und eingebrachtem Wassers ist essentiell.

Abstract

The aim of this Master thesis is the determination of water contents within landfills as well as the monitoring of water flow paths during a focused irrigation. For this purpose, the geoelectrical measuring method (ERT - electrical resistivity tomography) was chosen.

The first part of the measurements was performed at the area of the paleomagnetic laboratory of the "Montanuniversität Leoben" in Gams. Due to the knowledge of the composition of the subsurface, it is ideal for the measurements. By means of these measurements, the optimal electrode and measuring system parameter configuration could be determined, which was used during the measurements at the Rautenweg landfill. There, the purpose was to identify the original task, namely the determination of water content and the traceability of water flow paths.

The results from Gams indicate that the Wenner electrode configuration is the most suitable. Also, the original objectives of this Master's thesis could be determined by means of measurements at the Rautenweg landfill, with some restrictions. These limitations provided further findings in the importance of various factors influencing the qualitative determination of water contents and water flow paths for prospective projects. Therefore, knowledge about the temperature and conductivity within landfills, the presence of in-situ waste samples, and a sufficiently large difference between the conductivity of the landfill body and the introduced water, is essential.

Table of Contents

Acknowledgment.....	I
Kurzfassung	II
Abstract	III
Table of Contents	IV
1 Introduction.....	1
2 Basic Principles	3
2.1 Landfill characterization	3
2.2 Geoelectrical methods	4
2.2.1 DC resistivity method	5
2.2.2 Induced polarization (IP) method	13
3 Field measurements.....	16
3.1 Material and methods.....	16
3.1.1 Geoelectrical measurement device	16
3.1.2 Topographical measurement device (GPS)	17
3.1.3 Inversion software.....	18
3.2 Test site Gams	20
3.2.1 Quality check of the 4point light 10W device	21
3.2.2 Statistical evaluation	23
3.2.3 Pole-Dipole array comparison.....	27
3.2.4 Comparison of the Wenner-, Schlumberger- and Dipole-Dipole array	35
3.2.5 Well experiment Gams.....	38
3.2.6 Conclusion of the measurements in Gams	44
3.3 Rautenweg landfill.....	45
3.3.1 General site description	45

Table of Contents

3.3.2	Survey campaigns and measurement device settings	48
3.3.3	Evaluation of raw data – measurement errors and apparent resistivities	50
3.3.3.1	Statistical evaluation	50
3.3.3.2	Effects of gas wells on the measurements.....	51
3.3.4	Inversion results	53
3.3.5	Conductivity display of the inversion results	56
3.3.6	Time-Lapse measurements	66
3.3.7	Conclusions of the measurements at the Rautenweg landfill	79
4	Results / Discussion	81
5	Summary / Outlook	85
6	References.....	86
7	List of Figures.....	90
8	List of Tables.....	97
9	Appendix A	99
9.1	Tables	99
9.2	Figures	100

1 Introduction

The knowledge of water contents within landfills is of high interest for waste managements, since it has one of the strongest influences on biogas production (Rettenberger, 1992). Biogas production occurs at landfills when wet municipal solid waste is biodegrading through bacteria. This gas is on the one hand a greenhouse gas and must be collected and on the other hand the collected gas, since it consists of about 50 % methane, is a potential renewable energy source. At the Rautenweg landfill this production is decaying, because it has a surface seal and thus, only limited water circulation is possible. Therefore, by means of a focused irrigation of selected landfill areas the microbial activities should be enhanced to increase the biogas production again.

The common methods for determining water contents require in-situ waste samples and for these costly boreholes are mandatory. Geoelectrical methods are a good cost effective alternative, since with them it is possible to determine wet and dry areas within landfills in an even bigger scale. Therefore, the goals of this thesis are to identify, with a 2-D ERT survey, such areas within the Rautenweg landfill and to monitor the water flow paths of the focused irrigation.

To achieve these goals, this thesis is divided into two main measurement campaigns: one for auxiliary measurements and the other for the original problem.

Within the first campaign the aim was to identify the best settings for the measurements at the Rautenweg landfill. Hence several measurements were performed at the paleomagnetic laboratory of the “Montanuniversität Leoben” in Gams. This offers optimal conditions, since the composition of the subsurface is known. The measurements included the determination of the best electrode array and of the optimal measuring instrument parameters for the landfill monitoring and measurements. If some array types display measurement errors, an additional attempt was made to determine the source of the errors. Further, a small-scale monitoring experiment was carried out to decide if such a monitoring is feasible at the landfill.

The second campaign includes the measurements to answer the original problem at the Rautenweg landfill. Additionally, these measurements were subdivided into two measurement campaigns. The ambition of the first one was to identify wet and dry areas within the landfill body. Thus, in summary nine profiles were measured over the whole landfill area. Based on these measurements three profiles, with dry subsurface areas around the gas wells, were selected for the monitoring experiment which are assigned to the second campaign.

The results of the measurements are displayed in form of tables, Excel plots and 2-dimensional subsurface sections.

2 Basic Principles

2.1 Landfill characterization

Landfills are generally places where municipal solid waste (MSW) is dumped. During operation and after, there should be no hazard to public health or to the environment (Hermozilha et al., 2010). To guarantee this, after Frid et al. (2010) leachate, biogas, chemical and water samples are taken from a specific network (drilled wells and landfill surface).

Biogas or landfill gas (LFG) is a potential renewable energy source and essentially a greenhouse gas. The composition consists mainly of methane (CH₄) (50 %), carbon dioxide (CO₂) (45 %) and other minor components (Ahmed et al., 2014). While methane and carbon dioxide are two of the foremost greenhouse gases (Majdinasab et al., 2017), MSW landfills play a major role in the global carbon cycle and therefore in the discussion of climate change (Tintner et al., 2012). On the other hand, methane can be used as a renewable energy source. Each ton of MSW produces theoretically around 200 m³ of methane gas, which is in real landfills much smaller with ranges from 40 m³ to 80 m³ per ton MSW (Themelis and Ulloa, 2007). The landfill gas (LFG) is produced from anaerobic biodegradation of municipal solid wastes. After Kumar et al. (2004) the generation of LFG occurs in five phases: initial adjustment phase, transition phase, acid phase, fermentation phase and maturation phase. Each phase is characterized by different conditions (anaerobic or aerobic) and different amount of CO₂ and CH₄ production. The amount of gas production is controlled by various parameters such as pH, temperature and water content (Kumar et al., 2004). Of these parameters, water content is the most important factor influencing gas production. In the range of 20 % to 60 % water content, a small increase of a few per cent causes a significant increase in methane production (Rettenberger, 1992). Above 60 % water content, gas production would be ideal. However, in real landfills the values are between 15 % and 50 % (Rettenberger, 1992). Also, heat is generated by the biodegradation of methane bacteria, which leads to typical temperature ranges in landfills from 20 °C to 40 °C with some heat-nests up to 55 °C (Rettenberger, 1992). This range corresponds well with the optimal living conditions (30 °C to 40 °C) of the methane producing bacteria.

To predict the quantity of methane generation these parameters are monitored via boreholes. However, there are uncertainties in LFG generation rates, which lead to difficulties while operating an LFG collecting system (Majdinasab et al., 2017). Due to the reasons mentioned above the characterization of the subsurface and monitoring of LFG is of high interest for waste managements. Common control methods such as boreholes can only provide small scale estimates and are expensive. Geophysical methods are a cost effective alternative and can additionally provide information for a larger area.

2.2 Geoelectrical methods

In the last years, the importance of geophysical methods for landfill characterization has increased. One big advantage of these methods is that they can cover a larger area and are non-invasive. Methods such as geoelectrical tomography, refraction seismics, electromagnetic- and ground penetrating radar (GPR) profiles in combination with in-situ measurements allow the characterization of the landfills subsurface (Georgaki et al., 2008). After Georgaki et al. (2008) the geoelectrical method is the most suitable for the landfill characterization, because most waste materials and liquids are conductive (Bernstone et al., 2000).

There are a wide number of geoelectrical methods, but only three of them are commonly used in subsurface characterization and monitoring of hydrological features (Revil et al., 2012). One of them is a passive method, the self-potential (SP), and the other two are active methods, the DC resistivity and induced polarization (IP) method. The two active methods measure electrical potentials associated with the flow of currents in the subsurface. Or in other words: they measure the spatial distribution of resistivity or conductivity. The IP method is an extension of the DC resistivity method which determines only resistivity. In addition, the IP method measures also the capacitive properties (Binley and Kemna, 2005) of the subsurface. With this parameter, it is possible to quantify the electrical polarizability of the subsurface and make further statements about lithology and grain surface chemistry (Binley and Kemna, 2005). The goal of all geoelectrical methods is to characterize the subsurface in terms of structure and lithology with the measured parameters. To obtain

more accurate solutions, additional parameters such as geology or borehole information should be used.

2.2.1 DC resistivity method

Theoretical background and data acquisition

With the DC resistivity method, the spatial variation of resistivity ρ (or the reciprocal – conductivity σ) is measured. For each measurement four stainless steel electrodes (Binley and Kemna, 2005; Revil et al., 2012) are used. Two electrodes (current electrodes) form the current dipole, and the other two (potential electrodes), measure the potential difference (voltage) in the subsurface current flow between the current electrodes (Fig. 1). By convention the current electrodes are named A and B, and the potential electrodes M and N.

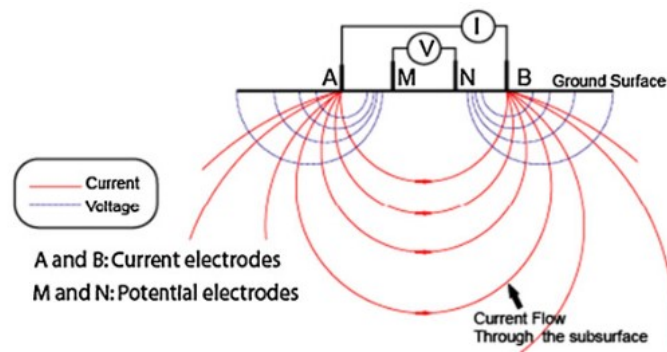


Fig. 1: Four electrode-measurement arrangement: Two current electrodes (A and B) and two potential electrodes (M and N) (modified after Revil et al., 2012).

By applying Ohms Law Eq.(1) the resistance R is obtained. U is the voltage measured between M and N and I is the strength of the injected current.

$$R = \frac{U}{I} [\Omega] \quad (1)$$

The resistivity across a cylindrical core sample can be calculated after Eq.(2), where R is the resistance, A the cross section, L the length of the cylinder and A/L the geometric factor, which is represented in its general form in Eq.(3).

$$\rho = \frac{R * A}{L} [\Omega m] \quad (2)$$

$$k_{geom} = 2\pi \left(\frac{1}{x_{AM}} - \frac{1}{x_{BM}} - \frac{1}{x_{AN}} - \frac{1}{x_{BN}} \right)^{-1} \quad (3)$$

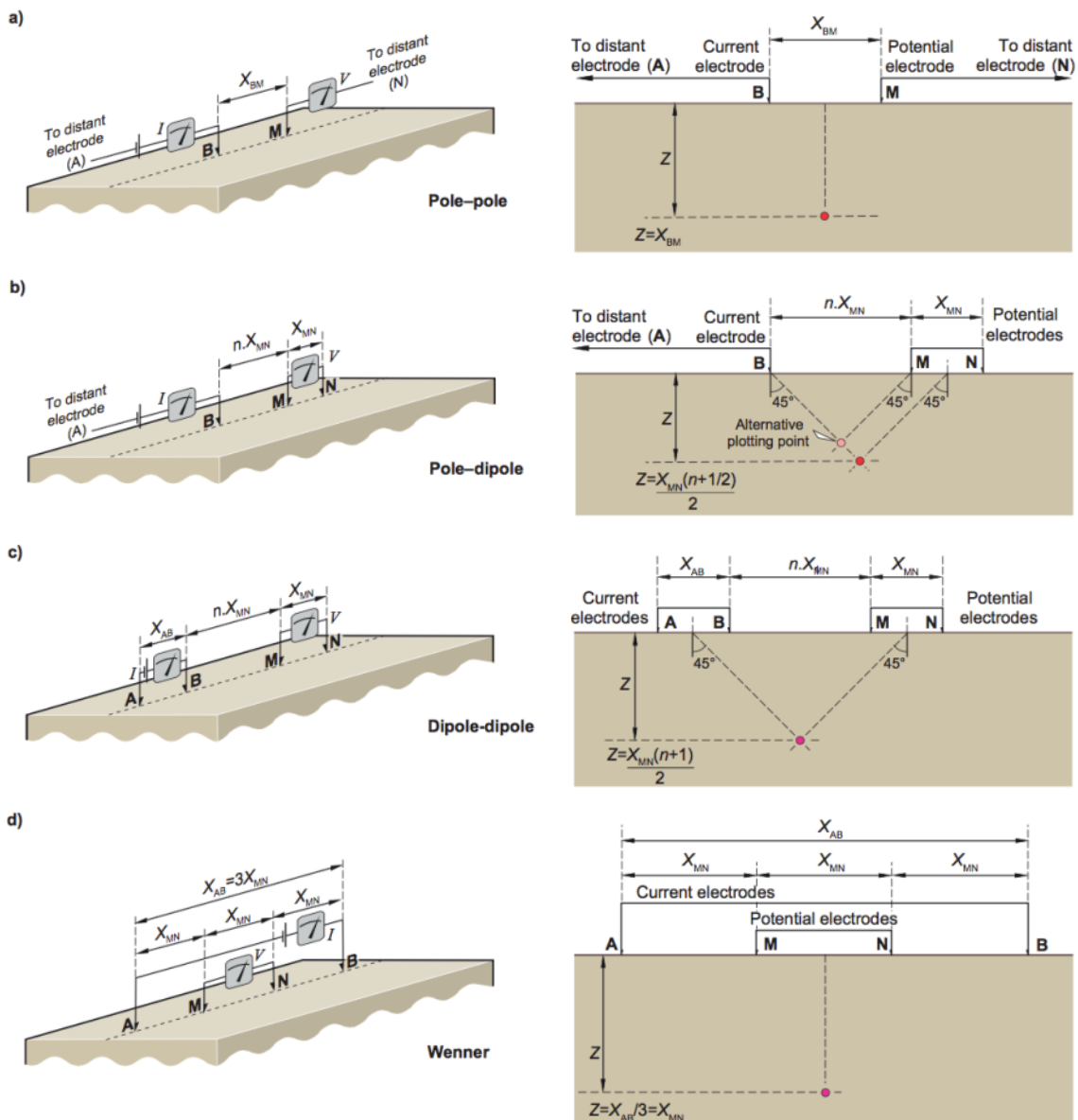
As visible in Eq.(3) the geometric factor k_{geom} depends on the position of the electrodes (Tab. 1).

Surface arrays	Geometric factor (k_{geom})
Pole-pole	$2\pi X_{BM}$
Pole-dipole	$2\pi n(n+1)X_{MN}$
Dipole-dipole	$\pi n(n+1)(n+2)X_{MN}$
Wenner	$2\pi X_{MN}$
Schlumberger	$\pi \frac{(X_{AB}/2)^2}{X_{MN}}, X_{MN} \leq X_{AB}/20$

Tab. 1: Geometric factors for different electrodes arrays (Dentith and Mudge, 2014).

The position of the electrodes is also known as an electrode array. There are many different numbers of electrode arrays in literature (Revil et al., 2012), but only five of them (pole – pole, dipole – pole, dipole – dipole, Wenner and Schlumberger (Fig. 2)) are commonly used (Dentith and Mudge, 2014). Each of these array configurations has its advantages and disadvantages. In general (Loke, 2015), the Wenner array is relatively sensitive to vertical changes and less to horizontal changes in the subsurface. Because of this property, the Wenner array is good in resolving horizontal structures. It has a moderate depth of investigation, but the strongest signal strength compared to all other arrays. This is an important property, while surveying in a noisy area. The Schlumberger array is similar to the Wenner array, but has a lower signal to noise ratio and is poorer in resolving horizontal structures. In comparison to the Wenner and Schlumberger array, the dipole-dipole array is very sensitive to horizontal changes in resistivity and so good for mapping vertical structures (Loke, 2015). One disadvantage of this array is the very low signal strength, which can cause problems in noisy areas. Also, the depth of investigation is smaller compared to the Wenner array, but the EM coupling between the current and potential circuits is low (Loke, 2015). Thus this array is widely used in IP surveys. For the pole-dipole array, the signal strength is higher than the dipole-dipole array, but lower than the Wenner and Schlumberger array.

Like the dipole-dipole array the pole-dipole array is more sensitive to horizontal changes. Since the pole-dipole array requires a remote electrode, it is an asymmetrical array. In some cases, this can influence the modelled resistivities (Loke, 2015). Otherwise the remote electrode is responsible for a greater depth of investigation compared to the other arrays. The pole-pole array is not widely used, because the ideal configuration with just one current and potential electrode does not subsist (Loke, 2015). As a conclusion, the dipole-dipole and pole – dipole arrays are good in resolving vertical structures in a non-noisy area. If a good horizontal resolution in a noisy area is required, the Wenner- or Schlumberger array is preferred.



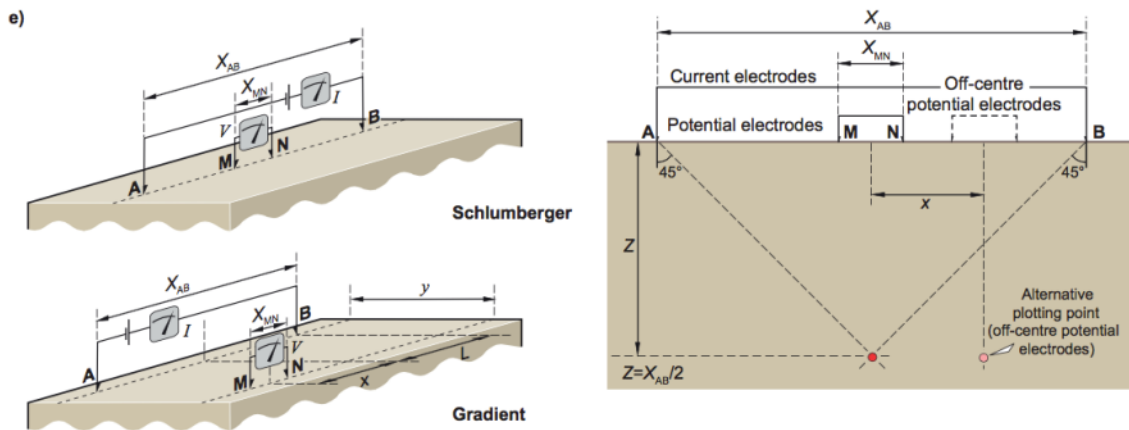


Fig. 2: The commonly used electrode arrays and plotting conventions for soundings and pseudosections: (a) pole–pole, (b) pole–dipole, (c) dipole–dipole, (d) Wenner, (e) Schlumberger and gradient arrays (Dentith and Mudge, 2014).

Inversion of ERT data

In general, measurements are performed in a heterogeneous subsurface. The product of the resistivity and the geometric factor leads therefore to the apparent resistivity ρ_a . For a homogeneous ground the apparent resistivity is equal to the true resistivity. Likely this is not the case in nature and thus the true resistivity is only obtained after inversion algorithms. Inversion algorithms search for a true resistivity model that explains the measured field data (Revil et al., 2012). In geoelectrical prospecting typically a smoothness based inversion scheme is used (Binley and Kemna, 2005). However there are others, but all have in common that they modify an initial model so that the difference between the model response (synthetic data) and the observed data values are reduced. The accuracy of the difference is expressed in terms of the root mean square (RMS) error. In Fig. 3 one example of an inversion process is displayed, where the pseudosection indicates the measured apparent resistivity and the tomogram the modelled resistivity. In the tomogram, the heterogeneities look smoother. This problem can be solved by modification of the regularization term (Blaschek et al., 2008).

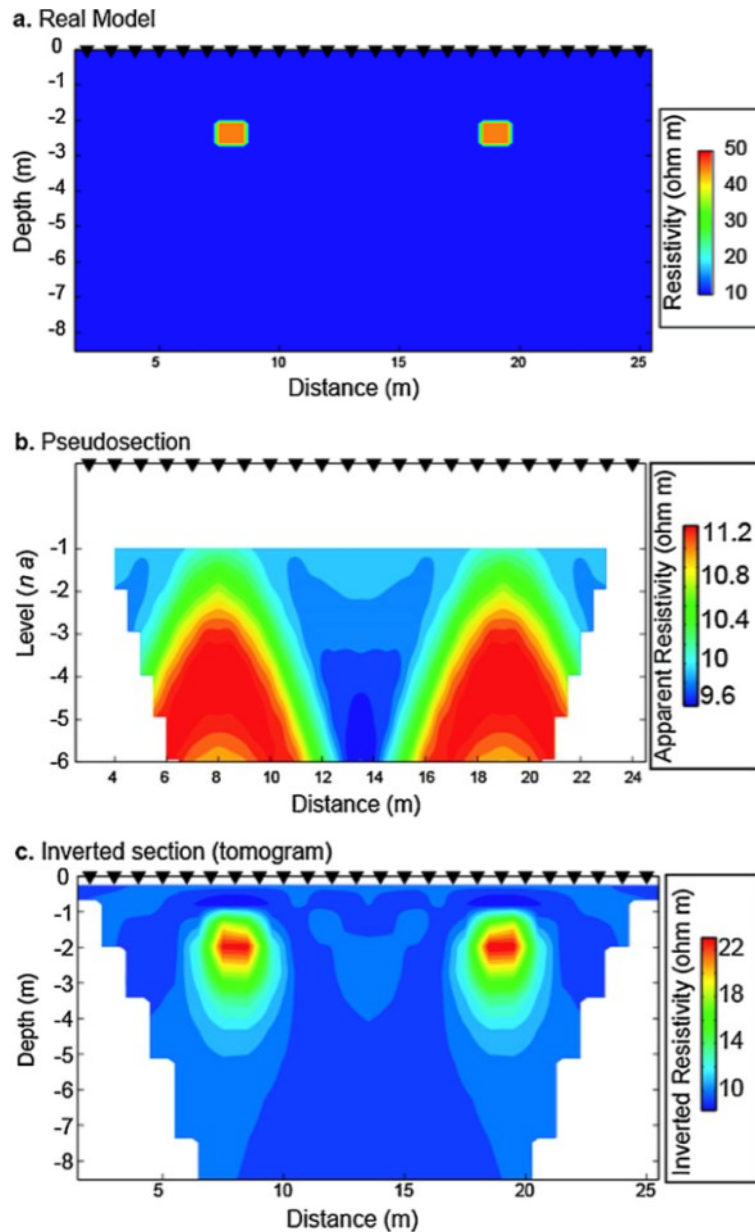


Fig. 3: Example for an electrical resistivity tomography measurement. (a) real model, (b) pseudosection with apparent resistivity and (c) the inverted section. The triangles indicate the positions of the electrodes (Revil et al., 2012).

Additionally the pseudosection has a form of an inverted “V” shape, also known as pants-legs structure. This occurs, because the plotting of the responses below a zone with anomalous electrical properties extends diagonally downwards due the array geometry (Fig. 4) (Dentith and Mudge, 2014).

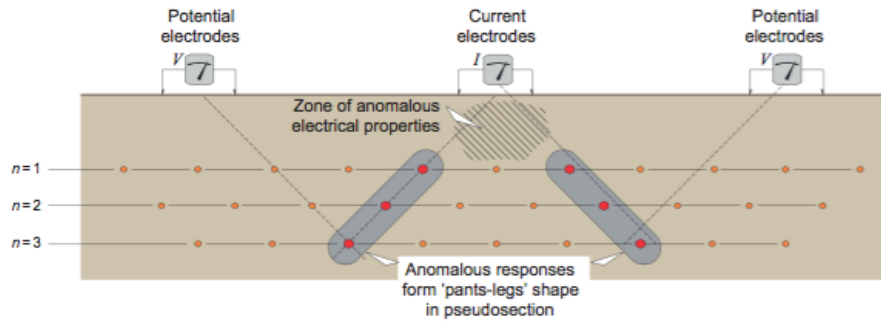


Fig. 4: Explanation of the pants-legs response using a dipole-dipole array (Dentith and Mudge, 2014).

Resistivity and hydrological properties

Natural rocks are commonly a two phase composite, consisting of a pore space (may be filled with fluids) and a solid mineral phase (generally nonconductive with some exceptions – e.g.: metallic grains). In porous rocks or materials, the conductivity is mainly controlled by the pore fluid and therefore generally higher than in igneous rocks. Water is the most common pore fluid. Pure water is a bad conductor, but naturally occurring water contains salts which leads to a good conductivity.

Waste materials are usually porous materials and thus the resistivity is commonly dominated by the leachate water. In general, the resistivities of such materials are low, since the leachate water dissolves many salts from the landfill. Typical waste materials have resistivity ranges from 15-70 Ωm and leachate water from 1-4 Ωm . If materials are accumulated they can produce resistivity anomalies. Bernstone et al. (2000) divided such anomalies into six classes: metals, ash from incineration plants, gardening waste, chemicals, plastics and waste in plastic bags. In Fig. 5 some resistivity values of typical waste materials and leachate waters are displayed.

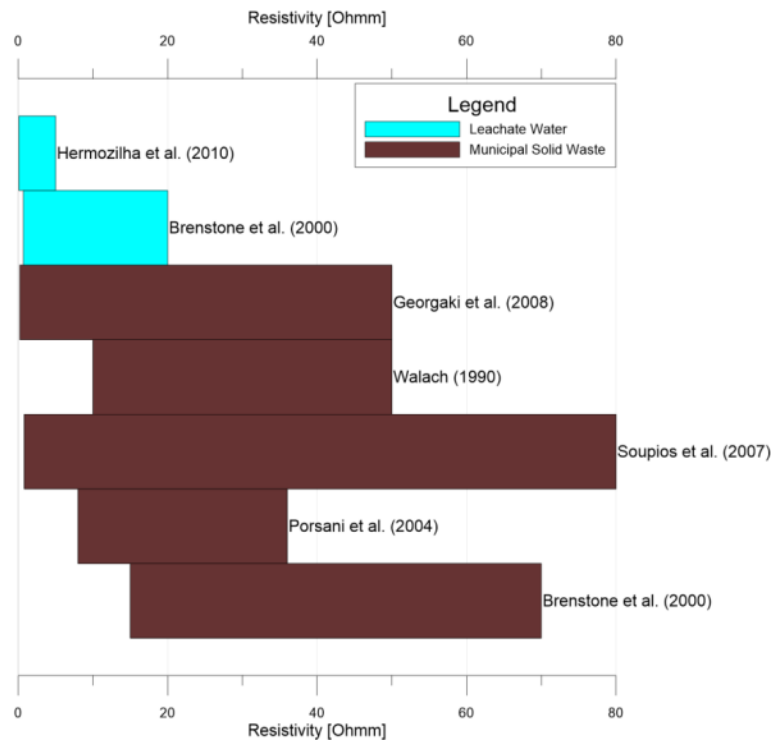


Fig. 5: Resistivity ranges of typical waste materials and leachate waters from various publications (Bernstone et al., 2000; Georgaki et al., 2008; Hermozilha et al., 2010; Porsani et al., 2004; Souplos et al., 2007; Walach, 1990).

Archie (1942) found out, that the resistivity of a fluid is proportional to the resistivity of a clean medium (shale and clay free) saturated with the fluid. This is defined by the first Archie equation Eq.(4),

$$F = \frac{\rho_0}{\rho_w} = \frac{a}{\phi^m} \quad (4)$$

where F is the formation factor, ρ_0 the resistivity of the fully saturated rock and ρ_w of the pore fluid, a is a constant, m the cementation exponent and Φ the porosity.

If the pore space is partly saturated the second Archie equation Eq. (5) is valid,

$$S_w = \sqrt[n]{\frac{\rho_w * a}{\rho_t * \phi^m}} \quad (5)$$

where S_w is the water saturation, ρ_t the resistivity of the partly saturated rock and n the saturation exponent.

Grellier et al. (2006) simplified the above relationship for MSW landfills to:

$$\rho = \rho_w a \theta^{-m} \quad (6)$$

where ρ the interpreted electrical resistivity, ρ_w the resistivity of the leachate water, a and m empirical parameters and θ the volumetric water content. In the field measurements from Grellier et al. (2006) the value for the parameter a was fixed to 0.75 and the values for m ranging from 1.6 up to 2.15 depending on the different waste types.

Applications and Errors

ERT surveys have been used for a broad variety of problems. Since the conductivity is mainly influenced by the pore fluid chemistry, the water saturation and the lithology (Binley and Kemna, 2005), these methods are commonly used in hydrogeology. After Loke et al. (2013) other applications are: mineral exploration, environmental studies, agriculture and soil sciences, engineering studies, archaeological applications and waterborne resistivity. The time-lapse mode (continuous repeat measurements at the same position over long times) is a great tool for monitoring water flow paths (Revil et al., 2012). Typically, this monitoring is performed at long term processes. Tildy et al. (2017) demonstrated a process of salt tracer propagation monitoring in a complex geological setting for a short term.

Errors in the measured data and the resulting resistivity image can occur from the measurement device, poor electrode contact or electrode polarization (Loke et al., 2013). Another type of error can appear in vertical electrical soundings, which search especially for the vertical variation in the electrical properties. These surveys are affected by the variation of the resistivity and thickness of the upper layer (Dentith and Mudge, 2014). Fig. 6 demonstrates that a high resistivity upper layer (e.g.: concrete) is better for the image quality of the lower layer. This is the case since the boundary between them is sharper with a resistivity of 500 Ωm for the upper layer compared with a resistivity of 5 Ωm .

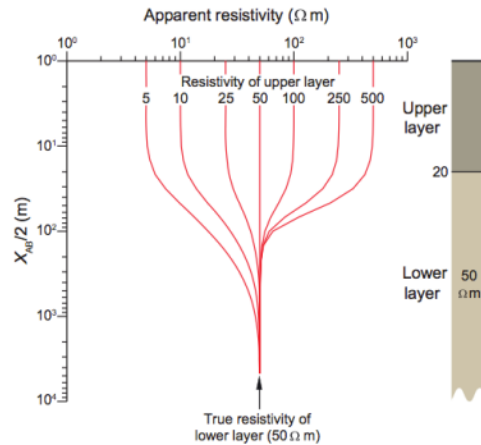


Fig. 6: Vertical electrical sounding curve for a constant thickness and variable resistivity of the upper layer (Dentith and Mudge, 2014).

Probably the strongest influence on electrical conductivity are changes in temperature of the subsurface. Hayley et al. (2007) performed field measurements during the May 2006 with temperature changes in the upper meter of approximately 3.5°C which leads to maximum and minimum corrections that differ by 6.5%. In landfills these variations are even higher, which can be seen by the study from Yesiller and Hanson (2003). In their measurements, the variations are ranging from seasonal temperature variations (within 9 m depth) up to a maximum of 60°C at a depth of 28 m. Generally, the deviation is about 2% change per degree. Therefore, during interpretation of ERT data temperature changes must be accounted.

2.2.2 Induced polarization (IP) method

Additional to the resistance, the capacitance of the subsurface is measured with IP surveys. The IP effect is mainly controlled by processes at the fluid-grain interface, whereas the resistivity of the soil is controlled by the pore fluid (Binley and Kemna, 2005). For the measurements in the field, a four-electrode arrangement is used. Therefore, the same electrode-arrays as for the DC resistivity method are valid (Fig. 2). However, they are not equivalent in terms of electromagnetic coupling effects, signal to noise ratio and electrode polarization (Binley and Kemna, 2005; Revil et al., 2012). To avoid electrode polarization, potential electrodes should be non-polarizing. Dipole-dipole arrays are often used for

ground surveys to obtain minimum coupling effects (Binley and Kemna, 2005). To enhance the signal to noise ratio, injected currents must be much higher than in DC methods.

IP surveys are measured with a DC current either in time-domain or frequency-domain mode (Binley and Kemna, 2005; Dentith and Mudge, 2014; Revil et al., 2012). In the time-domain mode the current is injected until a steady value (primary voltage V_p) and suddenly stopped. By turning off the current, first an initial sharp drop in the potential occurs by following a gradual decay (secondary voltage V_s). This gradual decay is measured and depends on the electrical charge polarization (Binley and Kemna, 2005). In comparison, the frequency-domain measures a phase shifted potential relative to an alternating injected current. In Fig. 7 both domains are represented after Dentith and Mudge (2014).

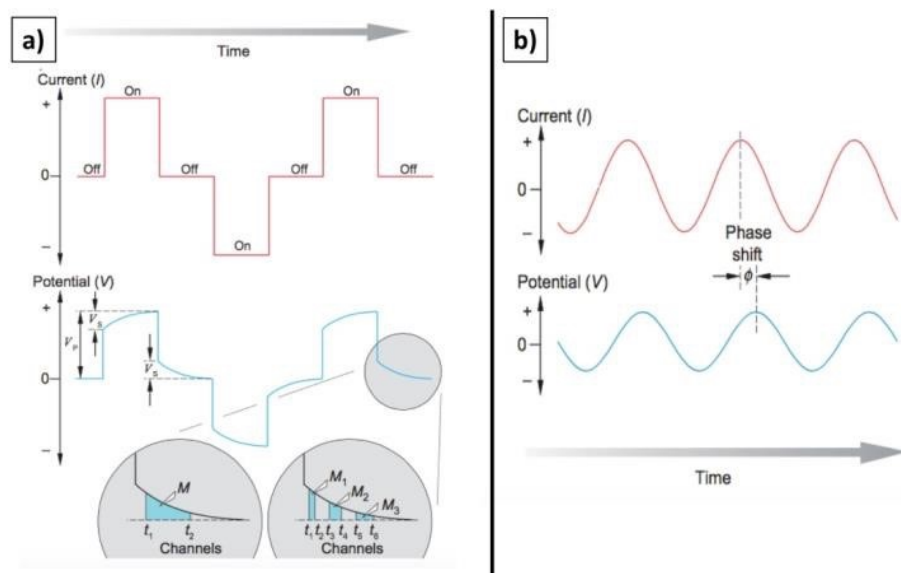


Fig. 7: (a) Time-domain measurement with small rise and decay of the secondary voltage produced by polarization effects. (b) Frequency-domain measurement with the sine wave signal and the phase shifted obtained potential (Modified after Dentith and Mudge (2014)).

When an external electrical field is applied to a rock, charges (electrons or ions) are transported and accumulated (reversibly) in rocks or soils causing induced polarization (Kemna et al., 2012). After Dentith and Mudge (2014) two main polarization mechanisms, membrane (electrolytic) polarization (Marshall and Madden, 1959; Titov et al., 2002; Vinegar and Waxman, 1984) (Fig. 8a) and grain (electrode) polarization (Merriam, 2007) (Fig. 8b), occur. Kemna et al. (2012) pointed out three main mechanisms: the Maxwell-Wagner polarization (Chelidze and Guéguen, 1999; Chen and Or, 2006), the polarization of the Stern layer (inner part of the electrical double layer (EDL)) (Leroy et al., 2008; Revil et al., 2012;

Vaudelet et al., 2011) and the polarization of the diffuse layer (outer part of the EDL) (De Lima and Sharma, 1992).

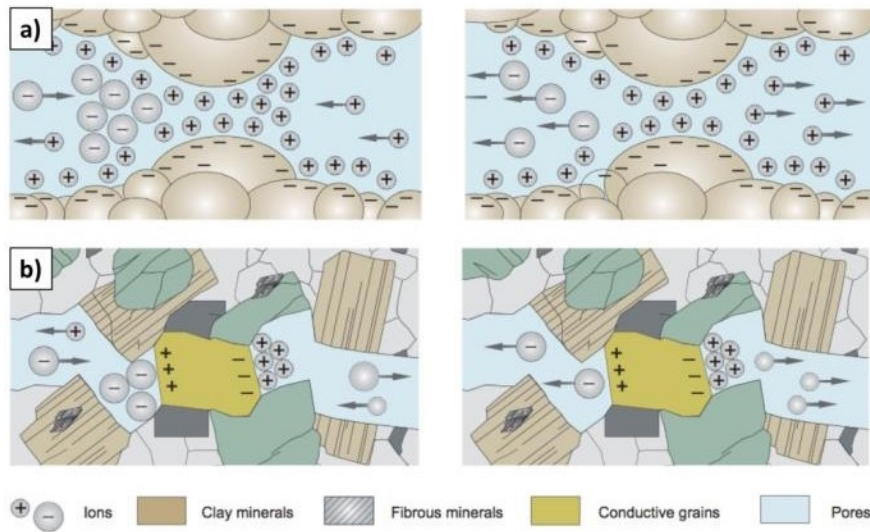


Fig. 8: Capacitive properties during charging and discharging of electrical charges. (a) Membrane polarization and (b) grain polarization (Modified after Dentith and Mudge (2014)).

The IP method is classically used for the exploration of ore bodies (porphyry and massive sulfide deposits) (Kemna et al., 2012). Other applications are: environmental studies (detection of contaminates), biological activities in soils, lithological characterization, geochemical and hydrological processes (Revil et al., 2012). For example Ghorbani et al. (2008) monitored a water infiltration test while using IP measurements.

3 Field measurements

The aim of this chapter is to analyse the different field campaign measurements and give an overview about the used materials and methods. In the first part of the field measurements the goal was to identify the best setup and suitability for the Rautenweg landfill survey campaign. These measurements were carried out in Gams, as a small-scale model experiment (approximately 1:7) in real nature under known subsurface conditions. The second part of the field measurements deals with the Rautenweg landfill survey, which is divided into two campaigns. The first one was used to identify wet and dry areas to subsequently irrigate the dry areas within the second campaign and monitor (time-lapse measurements) the water flow paths of the introduced water.

3.1 Material and methods

3.1.1 Geoelectrical measurement device

All electrical resistivity tomography (ERT) measurements were carried out with the 4point light 10W device from Lippmann geophysical instruments, which is a high precision instrument for ground resistivity determination. Also, it is transmitter and receiver at the same time. The 4point light 10W instrument is an AC device, but produces constant output currents. Therefore, it is possible measuring resistivity and IP effects at the same time. This is feasible because the receiver records the potential difference and the phase shift. Furthermore, different frequencies are selectable. A notebook was directly connected to the instrument and GeoTest software was used for remote controlling of the device. ERT surveys were performed using 100 electrodes and active boxes (Fig. 9b) for multi electrodes surveys. In Fig. 9a the classical ERT setup, with the measurement device and notebook, is displayed.

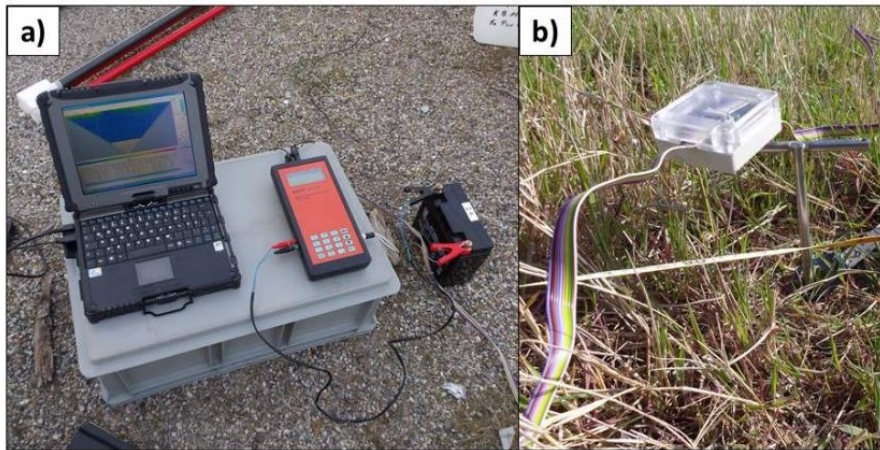


Fig. 9: (a) 4point light 10W instrument (right side) with the remote controlling unit and power supply (left side). (b) Active switch box for multi electrodes surveys.

3.1.2 Topographical measurement device (GPS)

To obtain the exact position in space of the profiles at the Rautenweg landfill a global positioning system (GPS) survey in the real time kinematic (RTK) mode was performed. One big advantage of this mode is that data processing occurs directly in the field. Therefore, the receiver 4700 in combination with the TSC1 data collector from Trimble Navigation Limited was used. The base receiver acts as a fixed base station (Fig. 10a) and transmits correction data, via a radio link, to the rover (TSC1 data collector) (Fig. 10b). Generally, while performing a RTK survey a minimum number of five satellites are needed to achieve accuracies below 5 cm.

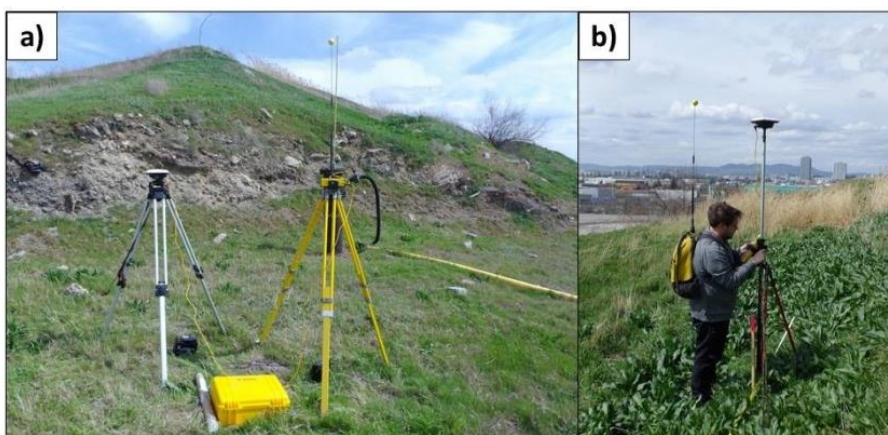


Fig. 10: (a) Base station with receiver and radio link. (b) Moving rover during measurements.

3.1.3 Inversion software

For the inversion of the ERT data the software RES2DINVx64 from Geotomo software (Loke, 2017) and the software package DC2DInvRes from Thomas Günther (Günther, 2007) were used. On one hand with the DC2DInvRes software package it is possible to use different inversion algorithms and parameters. On the other hand, RES2DINVx64 will automatically determine a two-dimensional resistivity model of the subsurface from the measured data. The 2D model consists of many rectangular blocks. To calculate the apparent resistivity values a finite-difference (Dey and Morrison, 1979a, 1979b) or finite-element (Silvester and Ferrari, 1996) modelling subroutine was used (Loke, 2017). The inversion routine of the program, which calculates the resistivity of the 2D model blocks, is based on the smoothness-constrained least-squares method (deGroot-Hedlin and Constable, 1990). The mathematical expression is given by

$$(J^T J + \lambda F) \Delta q_k = J^T g - \lambda F q_k \quad (7)$$

where F is given by

$$F = \alpha_x C_x^T C_x + \alpha_z C_z^T C_z \quad (8)$$

and C_x is the horizontal roughness filter, C_z the vertical roughness filter, α_x, α_z the relative weights given to the roughness filters, J the Jacobian matrix of partial derivatives, J^T the transpose of J , λ the damping factor, Δq the model change vector and g the data misfit vector. After Loke (2017) one advantage of this method is that the damping factor and roughness filters can be adjusted to suit different types of data.

For the time-lapse inversion, the program RES2DINVx64 uses the equation after Kim et al. (2009):

$$[J_i^T J_i + \lambda(F + \alpha M^T R_t M)] \Delta q_k = J_i^T g_i - \lambda(F + \alpha M^T R_t M) q_k \quad (9)$$

This equation represents a four dimensional (4-D) least-squares inversion algorithm which define the subsurface in a space-time domain (Kim et al., 2009). One advantage is that it

propagates no inversion artefacts between different inversion steps (Hayley et al., 2011). The damping factor α controls the regularization in time domain. Or in other words it controls how big the differences between the models are at different times. A value of zero indicates no time regularization and higher values will result in models that are more similar compared to others (Rucker et al., 2011). This value can be modified by the user manually. Also, the program RES2DINVx64 allows the user to choose the type of the time-lapse constraint. This can be set to blocky changes (L1 norm), smooth changes (L2 norm) or to no constraints where the inversions are carried out independently (Loke, 2017).

The DC2DInvRes software package was used for pre-processing of the measured data, thus it is possible to choose value ranges and eliminate selected data points. For further inversion steps, the program RES2DINVx64 was used.

3.2 Test site Gams

To identify the best array configuration for the landfill monitoring, several ERT measurements under known subsurface conditions were carried out. Therefore, the paleomagnetic laboratory of the “Montanuniversität Leoben” in Gams is ideal. The water level is in a depth of approximately 4 m to 5 m and the lithology is mainly composed of gravels. Three profiles (Fig. 11), each with 29.70 m lengths, 0.30 m electrode spacing and 2 m spacing from each other, were measured in four different array configurations (dipole-dipole (DPDP), pole-dipole (PDP), Wenner (WE) and Schlumberger (SCHL)).

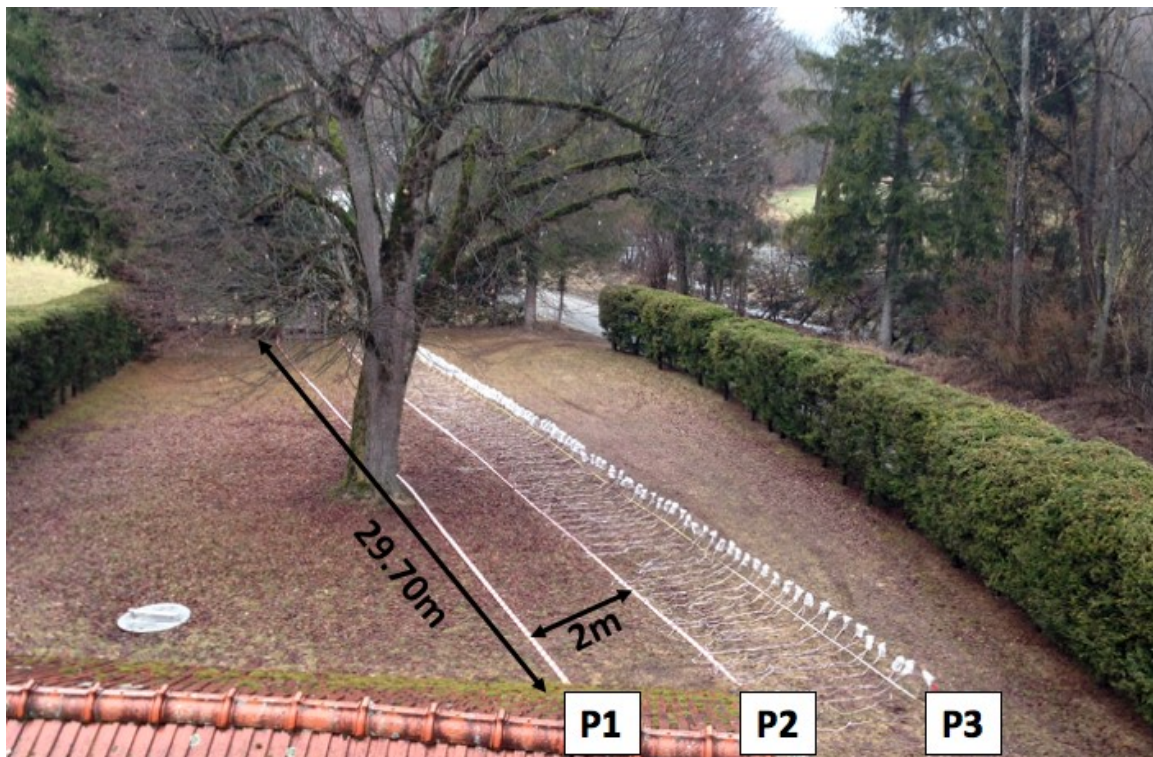


Fig. 11: Location of the profiles in Gams. (Abbreviations: P1 = profile 1 – P3 = profile 3).

The comparison measurements of the different arrays were carried out from 15/03/2018 until the 18/03/2018. During this time, there were different weather conditions, ranging from sunny over partly cloudy to rainfall. Rainfall might be a problem during interpretation and comparison, because of additional water in the subsurface. Therefore, the rainfall statistics is shown in Fig. 12. On the first day and the days before the measurements, there was no rainfall at all. In the night from 15/03/2018 to 16/03/2018 and during the 17/03/2018 at noon until the 18/03/2018 in the morning there was light to normal rainfall.

To minimize the effect of the rain, the comparison measurements were carried out shortly after each other, leading to no significant rainfall effects. For this reason, the different measurements can be easily compared with each other.

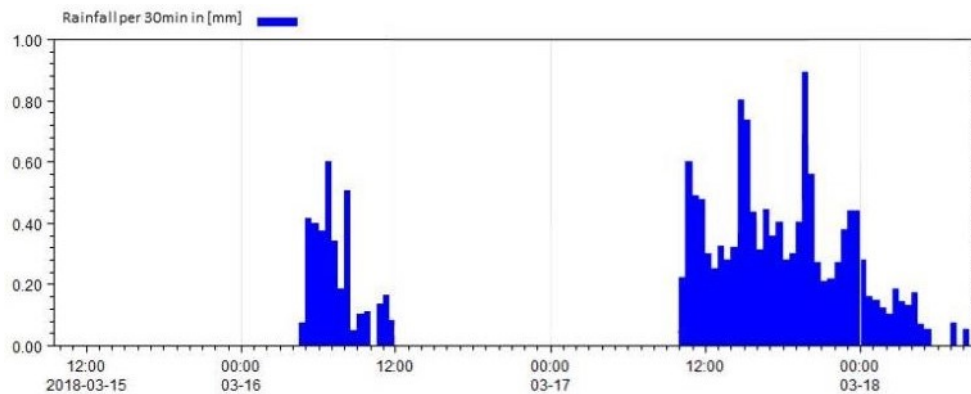


Fig. 12: Rainfall statistics from 15/03/2018 12:00 o'clock until the 18/03/2018 08:00 o'clock. Before and after this period of time there was no rainfall (Modified after: Hydrographie Steiermark (18/03/2018)).

3.2.1 Quality check of the 4point light 10W device

Before all measurements were performed, a calibration of the 4point light 10W device was done. The calibration of the instrument is an important step to guarantee the accuracy during all measurements. Two important factors control the accuracy of the instrument (Lippmann, 2014): the internal phase shift between current and voltage and the offset voltage, which is the voltage measured by the instrument if M and N are shorted. To obtain these factors a full calibration after the operating instructions from Lippmann (2014) was conducted. To control the calibration, two ERT measurements with a Wenner array configuration were executed at profile 1 in Gams (Fig. 11), one before and one after. The results of the ERT inversion are shown in Fig. 13 where Fig. 13a and b display the modelled resistivity section before and after the calibration and Fig. 13c represents the resistivity change in percent between the two modelled sections. The modelled sections indicate a horizontally aligned low resistivity zone at around 4.5 m depth which coincides with the prevailing groundwater level. In the first upper half meter, also a low resistivity zone occurs. That can be linked with the uppermost soil layer. Between these two zones a medium resistivity zone exists (gravels) with a very high resistivity lens in the left part. Interestingly this high resistivity zone is at the exact same position as the location of the tree (Fig. 11).

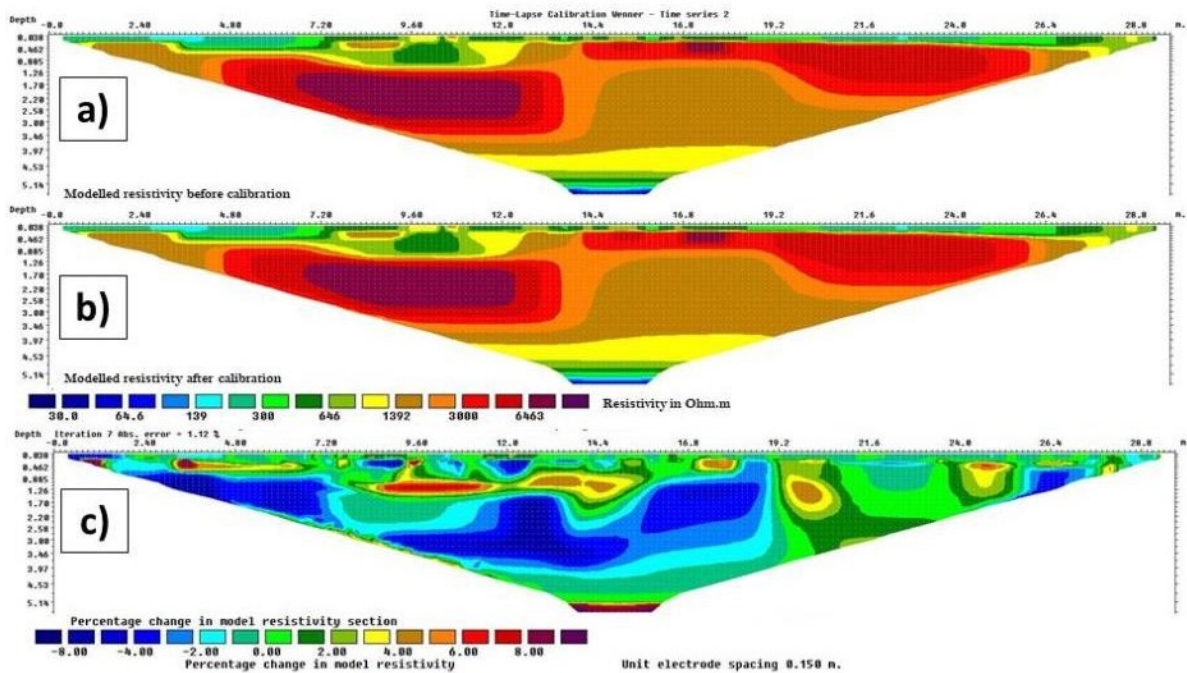


Fig. 13: Quality check of the calibration procedure at profile 1. (a) Modelled resistivity section before the calibration. (b) Modelled resistivity section after the calibration. (c) Resistivity change in percent obtained through the calibration procedure in the modelled sections.

Additionally, the measured apparent resistivities before and after the calibration are represented in Fig. 14. Since the percent change in the resistivity is small and randomly distributed over the whole section (Fig. 13c) and the plotted line in Fig. 14 is nearly 45° with no outliers, indicates that the instrument was well calibrated even before the calibration procedure. Generally, this experiment shows that a calibration of the instrument does not need to be carried out before each survey. It is sufficient to calibrate the measurement device once a year.

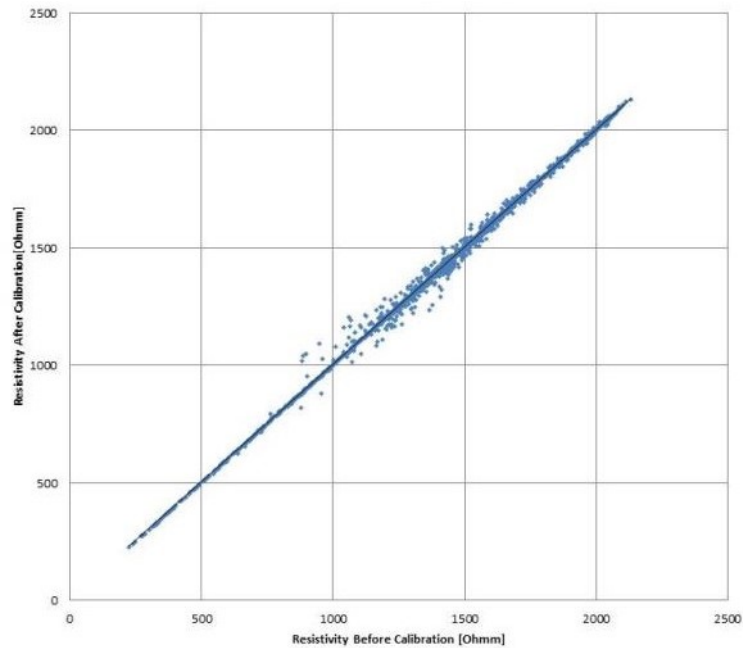


Fig. 14: Comparison of measured resistivity values before (horizontal axis) and after (vertical axis) calibration. The nearly 45° line indicates no significant changes during calibration.

3.2.2 Statistical evaluation

A statistical evaluation is an important tool for the comparison of different array types, since this is done before the inversion and thus with raw data. All measurements were executed with 100 electrodes with a separation of 0.30 m leading to a profile length of 29.70 m. The values of the resistivities (in Ohmm) and measurement errors (dU in %) are similar for each array type and profile. In Tab. 2, a detailed statistical analysis of the resistivities is given. There the different array types are abbreviated: Wenner (WE), Schlumberger (SCHL), dipole-dipole (DPDP) and pole-dipole (PDP_In = remote electrode in-line direction; PDP_P = remote electrode perpendicular to the profile direction). Additionally, the abbreviations PDP_PHQ stand for pole-dipole measurements with the remote electrode perpendicular to the profile direction and modified settings (HQ = high quality) of the measurement device and PDP_PL for the equal direction of the remote electrode but again with modified settings of the measurement device (L = long). These settings and measurements are explained in detail in chapter 3.2.3. The first column indicates the amount of measured data which is defined by the distribution of data points for the different array types. All four array types are self-contained (WE 1617 data points, SCHL 1763 data points, DPDP 1695 data points and PDP

1593 data points) except the PDP measurements at profile 1. Here two (PDP_P) or rather three (PDP_In) measurements were not stored. The next following two columns indicate the measured minimum and maximum values. Negative resistivity values cannot occur and are therefore measurement errors. These values are rare and only occur in the PDP measurements. However, the amount of negative values is small (8 to 12) except for the PDP_PHQ measurement. The resistivity yield in mean values in the range of 1305 Ohmm up to 1405 Ohmm for profile 1, 1008 Ohmm up to 1230 Ohmm for profile 2 and 842 Ohmm up to 1081 Ohmm for profile 3. A similar trend can be seen for the standard deviation and median identifiable. Any statistical parameter (mean, standard deviation and median) displays the same range (around 200-250 Ohmm) from the lowest to the highest value for each array type and profile.

Name	Amount of values	min. value [Ohmm]	max. value [Ohmm]	mean [Ohmm]	standard deviation [Ohmm]	median [Ohmm]	amount of neg. values
P1_WE	1617	225,22	2130,71	1404,54	416,76	1460,19	0
P1_PDP_In	1590	-5722,07	8818,62	1221,52	684,67	1197,39	8
P1_PDP_P	1591	-210,38	6568,83	1215,89	620,88	1192,20	1
P1_SCHL	1763	218,74	2450,68	1376,37	474,08	1406,05	0
P1_DPDP	1695	162,44	3017,31	1305,44	669,76	1244,83	0
P2_WE	1617	223,77	1799,04	1230,30	397,71	1328,00	0
P2_PDP_In	1593	-3358,09	5442,31	1009,53	565,05	982,00	12
P2_PDP_P	1593	-6260,14	8019,30	1008,17	614,23	978,93	13
P2_SCHL	1763	231,37	2018,44	1230,17	438,46	1306,99	0
P2_DPDP	1695	141,55	3001,53	1166,72	631,90	1112,61	0
P3_WE	1617	193,01	1653,18	1072,53	349,33	1116,55	0
P3_PDP_In	1593	-2044,07	2105,14	894,36	484,67	846,96	4
P3_PDP_P	1593	-1978,40	4614,44	889,42	496,53	840,51	5
P3_PDP_PHQ	1593	-35,77	2045,43	841,63	502,95	818,96	43
P3_PDP_PL	1593	-970,99	2024,72	867,77	458,50	826,57	2
P3_SCHL	1763	192,95	1965,14	1081,46	392,49	1118,50	0
P3_DPDP	1695	150,44	2329,51	1027,89	546,65	977,46	0

Tab. 2: Statistical evaluation for the resistivity values of profile 1 to 3. (Abbreviations: P1 = profile 1 to P3 = profile 3; WE = Wenner array; PDP = Pole-dipole array; PDP_In = pole-dipole array with remote electrode in-line direction; PDP_P = pole-dipole array with remote electrode perpendicular to the profile direction; _PL and _PHQ = see text above; SCHL = Schlumberger array and DPDP = dipole-dipole array).

Tab. 3 indicates a detailed analysis of the measurements errors. All maximum values are in a good range (up to 5.66 %) except for the PDP measurements. There, the highest values are up to 2490 %. Furthermore, the data quality is high, displaying a mean error value between

0.04 % and 3.08 %. Interestingly, the lowest mean values were obtained with the SCHL and DPDP array. Values of the standard deviation are in the range of 0.07 % up to 64.06 %. High values only occur for the PDP measurements. Also, the median displays very low values (0.02 % to 0.06 %). Another quality criterion is the amount of values below 2 % measurement error. This is very good for the WE, SCHL and DPDP array and sufficient for the PDP array. Since the PDP array configuration produces many errors, a detailed statistical evaluation of the raw data is described in section 3.2.3 to determine the causes. For a vivid presentation of Tab. 3, Fig. 15 displays a Box-Whisker plot. Here, values of 0.00 % had to be converted into 0.01% to set a logarithmic vertical axis of the Box-Whisker plot. This is permissible because the difference is in the range of 10^{-4} % for median and mean.

	dU min. value [%]	dU max. value [%]	dU mean [%]	dU standard deviation [%]	dU median [%]	values above 2% dU	values equal 0% dU
P1_WE	0	3,18	0,14	0,25	0,05	2	96
P1_PDP_In	0	602,76	2,46	25,87	0,03	73	107
P1_PDP_P	0	2489,37	3,08	64,06	0,03	70	89
P1_SCHL	0	5,66	0,03	0,14	0,02	1	181
P1_DPDP	0	1,26	0,05	0,08	0,02	0	178
P2_WE	0	5,23	0,23	0,44	0,06	14	73
P2_PDP_In	0	681,32	1,44	19,50	0,03	68	88
P2_PDP_P	0	134,80	0,63	4,81	0,03	64	112
P2_SCHL	0	1,22	0,05	0,09	0,02	0	176
P2_DPDP	0	0,55	0,04	0,06	0,02	0	168
P3_WE	0	4,29	0,23	0,41	0,05	12	67
P3_PDP_In	0	286,91	0,47	7,45	0,03	38	117
P3_PDP_P	0	109,15	0,38	3,73	0,02	33	129
P3_PDP_PHQ	0	54,69	0,28	1,86	0,04	29	58
P3_PDP_PL	0	82,13	0,23	2,24	0,02	17	117
P3_SCHL	0	1,78	0,05	0,10	0,02	0	196
P3_DPDP	0	0,89	0,04	0,07	0,02	0	157

Tab. 3: Statistical evaluation for the measurements errors dU (in %) values of profile 1 to 3. (Abbreviations: P1 = profile 1 to P3 = profile 3; WE = Wenner array; PDP = Pole-dipole array; PDP_In = pole-dipole array with remote electrode in-line direction; PDP_P = pole-dipole array with remote electrode perpendicular to the profile direction; _PL and _PHQ = see text above; SCHL = Schlumberger array and DPDP = dipole-dipole array).

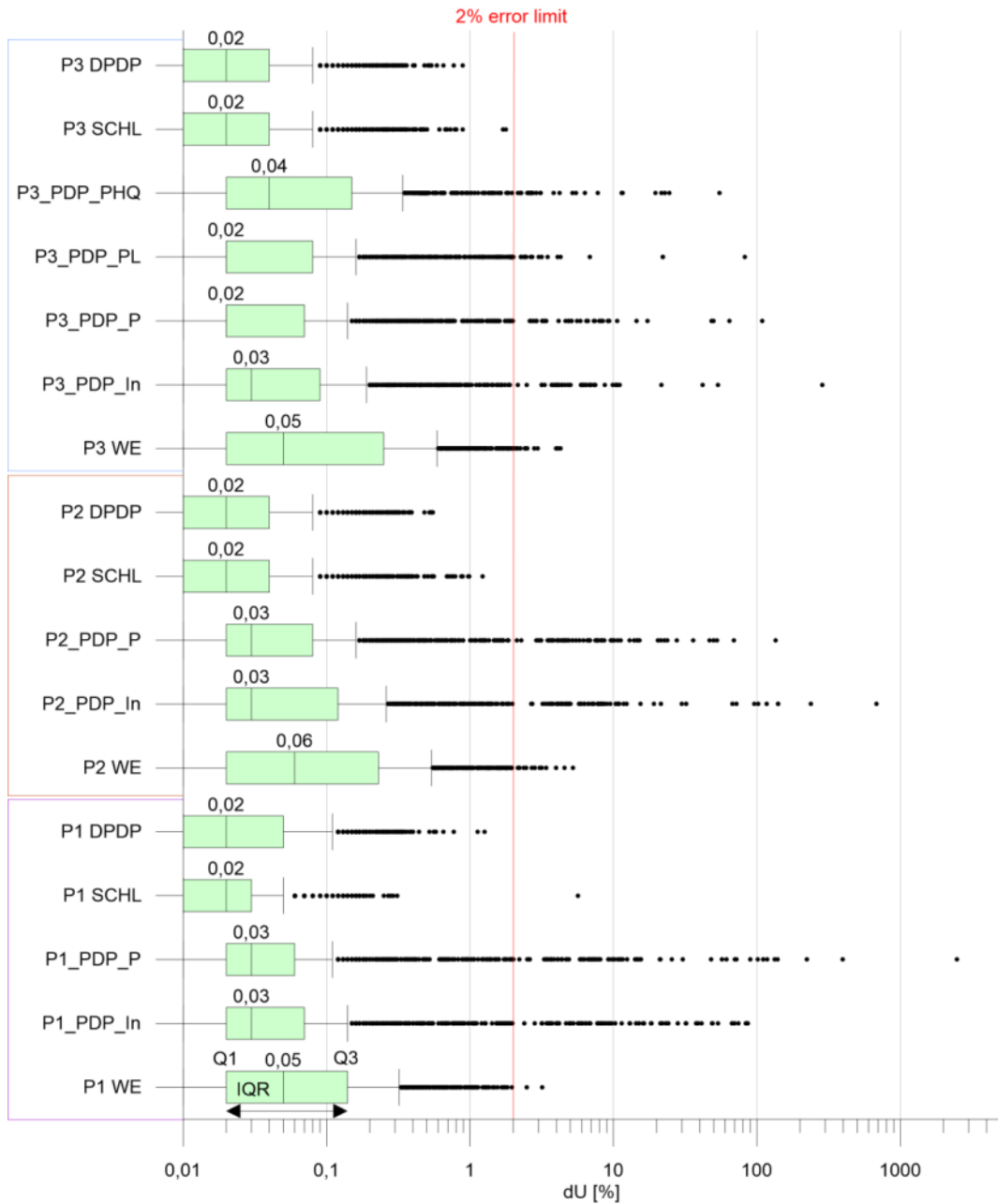


Fig. 15: Box-Whisker plot of the measurement error dU (in %) for profiles 1 to 3. The median is displayed for all measurements. The upper Whisker is located at $IQR \times 1.5$. (Abbreviations: IQR = interquartile range; Q1 = lower quartile; Q3 = upper quartile; P1 = profile 1 to P3 = profile 3; WE = Wenner array; PDP = Pole-dipole array; PDP_In = pole-dipole array with remote electrode in-line direction; PDP_P = pole-dipole array with remote electrode perpendicular to the profile direction; _PL and _PHQ = see text above; SCHL = Schlumberger array and DPDP = dipole-dipole array).

3.2.3 Pole-Dipole array comparison

At the three profiles in Gams (Fig. 11) pole-dipole measurements were carried out, which show many errors in comparison to the other array types. To identify from where these errors occur, this section deals with statistical evaluations of the measured raw data. In Tab. 4 the values of the measurement errors (dU in %) are seen. P1 to P3 stands for profile 1 to profile 3.

Name	Amount of values	dU [%]					
		min. value	max. value	mean	standard deviation	median	Amount of values over 2% error
P1_PDP_In	1585	0,00	86,69	0,89	5,96	0,03	65,00
P1_PDP_P	1592	0,00	2489,37	2,97	63,93	0,03	69,00
P2_PDP_In	1593	0,00	681,32	1,44	19,50	0,03	68,00
P2_PDP_P	1593	0,00	134,80	0,63	4,81	0,03	64,00
P3_PDP_In	1593	0,00	286,91	0,47	7,45	0,03	38,00
P3_PDP_P	1593	0,00	109,15	0,38	3,73	0,02	33,00
P3_PDP_PL	1593	0,00	82,13	0,23	2,24	0,02	17,00
P3_PDP_PHQ	1593	0,00	54,69	0,28	1,86	0,04	29,00

Tab. 4: dU values of profile 1-3 for the pole-dipole array. Minimum and maximum values, mean, standard deviation and median are calculated. (Abbreviations: P1 to P3 = profile 1 to profile 3; PDP = pole-dipole array; _In = remote electrode in-line direction; _P = remote electrode perpendicular to profile direction; _PL and _PHQ = different settings which are explained in the following text).

Generally, the pole-dipole measurements were performed with 100 electrodes and 0.30 m electrode spacing. The remote electrode B was located 100 m away in line direction or 100 m perpendicular away from the profile. The frequency was set to 4.16Hz (European standard) to avoid the frequency effect (Lippmann, 2014). Also, the measurements were carried out with default settings of the GeoTest software, except for profile 3. There, additionally two measurements with alternative settings were conducted. The default settings assume that the resulting voltage is between a defined interval and the measurements are repeated until the deviations of the readings reaches a defined limit. For the default settings, the limit is 2 % and the number of readings is between 2 and 5. Measurement P3_PDP_PL was carried out with default settings, but with a maximum number of readings of 20. This allows the software to be more precisely, because extra time

is available for each measurement. P3_PDP_PHQ was measured with the pre-defined high quality settings. With this setup, the maximum possible current is used and the number of readings is between 2 and 20 with a limit of 0.5 %.

A graphical statistical evaluation of the Tab. 4 is displayed in the Box-Whisker plot (Fig. 16). Values over 2 % are no longer representative for the dataset and will be neglected in further processing steps. In the Box-Whisker plot it is visible that the amount of values over 2% is commonly less by measurements perpendicular to the profile except for profile 1. P3_PDP_PL has the fewest errors over 2% and only 3 outliers over 5%. Overall the data quality for profile 3 is good, displaying a mean of the error between 0.23 and 0.47% and fine for profile 1 and 2.

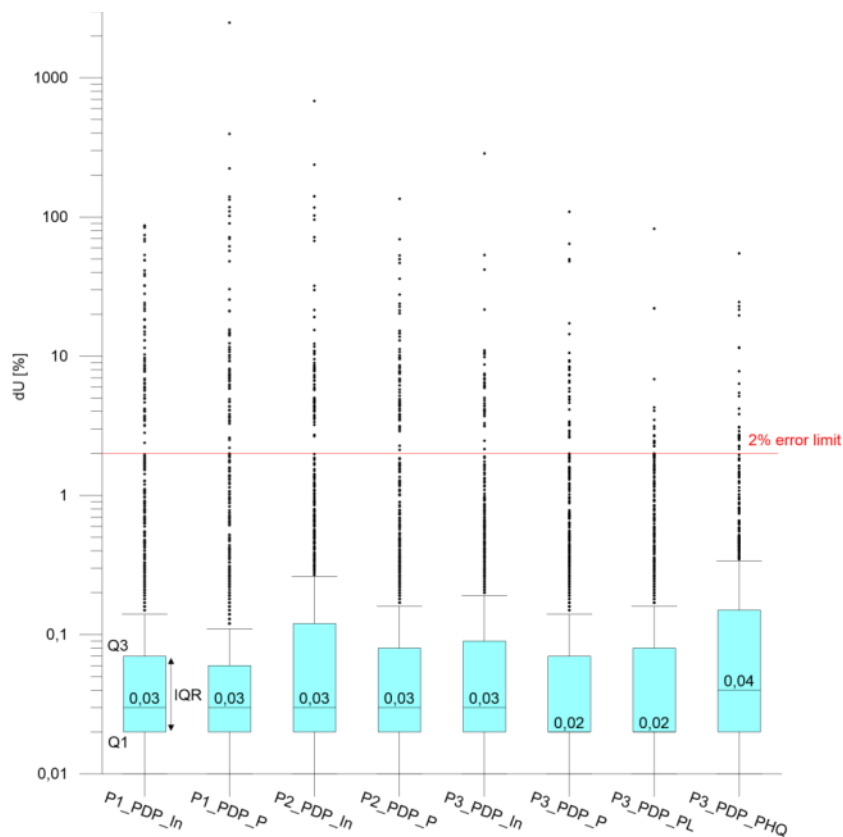


Fig. 16: Box-Whisker plot of the measurement error dU [%] for profiles 1 to 3 for the pole-dipole array. The median is displayed for all 8 measurements. The upper Whisker is located at $IQR \cdot 1.5$. Perpendicular direction of the remote electrode show generally less errors compared to the in-line direction. (Abbreviations: IQR = interquartile range; Q1 = lower quartile; Q3 = upper quartile; HQ = high quality; PDP = pole-dipole array; _In = remote electrode in-line direction; _P = remote electrode perpendicular to profile direction; _PL and _PHQ = different settings which are explained in the previous text).

To identify the proper settings and from where errors occur, dU in % is plotted against the measurement number, electrode number and electric current I in mA for profile 3. The other

two profiles (1 and 2) show the same trends as demonstrated in the following figures and thus they are not described. In Fig. 17 to Fig. 19 dU versus the measurement number is displayed. With increasing measurement number, the depth of the measurements increases gradually, considering the software measures first the first depth layer (measurement number 1 to 98), then the second (measurement number 99 to 195) and so on. Thus, it is possible to make statements about the error distribution according to depths. Fig. 17 plots dU versus the measurement number for P3_PDP_P, Fig. 18 for P3_PDP_PL and Fig. 19 for P3_PDP_PHQ. In all three plots the errors are randomly distributed over the whole interval and most of them are around 0.01 % to 0.03 %. However, P3_PDP_PHQ (Fig. 19) displays errors of about 0.5 % for the first 180 measurements and P3_PDP_PL shows least errors over 2 % in comparison with P3_PDP_P and P3_PDP_PHQ.

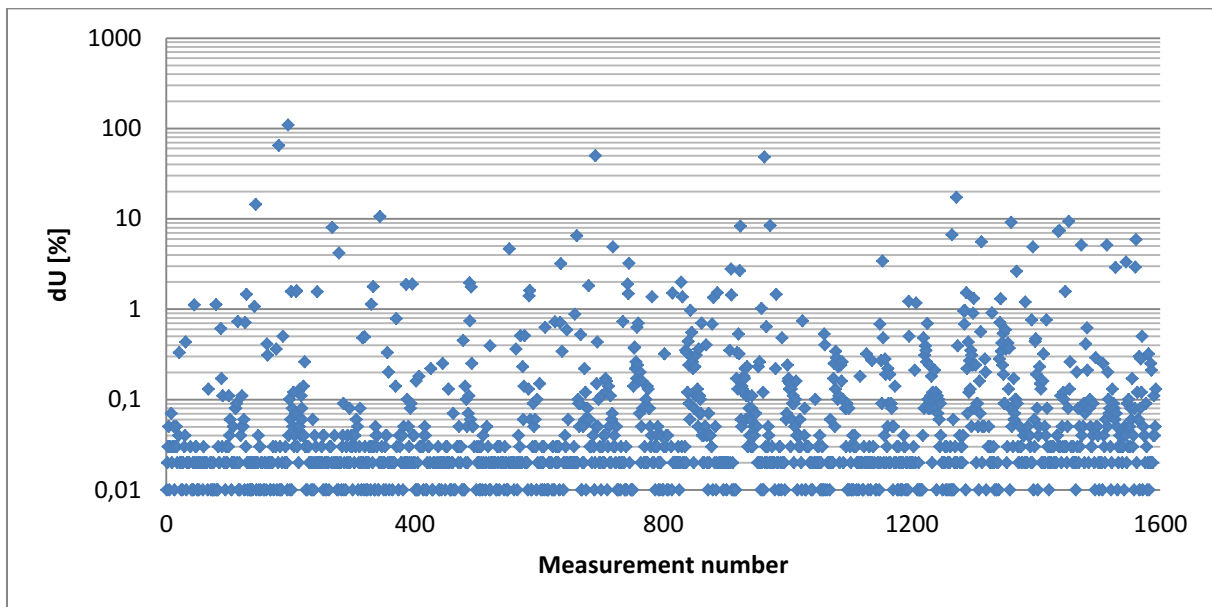


Fig. 17: The horizontal axis shows the measurement number and the vertical axis dU in % for profile 3 - P3_PDP_P. With increasing number of the measurements also the depth of the measurements increases.

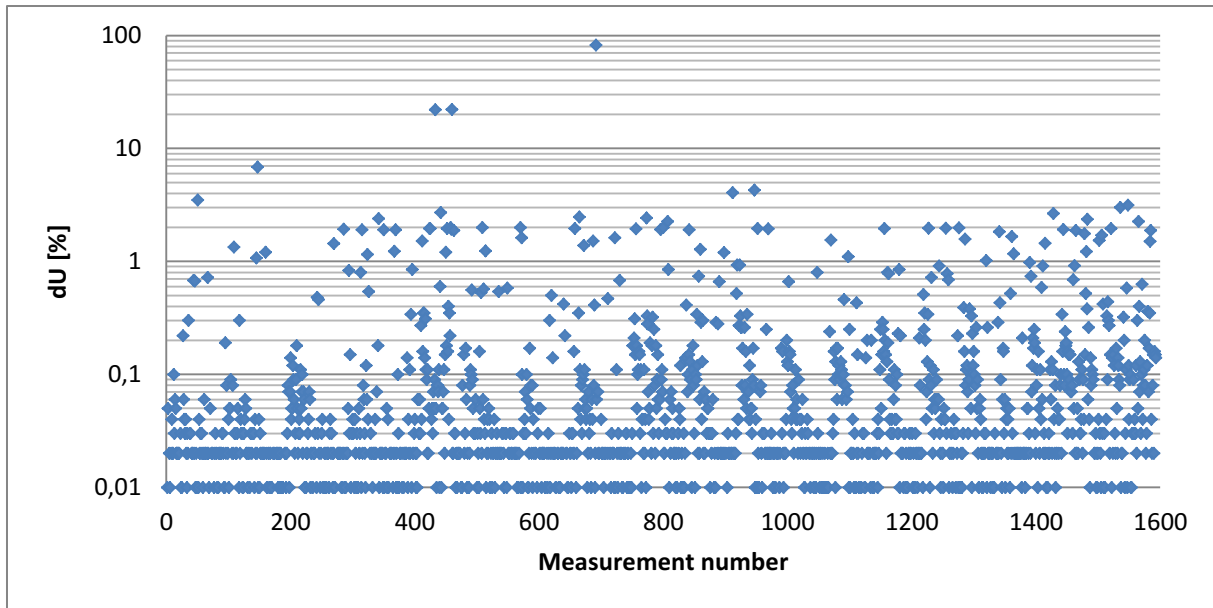


Fig. 18: The horizontal axis shows the measurement number and the vertical axis dU in % for profile 3 - P3_PDP_PL. With increasing number of the measurements also the depth of the measurements increases.

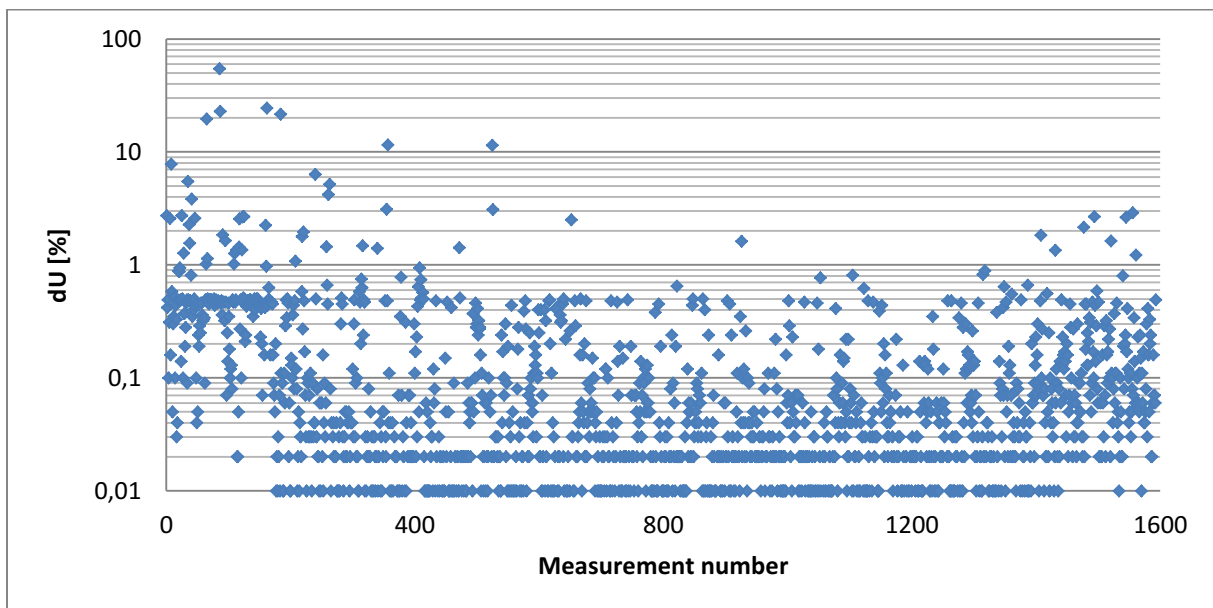


Fig. 19: The horizontal axis shows the measurement number and the vertical axis dU in % for profile 3 - P3_PDP_PHQ. With increasing number of the measurements also the depth of the measurements increases.

During multi electrode surveys the positions of the electrodes A, M and N change along the profile according to the wanted subsurface position of the measurement. Since this is the case, statements can be made whether one or more electrodes have a malfunction. In Fig. 20, dU versus the electrode number of P3_PDP_P is displayed. Additional one measurement with an error of around 100 % is marked with a red circle. If now an electrode has a

malfunction, then several readings must be placed on a vertical line at the electrode number position of the damaged electrode. This is not the issue and therefore no involved electrode has a malfunction. General in the whole plot there are no defect electrodes identifiable. The same trend is visible in Fig. 21 and Fig. 22, which show the plots for P3_PDP_PL and P3_PDP_PHQ.

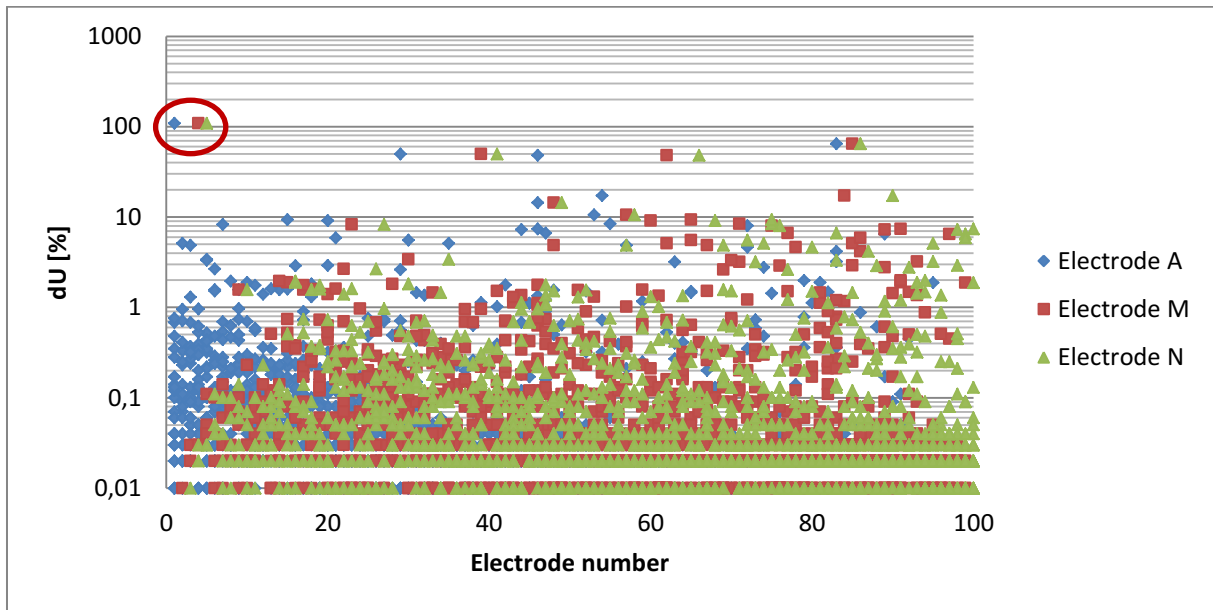


Fig. 20: The horizontal axis shows the electrode number and the vertical axis dU in % for profile 3 - P3_PDP_P. The red circle marks one measurement with an error around 100 %.

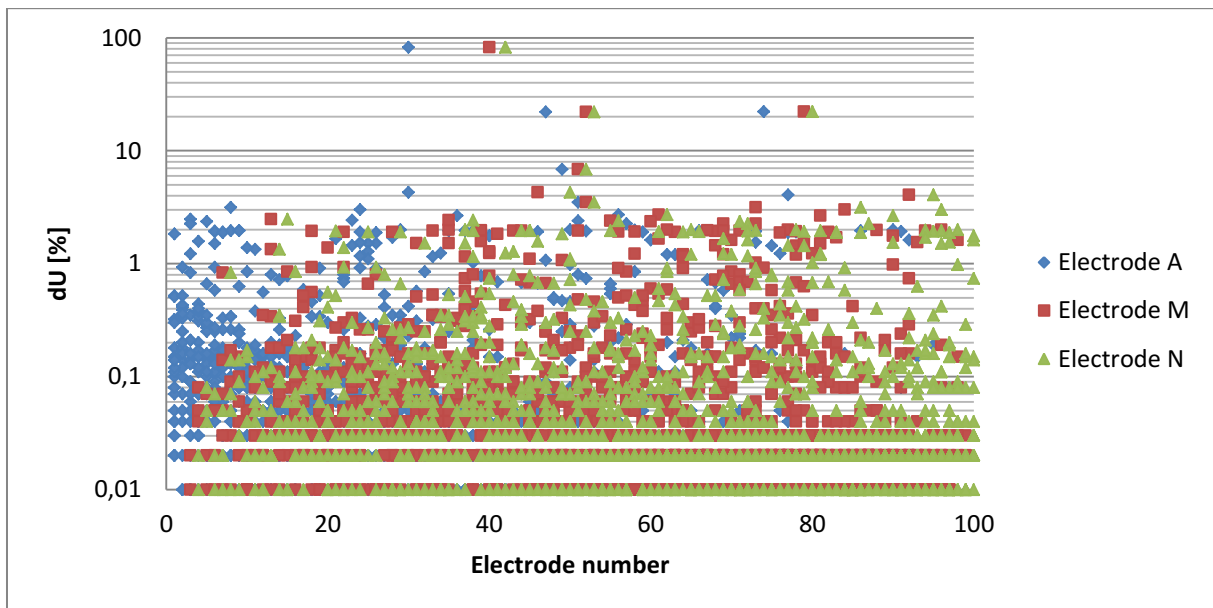


Fig. 21: The horizontal axis shows the electrode number and the vertical axis dU in % for profile 3 - P3_PDP_PL.

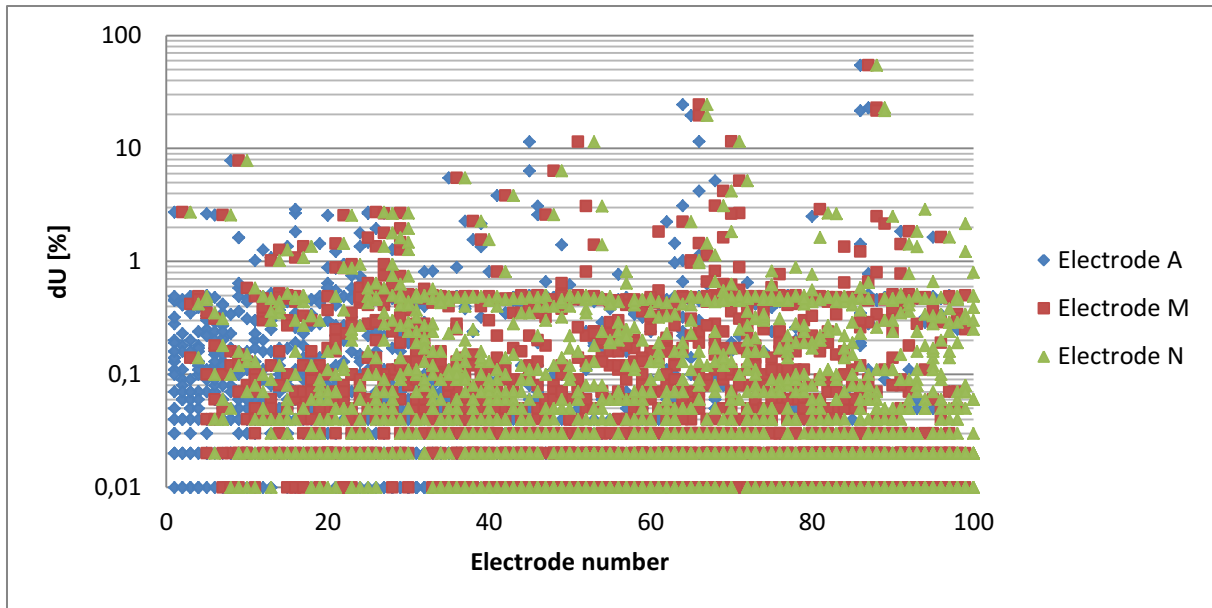


Fig. 22: The horizontal axis shows the electrode number and the vertical axis dU in % for profile 3 – P3_PDP_PHQ.

The following figures (Fig. 23 to Fig. 25) represent dU versus the electric current in mA. In Fig. 23 this is visible for the P3_PDP_P measurement. There the highest errors (over 10 %) occur at an electric current of 0.1 mA. The other currents (1; 5; 15 and 50 mA) also exhibit errors, but in a smaller range from 2 % up to 10 %. For the P3_PDP_PL survey (Fig. 24) the highest errors also occur at an electric current of 0.1 mA, but for the other ones the error values are smaller compared with the P3_PDP_P measurement. They are ranging up to a maximum of 4 % for 1 mA and 50 mA and 2.5 % for 5 mA and 15 mA. The previously described trend is not visible for the P3_PDP_PHQ measurement (Fig. 25). Here the highest errors occur at 15 mA and 50 mA and the lowest at 0.1 mA, 1 mA and 5 mA.

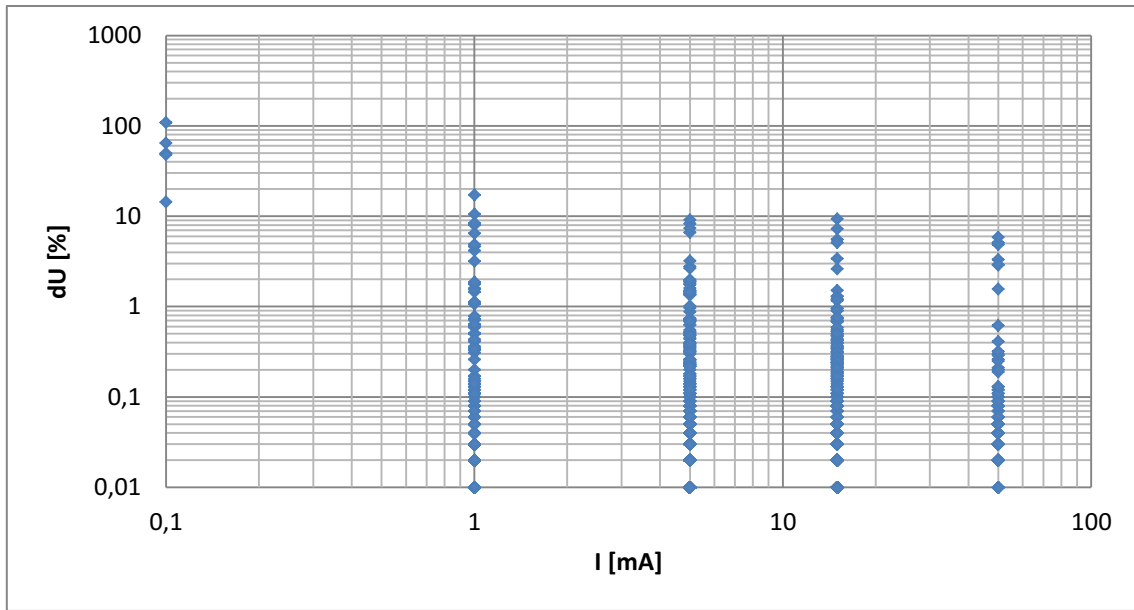


Fig. 23: The horizontal axis shows the electric current in mA and the vertical axis dU in % for profile 3 - P3_PDP_P.

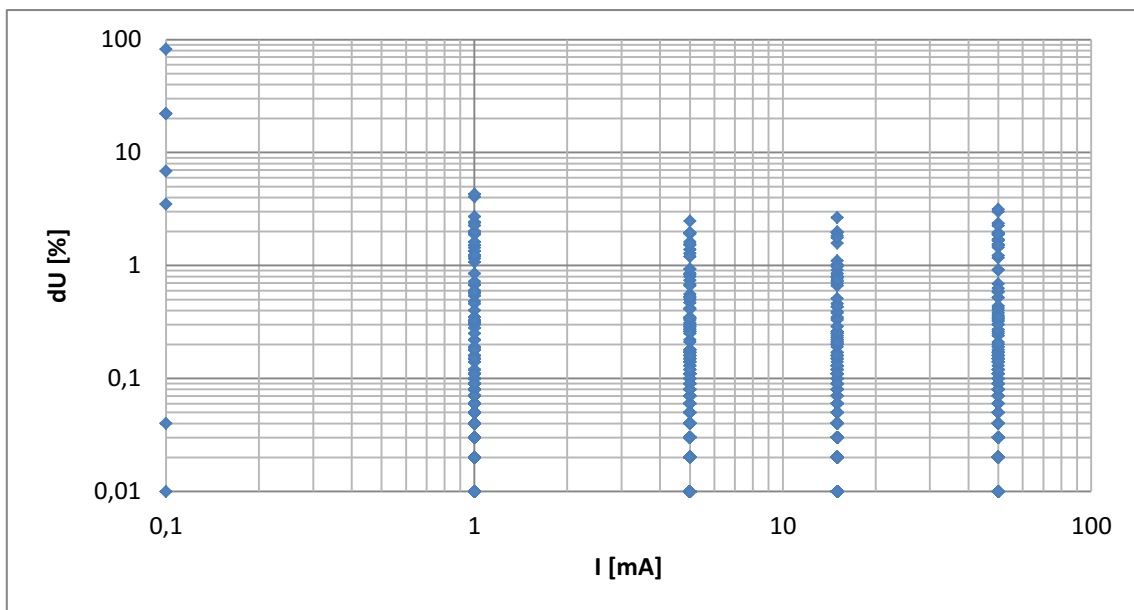


Fig. 24: The horizontal axis shows the electric current in mA and the vertical axis dU in % for profile 3 - P3_PDP_PL.

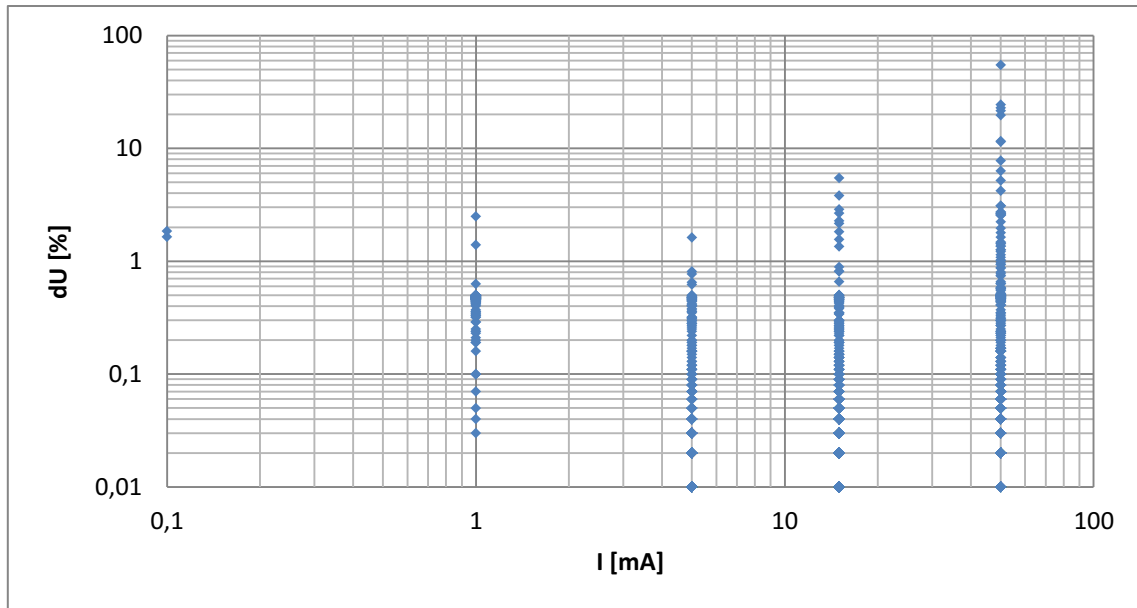


Fig. 25: The horizontal axis shows the electric current in mA and the vertical axis dU in % for profile 3 - P3_PDP_PHQ.

Based on the previous 9 plots the errors occur randomly and are not connected to the measurement depth, electrode number or strength of the electric current. Fig. 17 to Fig. 19 displays no concentration of errors at a certain number of depths and therefore they are incidentally distributed. In Fig. 20 to Fig. 22 there was no vertical line identifiable, which leads to the assumption that all electrodes worked well. And in Fig. 23 to Fig. 25 the errors according to the electric current are randomly distributed, since no current value indicates a particularly high number of errors. However, the highest error values occur at low currents (0.1 mA) for P3_PDP_P and P3_PDP_PL and high currents (50 mA) for P3_PDP_PHQ. Therefore, it is only possible to modify the settings and choose the direction of the remote electrode B to obtain fewer errors. Perpendicular directions are preferred which is visible in Fig. 16. There, fewer errors occur over 2% generally in perpendicular directions compared to in line directions. By comparing P3_PDP_P, P3_PDP_PL and P3_PDP_PHQ it can be demonstrated that the P3_PDP_PL settings provide the best results. The reason for this is that most of the errors are below 2% (Fig. 16, Fig. 18, Fig. 21 and Fig. 24) in comparison to P3_PDP_P and P3_PDP_PHQ. With P3_PDP_PHQ the worst results are obtained. This can be exemplarily seen in Fig. 19 where the first 180 measurements show error values around 0.5%. As a conclusion, when using a pole-dipole array, the remote electrode B is supposed to be perpendicular to the profile and the GeoTest software settings should be default, except the maximum number of readings. These are recommended to be set to 20 times. However, the errors over 2% are high for a homogenous subsurface. That's why the pole-dipole array

configuration will not be further investigated, since the subsurface of the landfill is expected to be very heterogeneous.

3.2.4 Comparison of the Wenner-, Schlumberger- and Dipole-Dipole array

Since the pole-dipole array configuration produces too many measurement errors (see section 3.2.3), the following section deals with the comparison of the Wenner-, Schlumberger- and Dipole-Dipole array configuration. All three array types have good statistical values and therefore the focus is now on the comparison of the inversion results. The inversion was carried out with the DC2DInvRes software, because there it is possible to exactly define model cells.

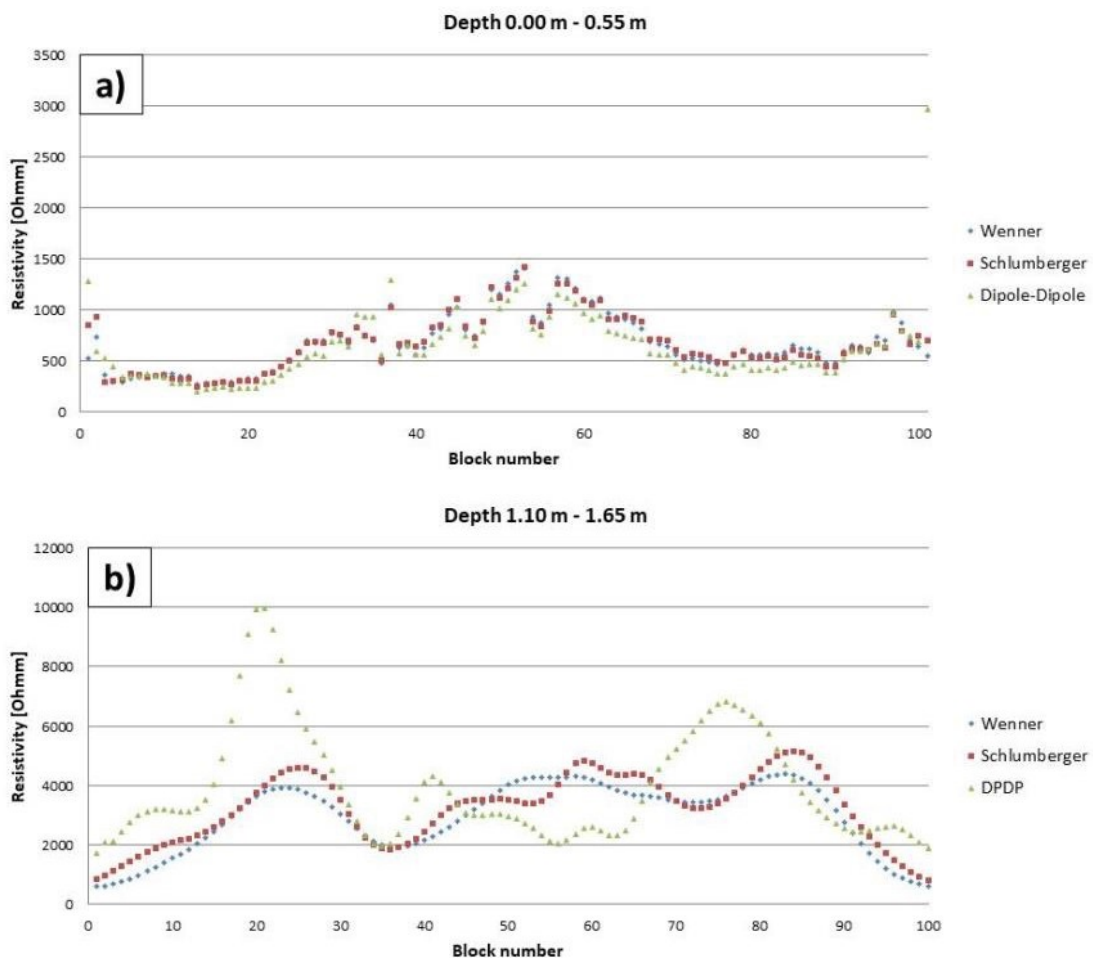
In Tab. 5 the used inversion parameters are listed. The starting model was divided into 10 layers in z-direction and 100 in x-direction leading to a total number of 1000 cells with a background resistivity of 1500 Ohmm. The cell width is 0.55 m in z-direction and 0.3 m in x-direction. The data was inverted with the SIRT (simultaneous iterative reconstruction technique) inversion algorithm.

x-direction layers	z-direction layers	cell width x-direction	cell width z-direction	amount of cells	background resistivity
100	10	0.30m	0.55m	1000	1500 Ohmm

Tab. 5: Inversion parameters for the SIRT (simultaneous iterative reconstruction technique).

In the following figures selected depth slices (layers) of profile 1 are displayed. Each figure represents the resistivity changes along the profile of the WE, SCHL and DPDP array configuration according to one defined depth level. The horizontal axis displays the 100 layers in x-direction and the vertical axis the modelled resistivities in Ohmm. In Fig. 26a the first layer (0 m to 0.55 m) is visible. There the three different array configurations show no major differences. Only the DPDP inversion has two outliers. In comparison Fig. 26b (1.10 m to 1.65 m depth) displays some differences. The main differences are between the DPDP configuration and the Wenner and Schlumberger configuration. WE and SCHL represents the same trend, but the WE configuration seems to smooth vertical resistivity changes more along the profile. DPDP has also a kind of the same trend, but exhibits the largest resistivity

variation. This can be clearly observed at block number 23, between 50 and 65 and at block number 80. For the depth layer 2.20 m to 2.75 m (Fig. 26c) the same general trend as for Fig. 26b is visible, except that the DPDP inversion shows more outliers at the edges of the model. Also, the vertical resistivity variations along the profile appear in all three array types smoother than for depth slice 1.10 m to 1.65 m. Fig. 26d represents a layer depth slice from 3.30 m up to 3.85 m. In comparison with the previous figures the vertical resistivity variation is much smaller. Again, at the edges of the model the DPDP array inversion show some outliers. The Wenner array resistivity inversion is nearly flat and the Schlumberger is like the Wenner. The deepest depth layer (4.95 m to 5.50 m) is represented in Fig. 26e. Here the differences between the arrays are small and the resistivities along the profile stay constant below 1000 Ohmm.



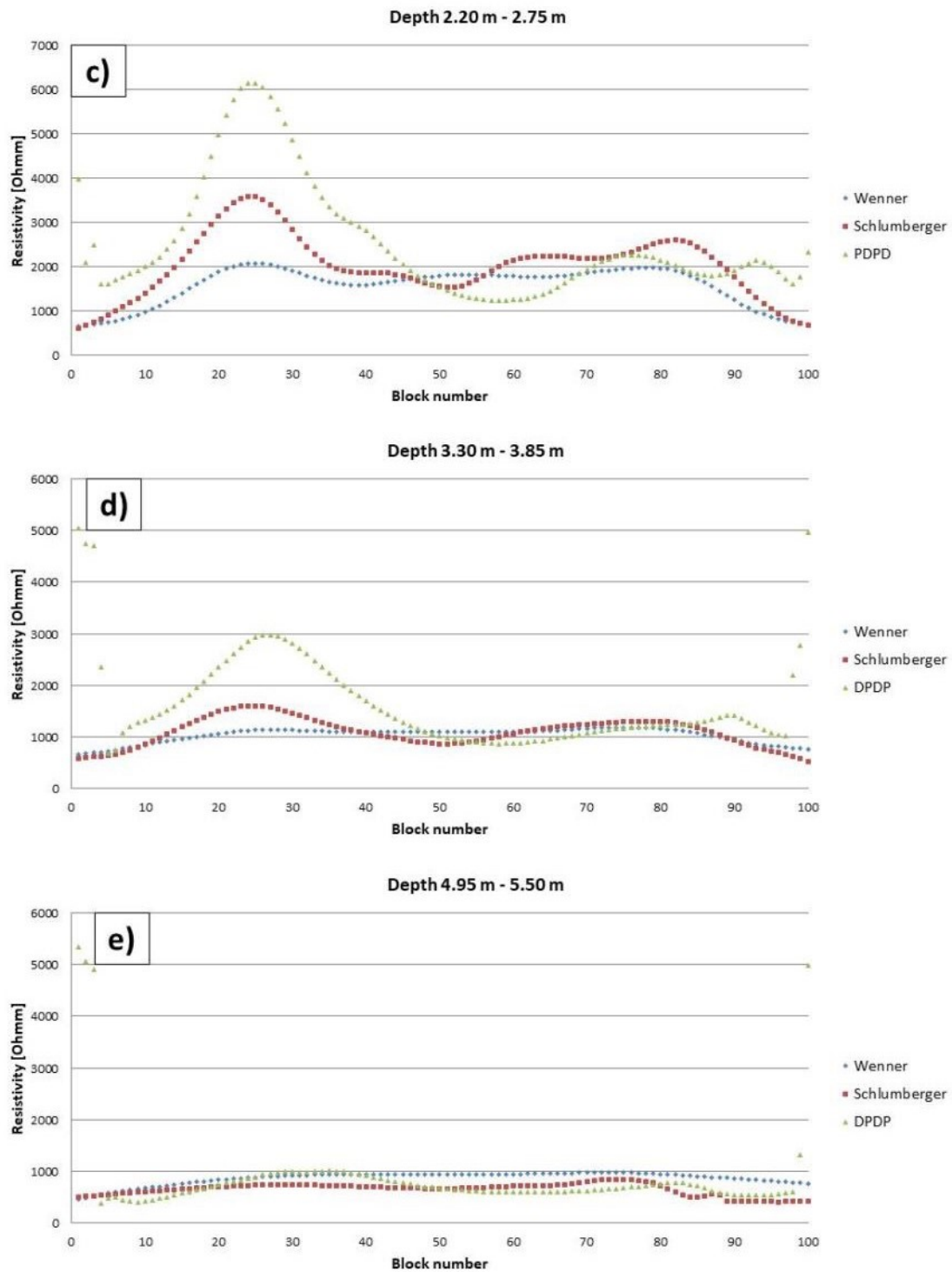


Fig. 26: Resistivity changes along the profile 1 at a depth level between (a) 0.0 m and 0.55 m, (b) 1.10 m and 1.65 m, (c) 2.20 m and 2.75 m, (d) 3.30 m and 3.85 m, (e) 4.95 m and 5.50 m. The horizontal axis indicates the 100 layers in x-direction and the vertical axis the resistivity values obtained with the SIRT inversion.

While comparing the five figures above some general trends are visible. In the first depth slice all array configurations show nearly the same lateral variations in resistivity, because of their similar array geometries. With increasing depth, the array geometry between the three array configurations changes leading to different results in the inversion process. As

described in section 2.2.1 the Wenner array is less sensitive to horizontal resistivity changes in the subsurface, followed by the Schlumberger and dipole-dipole array. This trend is clearly identifiable in Fig. 26c-d. In all three figures the Wenner array is the smoothest with less horizontal resistivity changes along the profile. Since the Schlumberger array is similar to the Wenner array, the same trend is visible, but with more horizontal resistivity changes. In comparison with the previous arrays, the dipole-dipole array indicates the largest changes. These general trends are in good comparison with literature data (Loke, 2015). Another important aspect is that these differences are getting smaller with increasing depth. While in Fig. 26b the differences are still big, in Fig. 26d they are rather small and almost disappeared in Fig. 26e. For the other two profiles (profile 2 and 3) the same similar trends were obtained and therefore they are not displayed here.

3.2.5 Well experiment Gams

To get a better knowledge how the water flow can be monitored in the landfill, a model experiment was carried out at profile 3 (Fig. 11) in Gams. The model scale was approximately 1:7. So the electrode spacing was 0.30 m and the profile length 29.70 m. At profile meter 15.0 a 1.0 m deep well (Fig. 27a) was driven in the ground for the introduction of water into the subsurface. The required water was provided with the aid of a two-stage process. First a container (Fig. 27b) with a volume of approximately 72 l was filled with tap water. Now table salt was added until the conductivity reached a value of 0.3 S/m. For the conductivity control a conductivity meter from Hanna Instruments (HI 8733) was used. In the second stage within 15 minutes the entire water of one container was pumped into the well. Then one geoelectrical measurement with a Wenner array configuration was carried out. The measurement took about 30 minutes so that the overall process of water introduction and geoelectrical measurement lasted about 45 minutes. This process was repeated seven times to obtain the changes due the water introduction. In total 576 l (in the last round two containers of water were used) water was pumped within approximately 5 ½ hours into the subsurface.



Fig. 27: (a) 1.0m deep well with garden hose at profile meter 15 for water introduction. (b) Containers for the provision of conductive (0.3 S/m) water.

For the time-lapse inversion, the software RES2DINVx64 with different parameters for the damping factor α was used. In Fig. 28 the time-lapse inversion for a damping factor $\alpha = 0.25$ is displayed. The resistivity changes between the time series are very small. However, there are slight changes in the upper high resistivity zone marked with a blue circle. At each time step the zone is shifted a little bit more to the left caused by the introduction of water at this location. This introduction is better visible in Fig. 29. The plot displays percentage changes in resistivities between the basic and following measurements due to irrigation. Negative values indicate an increase in water content whereas positive values indicate a decrease in water content.

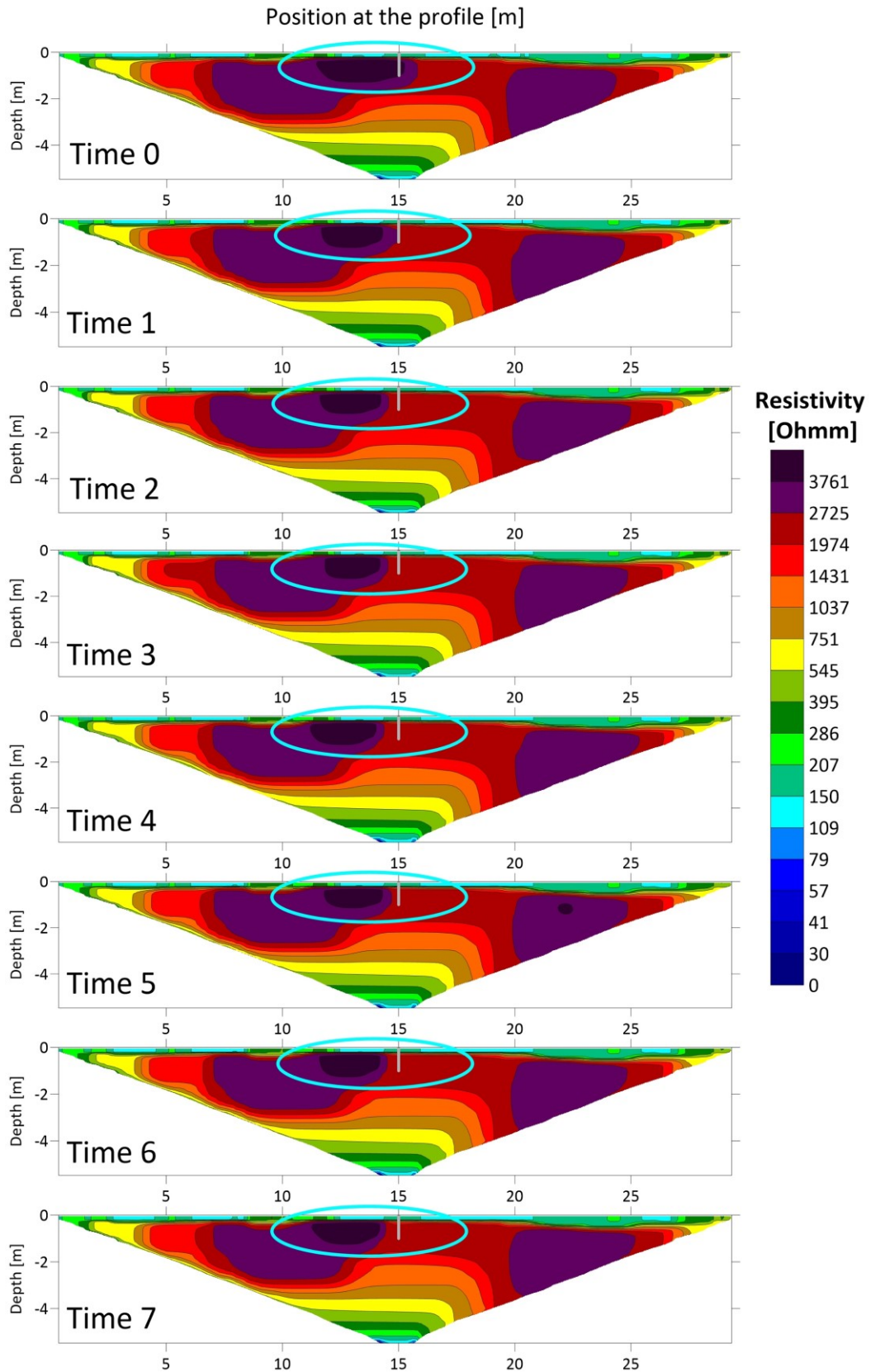


Fig. 28: Results of the time-lapse inversion with a damping factor of 0.25. At time 0 the upper high resistivity zone (marked with a blue circle) lies at profile meter 15. Because of irrigation this becomes smaller and migrates leftwards. The grey line indicates the position and depth of the test well.

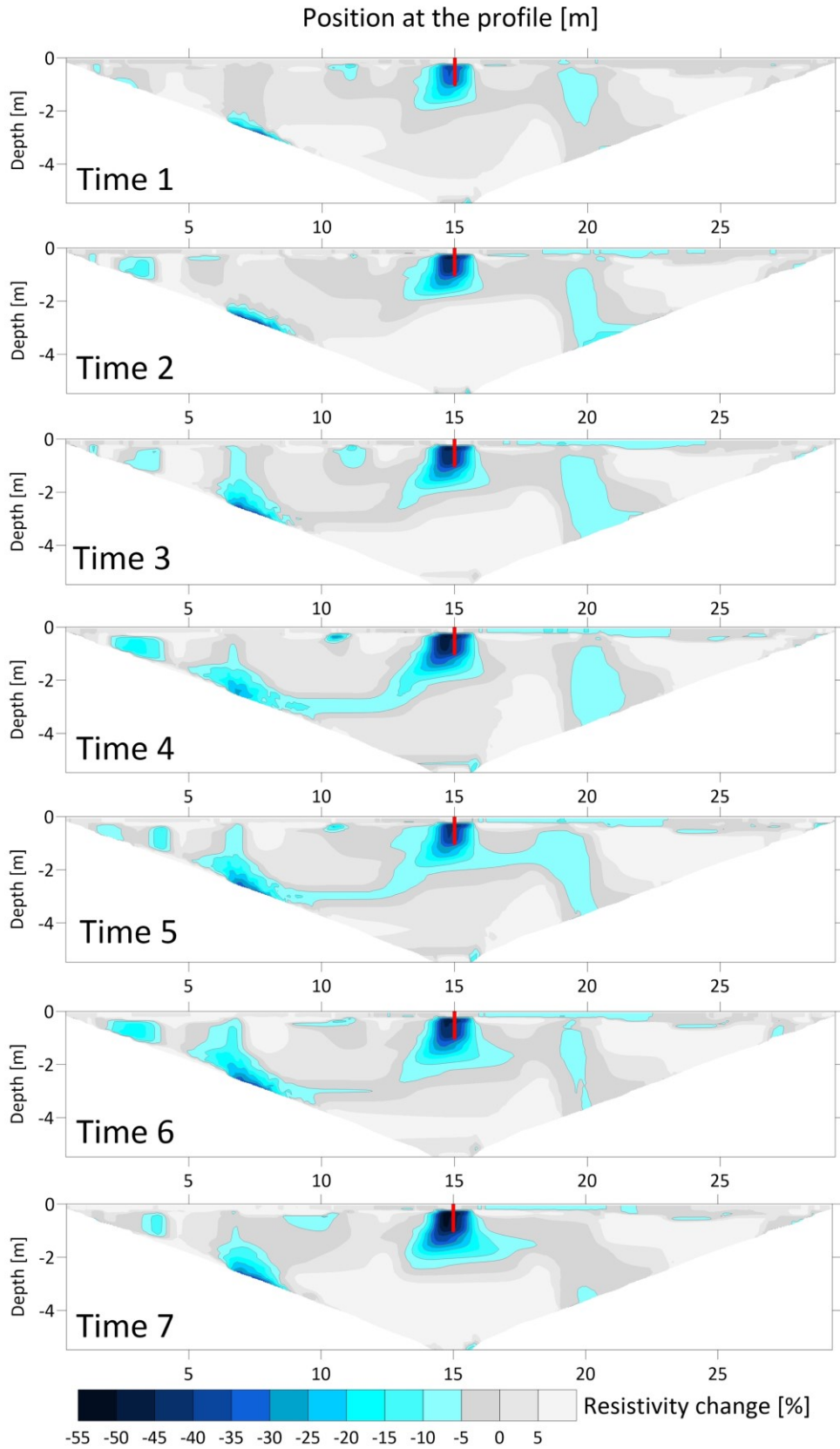


Fig. 29: Variation of the resistivity change in per cent for the monitoring inversion results. The changes are related to the basic measurement at time 0. Blue colours indicate negative values (water saturation). Water saturation especially at the well position (red line). Damping factor $\alpha = 0.25$.

The previous figure shows how the resistivity decreases because of irrigation, seen through the blue colours. Between time step 1 and 7 a continuous increase in water content is visible, except for time 5, marked by the always darkening blue tones. At time 7 the increase is highest, which can be explained by the addition of twice the amount of water. Additionally, between time step 4 and 5 a drainage corridor could have formed, represented by the turquoise colour leading away from the dark blue ones on the left and right side. At time step 6 the corridor begins to disappear before it is completely gone at time step 7, possibly explainable by the double time needed for the pumping of two containers of water into the well. This could have led to a dehydration of the drainage area.

In comparison to Fig. 29 the following figure (Fig. 30) displays a time series resistivity change plot in per cent with a damping factor α of 1.00. In both figures the general trends stays the same, but in Fig. 30 the drainage corridor is missing. Also, the structures are smoother, since the higher damping factor tries to minimize the differences between the models at different times (see section 3.1.3).

As a conclusion of this section, even a small amount of water (72 l) can be successfully monitored with the 4point light 10W measurement device. Higher damping factors lead to a smoother time-lapse plot but also extinguishes fine structures. Therefore, for the following landfill monitoring experiments a damping factor of 0.25 is used.

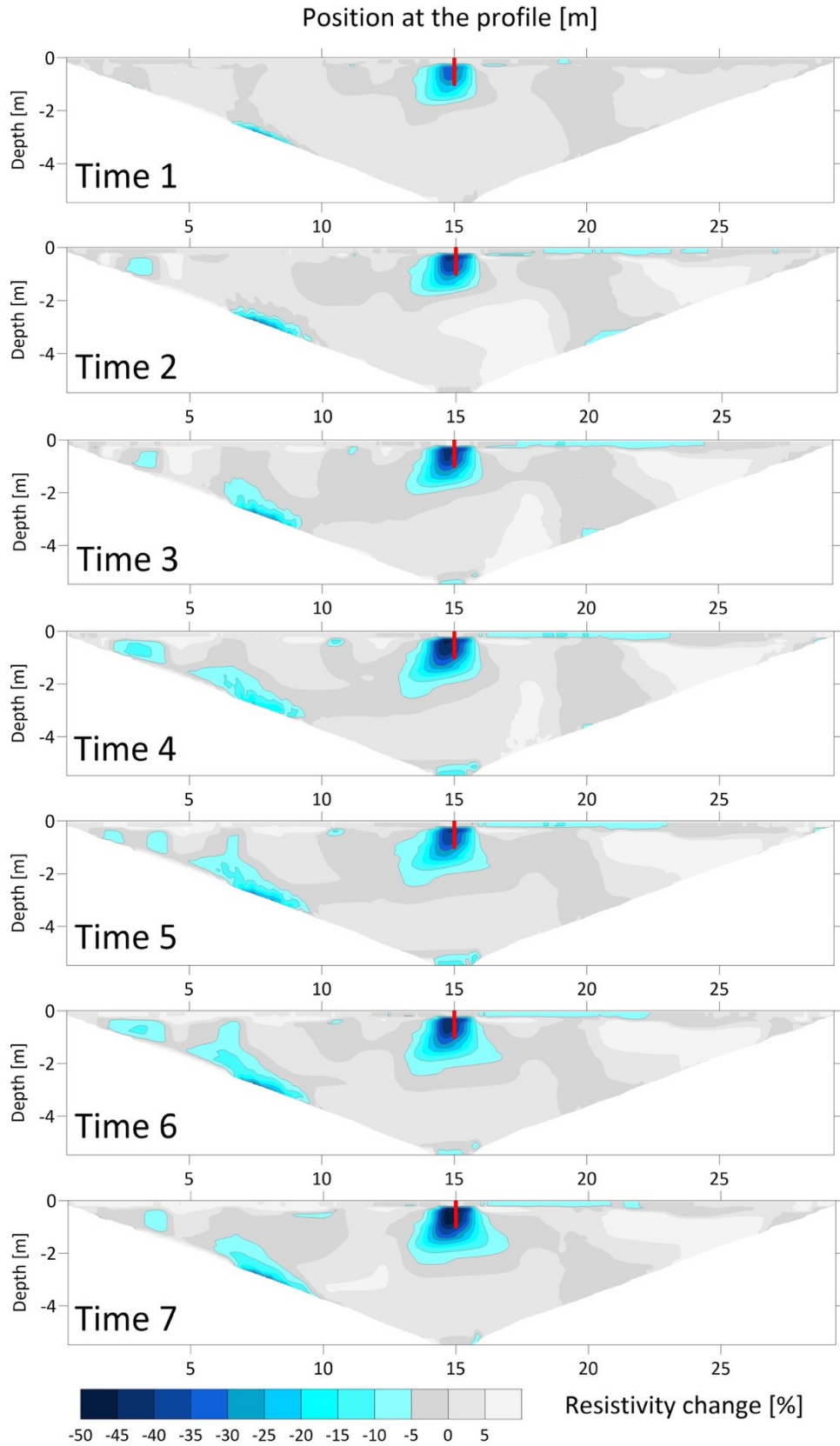


Fig. 30: Variation of the resistivity change in per cent for the monitoring inversion results. The changes are related to the basic measurement at time 0. Blue colours indicate negative values (water saturation). Water saturation especially at the well position (red line). Damping factor $\alpha = 1.00$.

3.2.6 Conclusion of the measurements in Gams

This section demonstrated a brief step by step process for the right array configuration of the landfill measurements and monitoring. Starting with a detailed statistical evaluation, over an error analysis for pole-dipole measurements up to a comparison of inversion results. Overall, the statistical values are good for all array types and profiles. However, the PDP measurements show higher error values for a homogenous subsurface, leading to the detailed analysis of this array type. Within this analysis, it can be demonstrated that these errors are not bounded to a depth level, to a specific electrode number or to a defined electric current value. This leads to the assumption that the errors are randomly distributed and cannot be improved to obtain fewer errors. Since this is the case the pole-dipole measurements are not suitable for the Rautenweg landfill survey campaign. The other three array types (Wenner, Schlumberger and Dipole-Dipole) are suitable. All of them indicate similar inversion results, according to their specified strengths. The Dipole-Dipole array resolves horizontal resistivity changes best, followed by the Schlumberger and Wenner array. But all of them show the same structures and are therefore applicable for the landfill survey, whereas the Wenner array is the preferred choice, since the signal to noise ratio is the best.

In addition, this chapter includes a model water monitoring experiment. With this it was tested if even a small amount of introduced water can be successfully monitored with the 4point light 10W device in the Wenner array configuration. As seen in section 3.2.5 the experiment was highly successful and thus the measurements at the landfill were carried out with the same settings.

3.3 Rautenweg landfill

3.3.1 General site description

The Rautenweg landfill (Fig. 31) is situated in the northern part of Vienna, approximately 10 km away from the city centre at the boarder to Lower Austria. It is the only municipal landfill of Vienna and has a trapezoid shape and covers an area of 58.8 ha. Originally the site was used as a gravel pit and on the 26 of June 1961 (MA48, 2013) the landfill was put into operation. Since 1997 it was operated as a mass-waste landfill and after it's reclassification in 2009 as a residual-waste landfill. From this point on, only treated residues from Vienna's waste incineration plants in form of ash and slag concrete were deposited (MA48, 2013). In 2014, the environmental impact assessment "Safe Disposal Rautenweg Landfill" was successfully implemented leading to an increase of the approved deposit volume from 11 Mio m³ to 23.3 Mio m³ (Lorber, 2010). Also the approved final height was increased from 45 m above ground level to about 75 m above ground level (Lorber, 2010). This makes it the largest landfill in Austria.

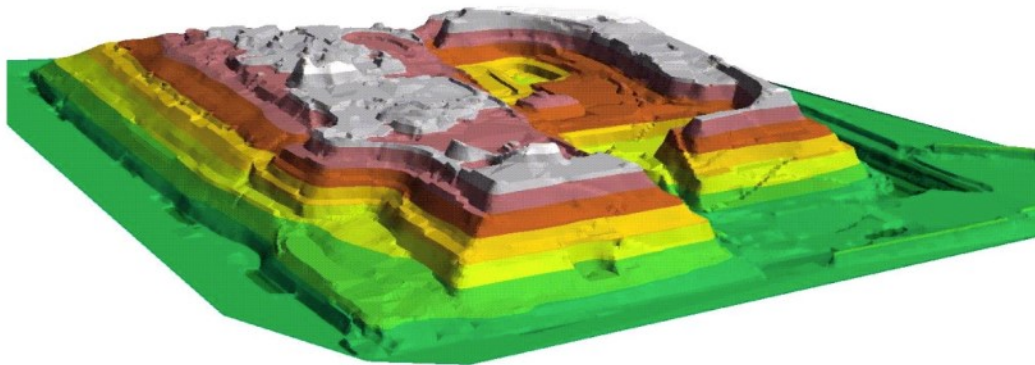


Fig. 31: Model of the Rautenweg landfill (Lorber, 2010).

In 1986, the landfill was secured with the Vienna sealed-wall chamber system, thus it has no base sealing. In Fig. 32 the general principle of the Vienna sealed-wall chamber system is displayed. Two sealing walls with a distance of eight meters between them were installed around the landfill, marking their limits. The lower ends of the walls extend into the aquiclude leading to a separation between the ground water and landfill leachate water. The

space between the two walls is subdivided into 49 sealed-wall chambers through transverse barriers (MA48, 2013). To guarantee the tightness, each wall is annually checked. Additionally, to ensure that no leachate water can escape into the ground water the water level inside the sealed-wall chamber system is being hold with pumps 1 m below the surrounding ground water. This creates a hydraulic gradient and water can just flow from outside into the landfill.

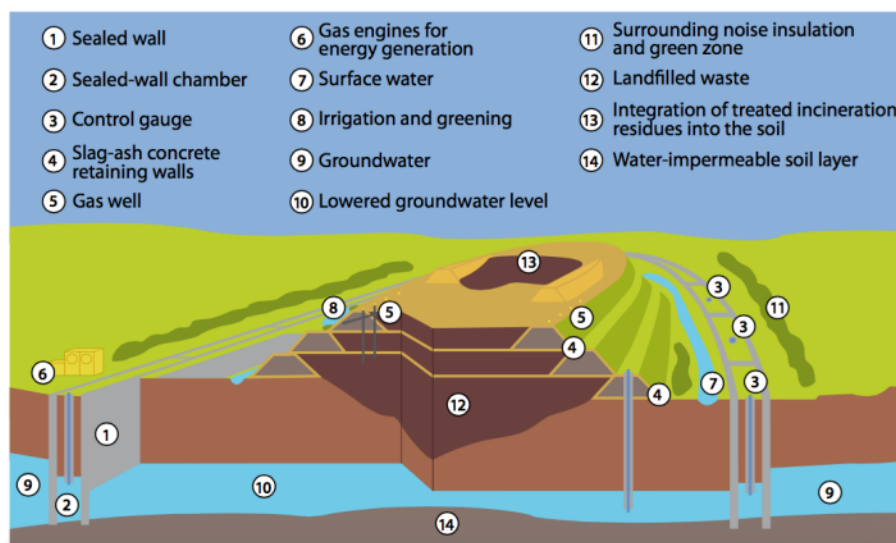


Fig. 32: Schematic representation of the Vienna sealed-wall chamber system at the Rautenweg landfill (MA48, 2013).

As mentioned in chapter 2.1 any municipal solid waste landfill produces biogas as a result of decomposition processes. At the Rautenweg landfill this happens in the old domestic waste deposits, which were deposited before 2009. After this time, the new gas-formation potential is zero (Lorber, 2010) because from that date on only ash and slag concrete were dumped. However, the landfill is still degassing today from the pre 2009 waste deposits, but the gas volume is decreasing each year. In the ÖNORM S 2084 the degassing arrangements are defined. At the Rautenweg landfill this is done since 1991 with a landfill gas registration system (Lorber, 2010). The landfill gas is extracted and utilized with an active degasification plant which consists of gas wells, gas manifolds and gas compressor stations (MA48, 2013). At most of the well locations there are two gas wells with different depth levels to collect also gas which is separated through false ceilings. Each gas well is composed of a steel filter pipe (Fig. 33) surrounded by gravels at the bottom, followed by sand and a bentonite barrier

layer at the top (Lorber, 2010). The obtained gas is transported to a power generation plant and the generated power is fed into the electricity network.

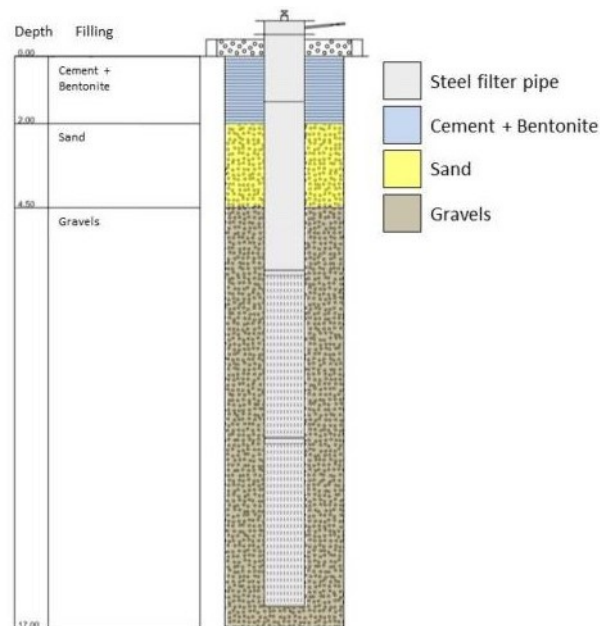


Fig. 33: Gas well GB76 3-16, which exemplifies the design of the gas wells. (Modified after: Implenia Baugesellschaft m.b.H., 2016).

The landfill offers many animals (deer, hare, crows, crested lark, Pinzgauer goats and many others) and plants a unique habitat. Probably the most prominent animal that lives on the landfill is the Pinzgauer goat (Fig. 34). They were settled in the 1990s because they were threatened with extinction in Austria and only 200 were left in the wild (MA48, 2013). Another example is the crested lark; a bird which is protected after the Vienna Nature Conservation Act in the whole urban area. Also plants, for example the burr medick (which is on the red list of threatened plants) appear at the landfill.



Fig. 34: Pinzgauer goats at the Rautenweg landfill. The right picture demonstrates how curious these animals are.

3.3.2 Survey campaigns and measurement device settings

Overall 9 profiles (Fig. 35) have been measured at the landfill within different stages. The first pilot measurements took place in December 2017. Their aim was to prove the suitability of ERT measurements on the landfill, which was successful. At this time, the first three profiles (RW 1 to RW 3) with different array configurations (Wenner-, Schlumberger- and Pole-Dipole) have been measured. Even at this time the Pole-Dipole measurements produced many errors which led to a detailed statistical error analysis at the test site Gams in March 2018 (section 3.2.3) and to an exclusion of this array type in the further project steps. The second measurements were performed in April 2018. Five more profiles (RW 4 to RW 8) have been measured in the southern part of the landfill to identify wet and dry areas in the subsurface and subsequently select profiles for the monitoring. Based on the knowledge from the test measurements in Gams only, the Wenner-, Schlumberger- and Dipole-Dipole array configurations were used. The last two measurement campaigns with the water flow path monitoring were performed in May and June 2018 (RW 1, RW 6 and RW 7). Additionally, in May 2018 a ninth profile has been measured.

All nine profiles are 200 m long, except profile RW 7 (170 m long) and the monitoring profile RW 1 (250 m), and have 100 electrodes. The conditions for the measurements were quite challenging, because of a concrete top layer (Fig. 36a). Therefore, nearly each electrode skewer at profiles RW 1, RW 2, RW 6, RW 7, RW 8 and RW 9 had to be drilled into the ground. Since this was the case, also each electrode had to be watered (Fig. 36b) to obtain

better contact resistances. In addition, the Pinzgauer goats are very curious (Fig. 34) and thus it was not possible to perform monitoring measurements overnight. As described in section 3.1.1 the measurement device was the 4point light 10W instrument from Lippmann geophysical instruments. The used settings were default ones, except the number of readings for one measurement. This was changed to a value of 10.

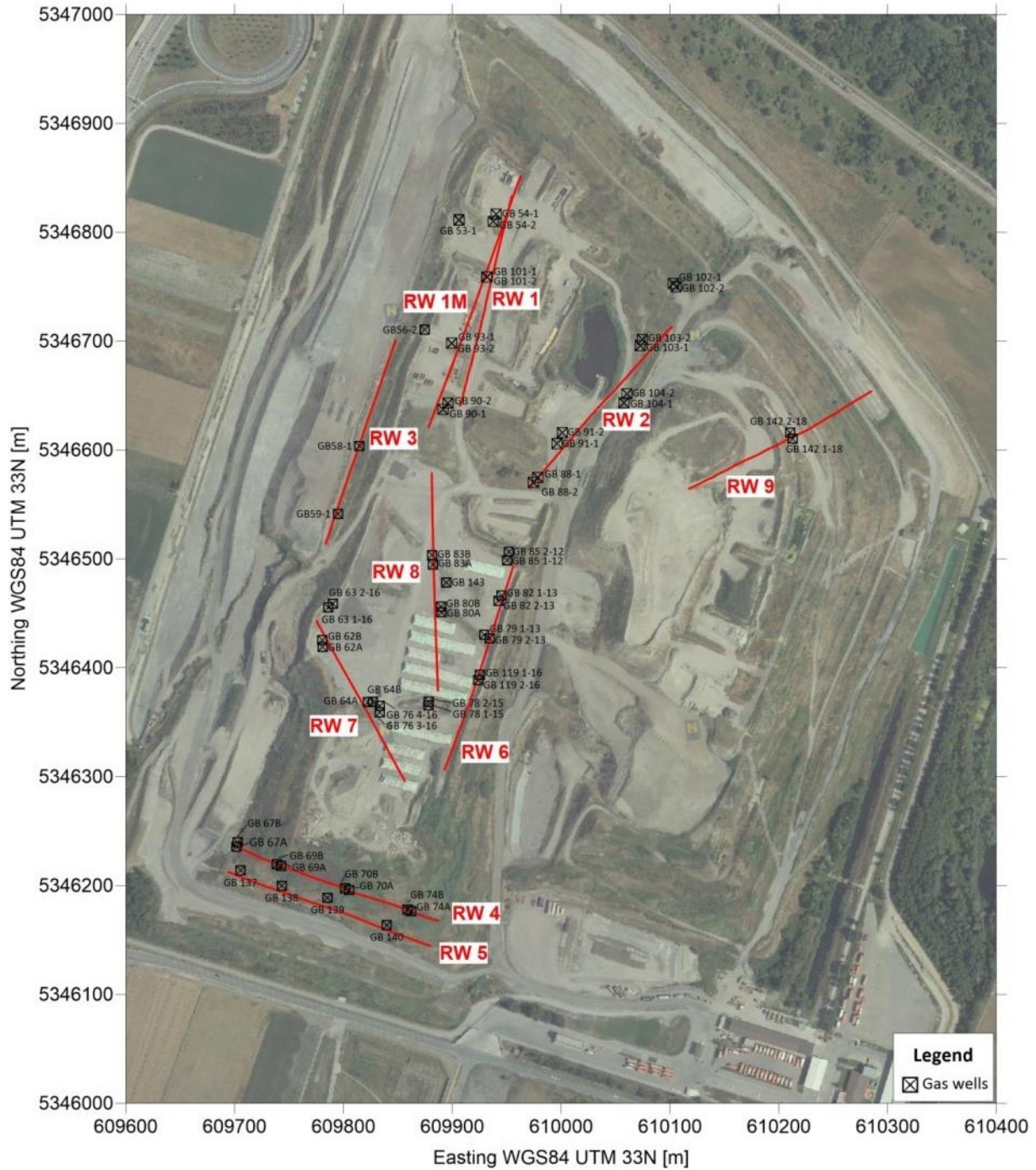


Fig. 35: Position of the nine profiles at the Rautenweg landfill. Additionally the locations of the gas wells are marked with black rectangles. (Base map: Digitaler Atlas GIS Niederösterreich (December 2017)).

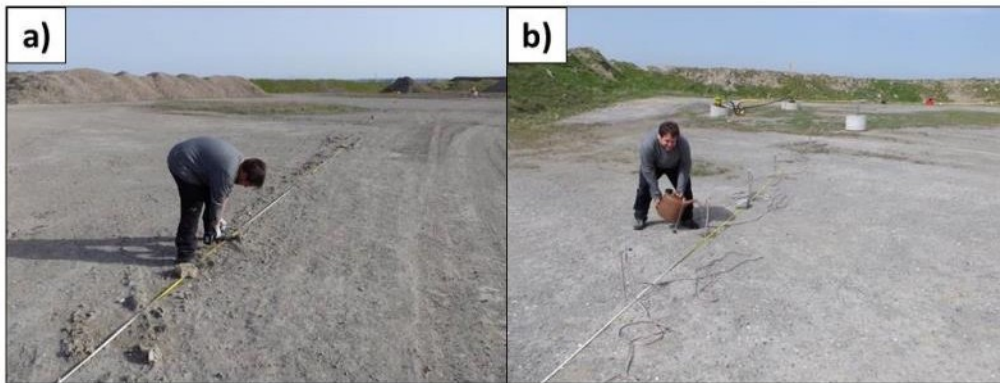


Fig. 36: (a) Electrode skewers which had to be drilled into the concrete top layer at profile RW 8. Two gas wells are visible in the background. (b) Watering of the electrode skewers to obtain better contact resistances.

3.3.3 Evaluation of raw data – measurement errors and apparent resistivities

3.3.3.1 Statistical evaluation

The measurements at the landfill were conducted, based on the knowledge from the test site Gams, with the Wenner, Schlumberger and Dipole-Dipole array, except for profile RW 1 to RW 3. At these three profiles additionally Pole-Dipole measurements, with less success, were performed, which led to the detailed analysis of this array type in Gams. The Dipole-Dipole measurements in Gams showed good results, but failed completely at the landfill. The other two configurations (Wenner and Schlumberger) consistently show good results, with the best results for the Wenner array. However, this is not surprising, as it has the best signal to noise ratio (section 2.2.1) and thus it is well suited for heterogeneous conditions as it is the case at landfills. Since the lowest error values have been obtained by using the Wenner array configuration, the Box-Whisker plot (Fig. 37) of the nine profiles shows only the measurement errors (dU in %) for this array type. The plot displays good mean values of the error between 0.11 % and 0.34 % respectively. Values above $Q3 + IQR \cdot 1.5$ are defined as outliers and values over 2 % will be neglected in further processing steps of the data because they are not representable. A more detailed statistical evaluation is presented in Appendix A (Tab. 12 and Tab. 13). Furthermore, there the minimum-, maximum-, mean-, standard deviation-, median- and amount of negative resistivity values of the measurement errors

and measured resistivities are displayed. Also, these tables show the results for the Schlumberger, Pole-Dipole and Dipole-Dipole measurements. Since the best results were achieved with the Wenner array, only this is used for the inversion and further evaluation of the data.

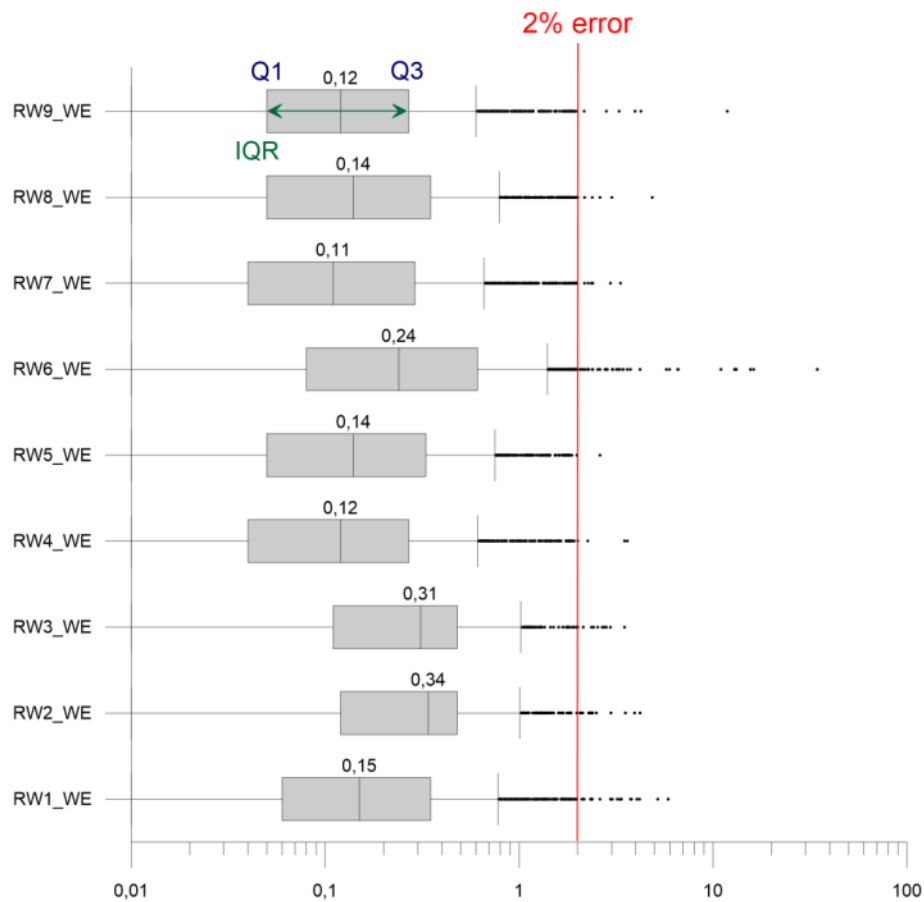


Fig. 37: Box-Whisker plot of the measurement error dU (%) for profiles RW1-RW9. The median is displayed in all nine profiles. Values over $Q3 + IQR \cdot 1.5$ are defined as outliers. (Abbreviations: Q1 = lower quartile; Q3 = upper quartile; IQR = interquartile range; WE = Wenner array).

3.3.3.2 Effects of gas wells on the measurements

Since the gas wells consist of a steel filter pipe they could affect ERT measurements, if the profile is too close to such a well. This effect can be demonstrated with the two profiles RW 4 and RW 5. Both profiles are located in the most southern part of the landfill where there have been no changes for years, as the final structure of the landfill has been reached. The profiles are parallel to each other with a spacing of approximately 15 m at different sea levels. The difference between them is roughly 5 m. Furthermore, at both profiles gas wells

are located but with a different distance between the wells and the profile. At profile RW 4 the distance is only a few centimetres, whereas the distance at profile RW 5 is between 5 m and 8 m.

Fig. 38 represents the apparent resistivity section of profile RW 4 and Fig. 39 the apparent resistivity section of profile RW 5. In both sections the uppermost levels indicate the same trend: a relatively high resistivity zone, which is interrupted in profile RW 4, and a transition zone (yellow colours) to a very low resistivity zone. However, the low resistivity zone in greater depths is different. In profile RW 4 this zone is disturbed by three pants-leg structures, while in profile RW 5 this part is totally undisturbed. Since both profiles are located in the same unaffected area, the only difference between them is the distance to the gas wells. Also, the positions of the gas wells on the profile RW 4 are in a good agreement with the position of the pants-leg structures. Therefore, the assumption is that the pants-leg structures in profile RW 4 are caused by the gas wells.

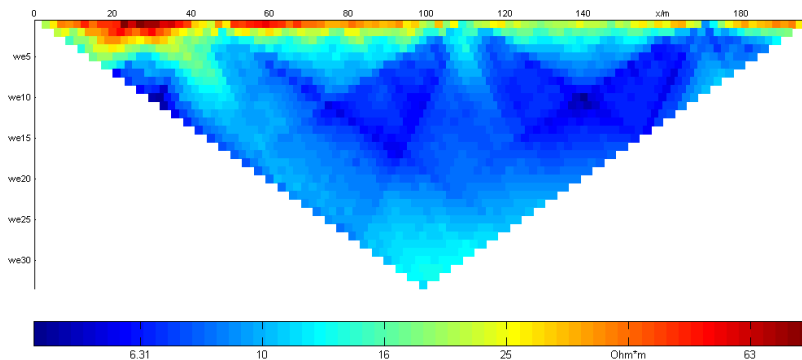


Fig. 38: Apparent resistivity section of profile RW 4 with pants-leg structures caused by the insufficient distance between the profile and the gas wells.

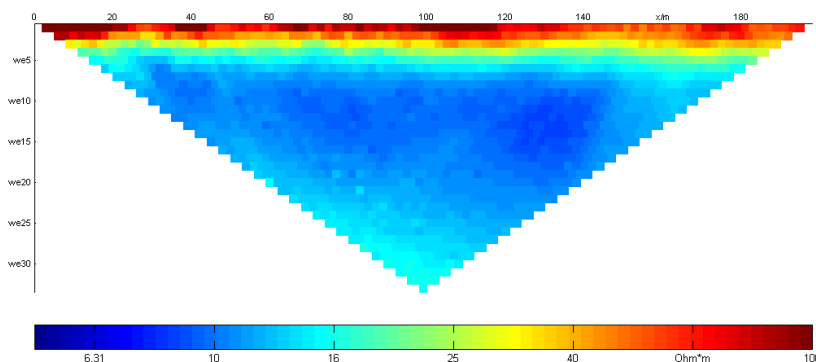


Fig. 39: Apparent resistivity section of profile RW 5. Since the distance is big enough between the profile and the gas wells, no pants-leg structure occurs.

3.3.4 Inversion results

The inversion of the profiles was carried out with the software RES2DINVx64 with different inversion parameters for each one. However, the model discretization (small model cells), the forward modelling method parameters (fine mesh) and the inversion method (robust data constraints) remained almost the same. The exact parameters used are located digitally on an enclosed USB stick. Additionally for each profile, different inversion parameters were used to estimate the smallest differences between the measured apparent resistivity pseudosection and the calculated apparent resistivity pseudosection. In Tab. 6 the RMS errors for the final results of each profile after the fifth (RW 1 to RW 3) and seventh (RW 4 to RW 9) iteration step are displayed.

Profile	RW 1	RW 2	RW 3	RW 4	RW 5	RW 6	RW 7	RW 8	RW 9
RMS error [%]	2.15	3.14	1.99	3.13	1.18	4.69	1.29	2.51	2.57
Iteration	5	5	5	7	7	7	7	7	7

Tab. 6: RMS errors for the RES2DINVx64 inversion steps.

Fig. 40 and Fig. 41 exemplify the differences between the different inversion parameters for one profile based on profile RW 4. The major differences between these two figures are the damping factor and the ratio between the vertical and horizontal flatness filter. With a higher weight of the vertical filter it is possible to optimize the inversion parameters for vertical structures. The other way around by using smaller weights it is possible to optimize the inversion parameters for horizontal structures. In the inversion parameters for Fig. 40 less weight was given to the vertical filter in comparison to the inversion parameters of Fig. 41, which can be seen in Tab. 7.

Inversion Parameter	RW4_WE	RW4_WE_1
Profile	4	4
RMS error [%]	3.1	3.7
Weight of the vertical filter	0.9	1.85

Tab. 7: Major difference of the inversion parameters at profile RW 4.

Both figures represent the same general trend: a good approximation of the calculated apparent resistivity pseudosection to the measured one and three very low resistivity zones in the upper part of the inverse model resistivity section.

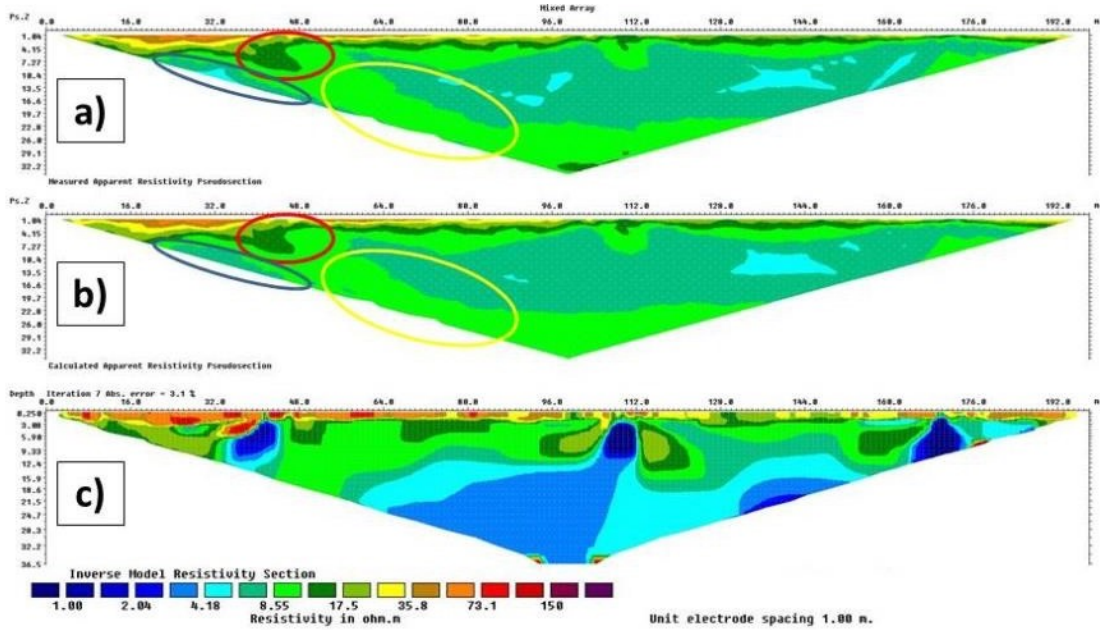


Fig. 40: (a) measured apparent resistivity pseudosection, (b) calculated apparent resistivity pseudosection and (c) inverse model resistivity section of profile RW 4 with used RW4_WE inversion parameters.

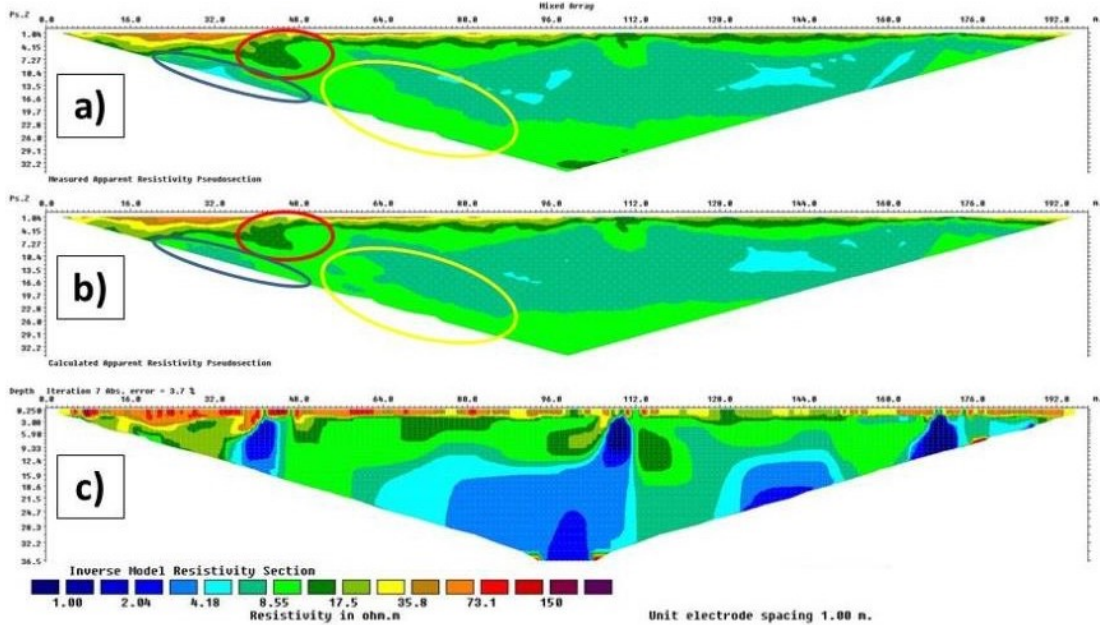


Fig. 41: (a) measured apparent resistivity pseudosection, (b) calculated apparent resistivity pseudosection and (c) inverse model resistivity section of profile RW 4 with used RW4_WE_1 inversion parameters.

While comparing both figures, it turns out that the approach of the calculated apparent resistivity pseudosection to the measured one is better in Fig. 40. This can be seen at zones marked with a coloured circle. The area marked with a red circle indicates a triangular shaped resistivity zone (dark green). This shape is a little bit bigger in Fig. 40, than in Fig. 41 and hence better modelled in comparison to the measured pseudosection. Also, the area marked with a blue circle is better modelled in Fig. 40. This is the case, because the 7 Ohmm resistivity zone extends longer over the lower edge of the pseudosection as it is also the case in the measured apparent resistivity pseudosection. The last and most obvious structure is marked with a yellow circle. Here the 7 Ohmm resistivity zone in Fig. 41 is modelled to big in comparison with the measured apparent resistivity pseudosection. In addition two small 7 Ohmm resistivity zones are created at the left boarder of the circle. Based on these three areas and on the lower RMS error for the modelled section with the parameter RW4_WE, Fig. 40 indicates the better result compared with the parameters RW4_WE_1. Thereby, the description of the modelled resistivity section is only conducted for Fig. 40. In the upper three meters a relative high, partially interrupted, resistivity zone is located. A medium resistivity zone indicates a transition zone, before the resistivity becomes low in greater depths. In this transition zone, additionally three very low resistivity zones are located. These zones correspond well with the locations of the gas wells and are therefore most likely inversion artefacts of the pants-leg structures seen in Fig. 38, as their extension is too wide for a steel pipe of the gas wells.

In addition to the resistivity measurements, IP measurements were executed at each profile. Since the steel filter pipe of the gas wells and the surrounding subsurface consists of different materials an IP effect should theoretically be visible. In Fig. 42 the result of the IP inversion for profile RW 4 is represented. In the measured phase angle section a pants-leg structure is visible (dotted white line) which corresponds with the location of the gas well at around 35 m. However, this structure is no longer recognizable in the modelled section. Instead another structure appears at profile meter 176 (marked with the red circle). This one coincides perfectly with the gas well at this position. However, the other two gas wells are unfortunately not detectable at the modelled section.

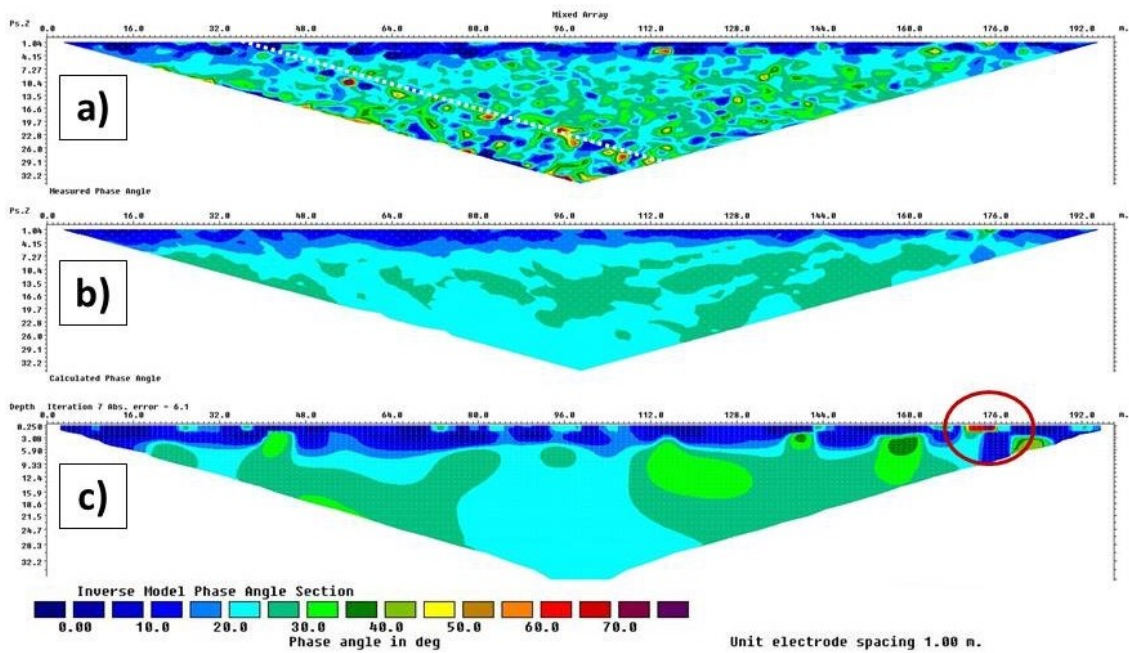


Fig. 42: IP inversion results for profile RW 4. (a) Measured phase angle, (b) calculated phase angle and (c) inverse model phase angle section.

Such comparisons described above were performed for each profile to obtain the best results which represent the measured data. In Appendix A (Fig. 57 to Fig. 64) the final inversion results for the remaining profiles are presented.

3.3.5 Conductivity display of the inversion results

The inversion results from RES2DINVx64 were exported into the Surfer software format from Golden Software. Afterwards they were gridded with the “Triangulation with linear interpolation” algorithm to create a grid which can be used by the program Surfer. This process was done in order to display the electrical conductivity and determine the corresponding water content at different temperature levels, since the conductivity is temperature dependent (Grellier et al., 2006; Hayley et al., 2007). In order to create these plots, however, the measured leachate water conductivity was first converted to specific temperature levels.

Therefore, a laboratory experiment was carried out to establish a temperature conductivity relationship. Thus, two leachate samples were taken at the Rautenweg landfill in Vienna:

one of the fire pond and the other of the inner pipe 2 (Fig. 43a). Following, the experimental setup (Fig. 43b) and procedure is explained, which was the same for each sample.

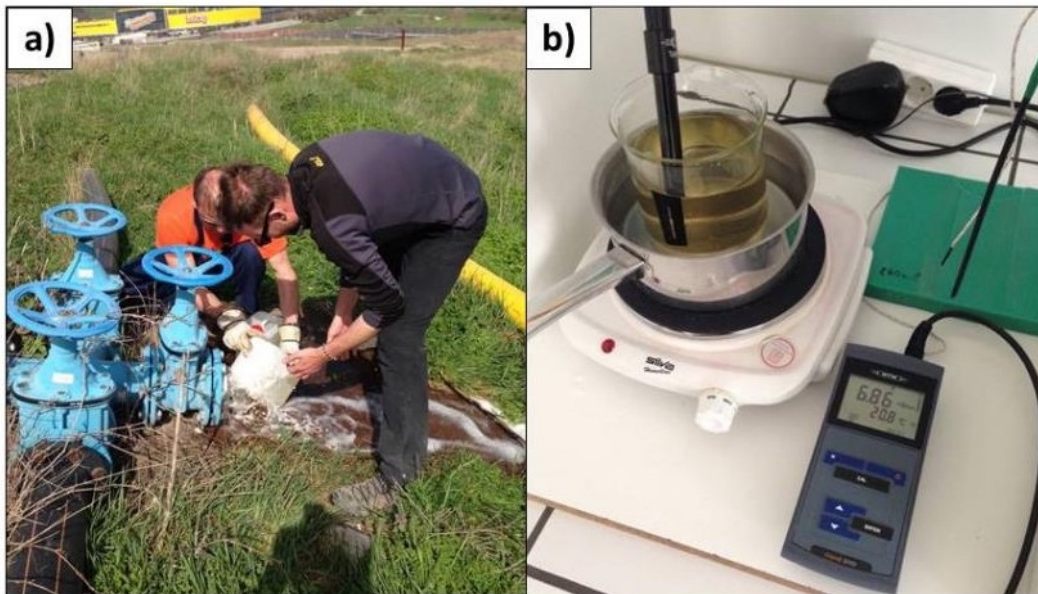


Fig. 43: (a) Leachate water sample collection at the inner pipe 2. (b) Experimental setup for the determination of the relationship between temperature and conductivity.

The samples were heated manually from 20°C to 80°C via a hot plate in a beaker. Additionally, the beaker was situated in a pot which was filled with tap water. This procedure was performed to guarantee that no conductivity is induced from the pot into the leachate water samples. To control the temperature and conductivity the conductivity measuring cell “TetraCon 325” from WTW (Wissenschaftliche Technische Werkstätte) was connected to the compact precision conductivity meter “Cond 3110” from WTW. Since the conductivity meter automatically applies a nonlinear temperature compensation, the measured conductivity values are related to the reference temperature at 25°C. Thus, these values have to be transformed from their reference temperature to the actually measured temperatures. This was not exactly feasible, because the temperature compensation curve used in the conductivity meter is internal knowledge from WTW. An alternative is the equation after the ÖNORM EN 27888,

$$EC = [1 + a * (t - 25)] * EC_{25} \quad (10)$$

where EC is the electrical conductivity at temperature t , EC_{25} the electrical conductivity at the reference temperature and a the temperature coefficient of the electrical conductivity. The value EC_{25} was obtained by measuring the two samples before and after heating at 25°C and calculating a mean value out of it. For the temperature coefficient a mean value of the experiments from Grellier et al. (2006) was used. In Fig. 44 the conductivity after transformation is displayed as a function of temperature.

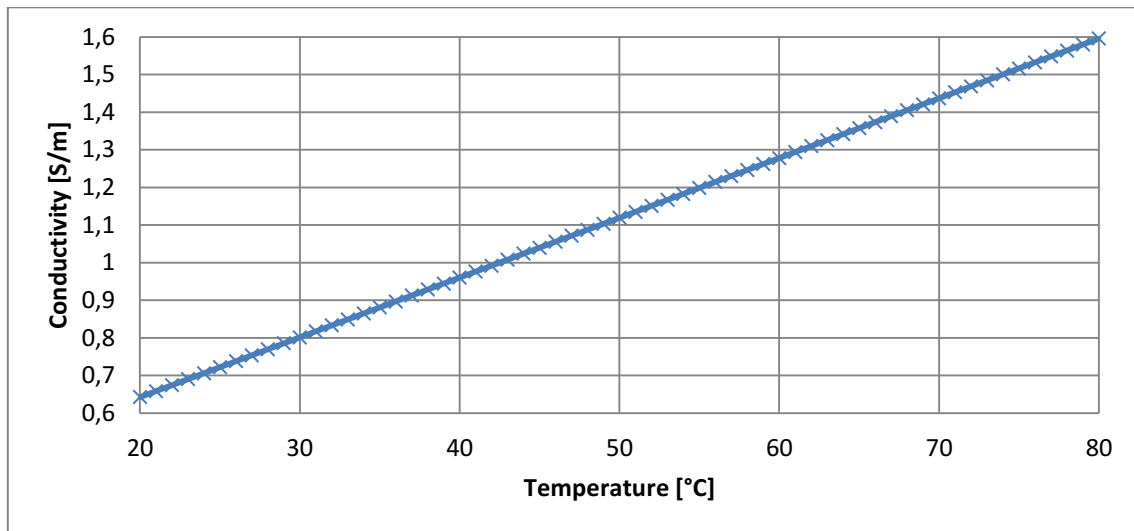


Fig. 44: Conductivity vs. temperature for the mean value of the two leachate water samples calculated after ÖNORM EN 27888. The temperature coefficient was set to 0.022.

Since the conductivity is temperature dependent and the temperature inside the landfill was not exactly determinable the measured ERT conductivity is displayed with four different conductivity scales in the following plots. These scales correspond to the lowest, two intermediate and highest expected temperatures in landfills (see section 2.1) and were used for water content estimations. The maximum value of the respective scale represents the conductivity value of the temperature compensated leachate water samples. In figure (a) the temperature level of 20 °C is displayed. Here a conductivity of 0.643 S/m marks a water saturation of 100 %. At 30 °C a conductivity value of 0.801 S/m (b) represents a water saturation of 100 %. Figure (c) displays a temperature level of 40 °C where 0.960 S/m indicates a water saturation of 100 %. In the last figure (d) the temperature is 55 °C which leads to a conductivity value for water of 1.199 S/m according to the temperature compensation. In all four plots (a – d) the absolute measured ERT conductivity values stay the same and only the colour scale changes. Also a conductivity of 0.0 S/m represents a

water saturation of 0 %. Between the maximum and minimum water saturation the values were interpolated linearly, because no additional data (in situ samples of the landfill waste) was available for the estimation of the water saturation after Eq. 6.

In the subsequent figures only the three profiles (RW 1, RW 6 and RW 7) which were monitored later and profile RW 4 are displayed. The results of the other five profiles are visible in Appendix A (Fig. 65 to Fig. 69).

Along the horizontal axis the positions in the profile and along the vertical axis the depth can be seen. Reddish colours represent less conductive and therefore rather dry and bluish colours represents high conductive and thus rather moist to saturated areas. Furthermore, the water saturation range between 30 % and 55 % is marked, which represents the optimum range for methane production.

Profile RW 1

This profile is located in the most northern part of the landfill and was measured on 14/12/2017. It is 200 m long with an electrode spacing of 2.00 m and elongates from north to south. Profile RW 1 (Fig. 45) exhibits in all temperature intervals a non-conductive top layer with an extension between 5 m to 10 m. North and south of the gas wells GB 101-1 and GB 101-2 two conductive structures are located. These indicate water saturations above 55 % at a temperature of 20 °C and water saturations between 30 % and 55 % for a temperature of 55 °C. Between these two temperatures the water saturation is constantly decreasing with increasing temperature. Around the gas wells GB 93-1 and GB 93-2 water saturations between 30 % and 55 % occur at a temperature of 20 °C. This saturation is below 30 % for temperatures above 55 °C. However, at the positions of the gas wells the water saturation is below 30 % for the expected temperature range in landfills and therefore these areas are to dry.

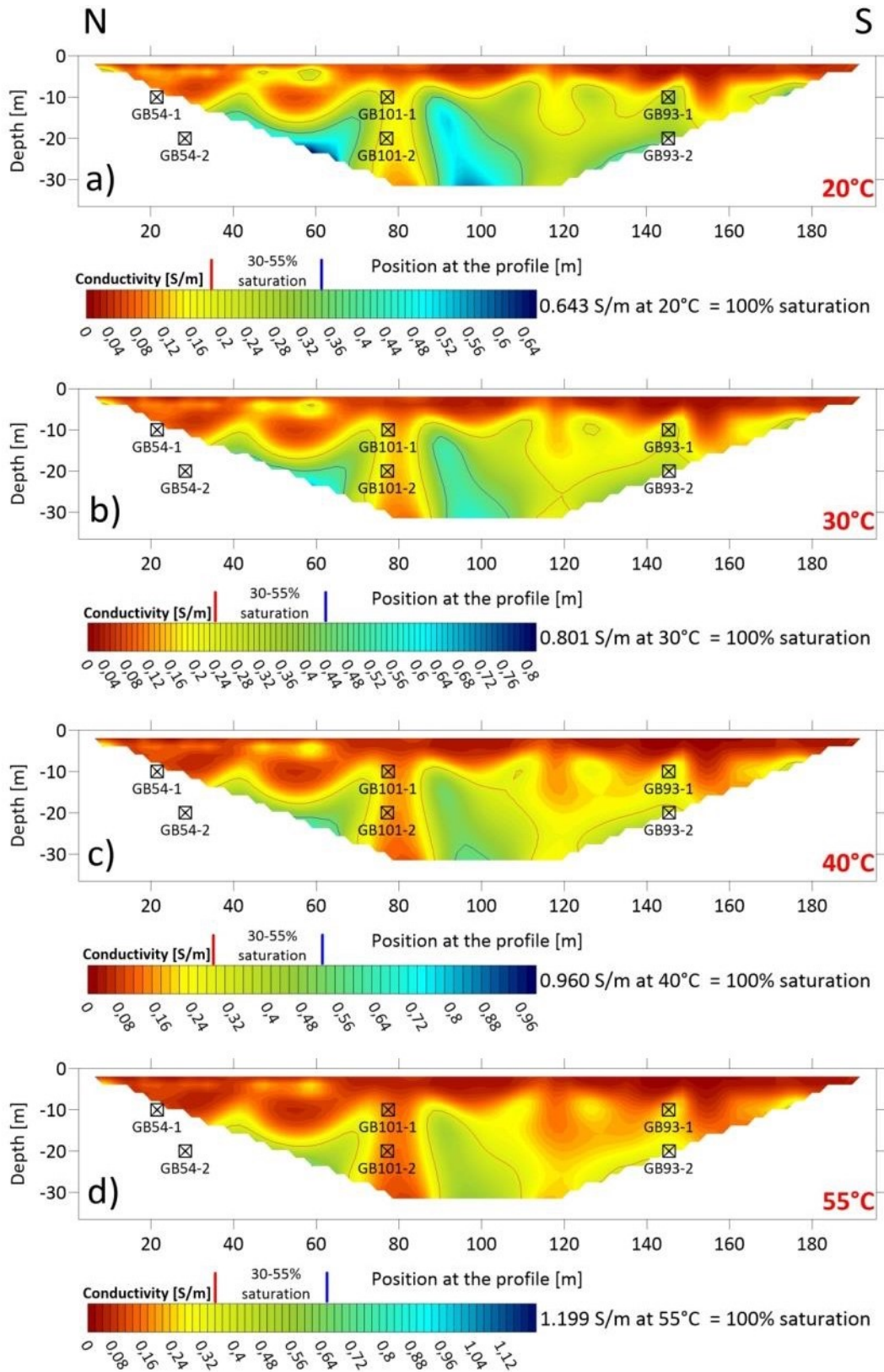


Fig. 45: Variation of the conductivity [S/m] along profile RW 1 with conductivity scaling at (a) 20 °C, (b) 30 °C, (c) 40 °C and (d) 55 °C. The maximum value of the conductivity corresponds to 100% water saturation and a conductivity of 0 S/m equates to a water content of 0%. The black squares mark the position of the gas wells where the depths represent the mean depth of the steel filter pipe.

Profile RW 4

Profile RW 4 (Fig. 46) is in the most southern part of the landfill and was measured on 09/04/2018. It elongates from west to east and is 200 m long. In all four temperature levels a poorly conductive top layer appears. Up to a depth of about 10 m, the inversion model shows three very conductive areas (quadratic shape) that are congruent with the positions of the gas wells. This can be explained by the fact that the iron pipes of the gas wells act as an electrical conductor and are too close to the profile. The main difference between the temperature intervals is the area of water saturation. It is striking, those areas which have a water saturation of 30 % to 55 % at 20 °C, are getting smaller and smaller from 30 °C to 40 °C and fall at 55 °C below 30 % water saturation and are therefore considered to be to dry.

Profile RW 6

In Fig. 47 the conductivity results for profile RW 6 are shown, which is situated in the middle part of the landfill, elongates from north to south and was measured at 10/04/2018. The distance from the gas wells to the profile is quite low (around 50 cm), but compared with profile RW 4 such clear gas well effects are not evident in this profile. However, in Fig. 47a, a weak effect may be recognizable around gas well GB 119 1-16. Here, a similar quadratic structure in light blue appears like in profile RW 4. In this figure two areas with a water saturation of 30 % to 55 % are visible: one below the quadratic structure and one around the gas wells GB 79 1-13 and GB 79 2-13. With increasing temperatures, these areas are getting smaller and at 55 °C the water saturation is below 30 %. Furthermore, two distinctive details are detectable. The first is, that the whole area south of the gas wells GB 119 1-16 and GB 119 2-16 represents very low conductivities at all temperature levels. The same low values are valid for the top layer and for the area northern of the gas wells GB 79 1-13 and GB 79 2-13 in Fig. 47d. The second feature is the very steep vertical structure separating the two conductive areas around gas well GB 79 1-13 and GB 119 1-16, which is visible in each figure. Like in the previous two figures the areas around the gas wells are showing to low conductivity values and are therefore to dry.

Profile RW 7

Profile RW 7, shown in Fig. 48 is the shortest of all profiles (170 m) and was measured at 11/04/2018. It is located like profile RW 6 in the middle part of the landfill and elongates from north-west to south-east. The most obvious detail of this profile is that at a temperature of 55 °C nearly the whole section indicates very low conductivity values and thus is too dry. But also in the other temperature ranges the conductivity values represent water saturations below 30 %. The second obvious structure is a very low conductivity zone in a depth of around 20 m, at profile meter 120 and situated at the lower edge of the representable triangle. And a third small structure is visible at profile meter 20 with water saturations between 30 % and 55 %. However, this structure is caused by an irrigation lance and thus only an inversion artefact.

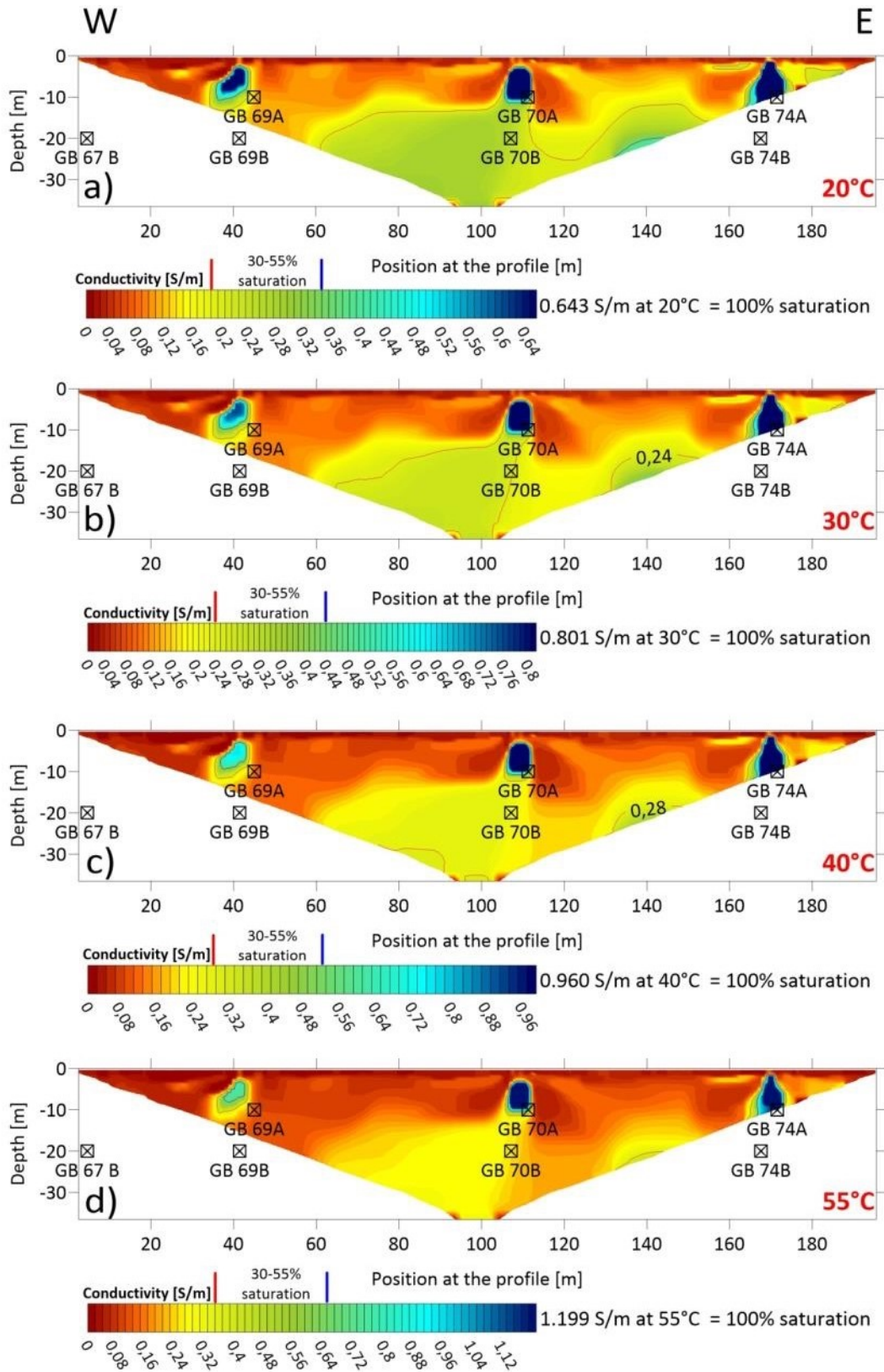


Fig. 46: Variation of the conductivity [S/m] along profile RW 4 with conductivity scaling at (a) 20 °C, (b) 30 °C, (c) 40 °C and (d) 55 ° C. The maximum value of the conductivity corresponds to 100% water saturation and a conductivity of 0 S/m equates to a water content of 0%. The black squares mark the position of the gas wells where the depths represent the mean depth of the steel filter pipe.

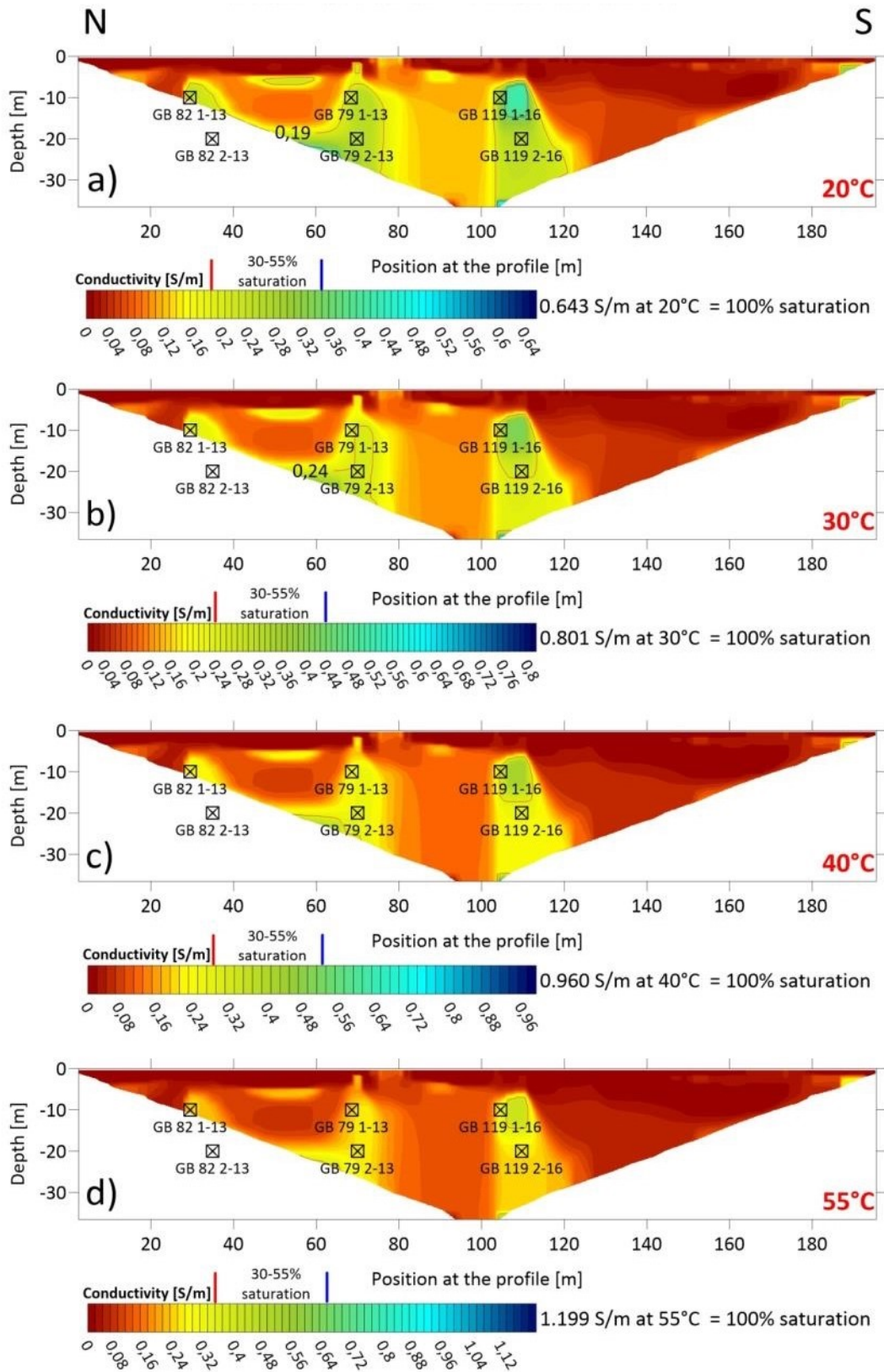


Fig. 47: Variation of the conductivity [S/m] along profile RW 6 with conductivity scaling at (a) 20 °C, (b) 30 °C, (c) 40 °C and (d) 55 ° C. The maximum value of the conductivity corresponds to 100% water saturation and a conductivity of 0 S/m equates to a water content of 0%. The black squares mark the position of the gas wells where the depths represent the mean depth of the steel filter pipe.

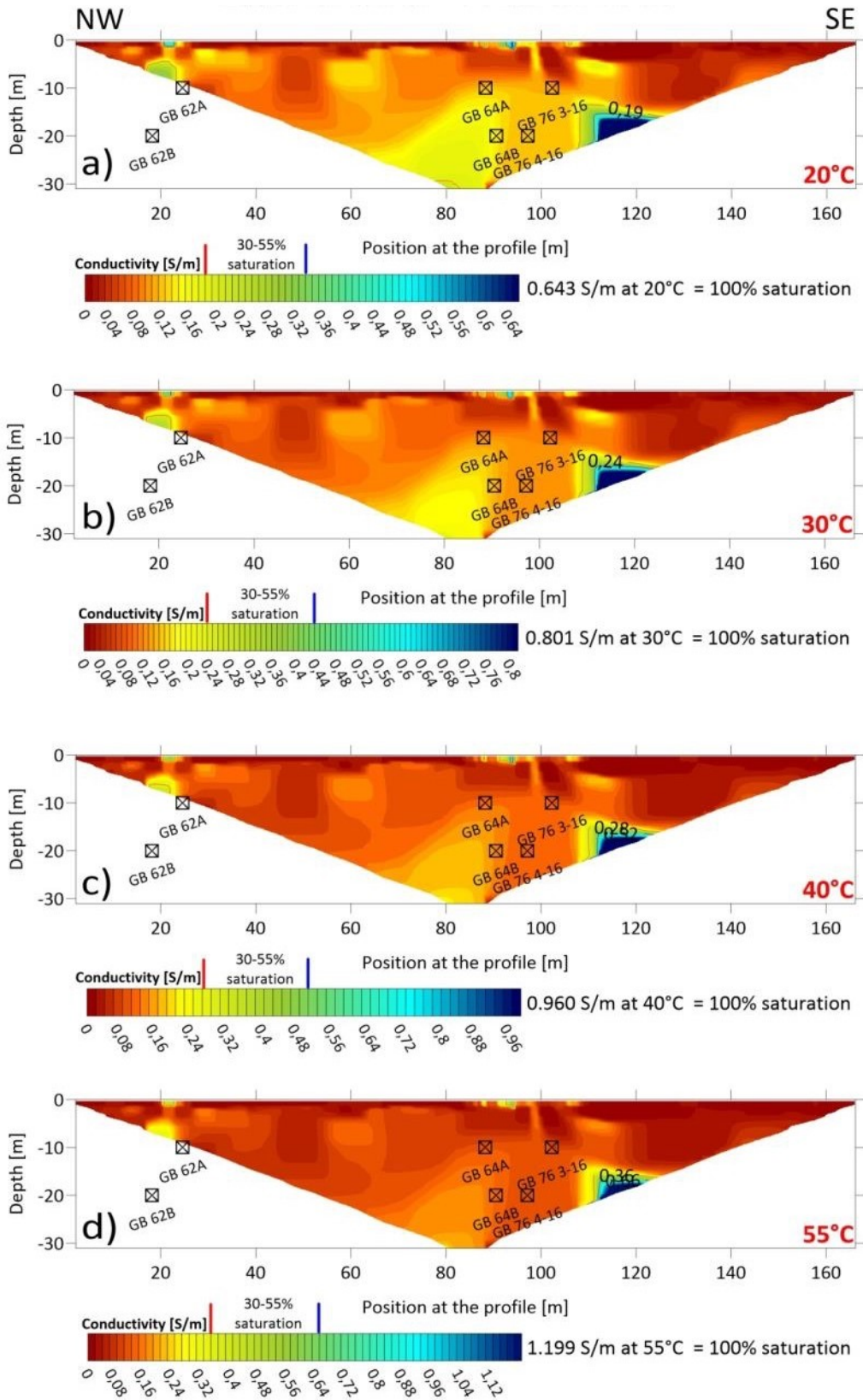


Fig. 48: Variation of the conductivity [S/m] along profile RW 7 with conductivity scaling at (a) 20 °C, (b) 30 °C, (c) 40 °C and (d) 55 ° C. The maximum value of the conductivity corresponds to 100% water saturation and a conductivity of 0 S/m equates to a water content of 0%. The black squares mark the position of the gas wells where the depths represent the mean depth of the steel filter pipe.

3.3.6 Time-Lapse measurements

Based on the finding of the previous chapter, the profiles RW 1, RW 6 and RW 7 were selected for the water flow path monitoring, since these profiles show too dry areas for a good methane production in the subsurface around the gas wells. To enhance the biogas production, water is introduced via the gas wells into the subsurface. The introduced water was monitored with time-lapse measurements to identify the water flow paths.

Profile RW 7

The first monitored profile (RW 7) was measured from 28/05/2018 until 18/06/2018 in irregular time steps (Tab. 8). The first measurement (Monitoring 0) was carried out at 28/05/2018 before the introduction of water for comparative purposes. The next 20 measurements (Monitoring 1 to Monitoring 20) were accomplished the following 4 days and measurement Monitoring 21 two weeks after the start of irrigation.

Measurement	Day	Start Time	End Time		Measurement	Day	Start Time	End Time
Monitoring 0	28.05.2018	15:38	16:46		Monitoring 11	30.05.2018	08:20	09:18
Monitoring 1	29.05.2018	08:42	09:42		Monitoring 12	30.05.2018	09:30	10:26
Monitoring 2	29.05.2018	09:57	10:56		Monitoring 13	30.05.2018	10:40	11:37
Monitoring 3	29.05.2018	11:12	12:12		Monitoring 14	30.05.2018	11:50	12:50
Monitoring 4	29.05.2018	12:27	13:29		Monitoring 15	30.05.2018	13:00	14:00
Monitoring 5	29.05.2018	13:38	14:36		Monitoring 16	30.05.2018	14:10	15:13
Monitoring 6	29.05.2018	15:24	16:28		Monitoring 17	30.05.2018	15:20	16:21
Monitoring 7	29.05.2018	16:39	17:41		Monitoring 18	30.05.2018	16:30	17:38
Monitoring 8	29.05.2018	17:43	18:39		Monitoring 19	31.05.2018	09:08	10:09
Monitoring 9	29.05.2018	18:53	19:47		Monitoring 20	01.06.2018	09:09	10:04
Monitoring 10	30.05.2018	07:10	08:12		Monitoring 21	18.06.2018	13:00	14:04

Tab. 8: Times for the time-lapse measurements with the start and end time for each measurement.

The irrigation of the gas well GB76 3-16 took place from 29/05/2018 until 30/05/2018: on the first day from 08:10 to 17:10 and on the second day from 08:20 to 14:00 with an overall volume of 714 m³ of water. The water was provided from the inner well 4 which is in the south-western part of the landfill and pumped via a fire hose into the gas well (Fig. 49a).

Additionally, the conductivity and temperature of the introduced water were monitored directly in the field (Fig. 49b), with the conductivity meter “Cond 3110” from WTW and the results are depicted in Tab. 9.

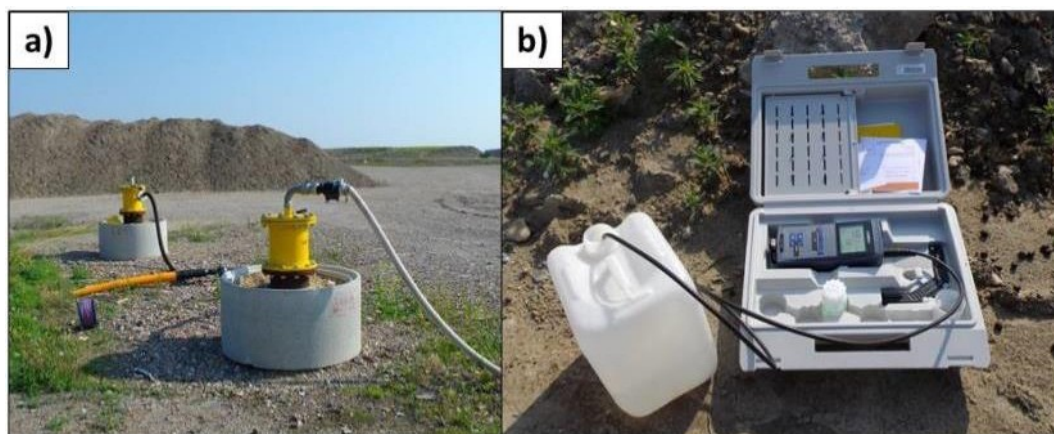


Fig. 49: (a) Gas well GB76 3-16 with the fire hose and water counter for the introduction of water from the inner well 4. (b) Conductivity meter “Cond 3110” for temperature and conductivity control of the introduced water.

Measurement	1	2	3	4	Mean value
Day	29.05.2018	29.05.2018	29.05.2018	30.05.2018	
Time	09:00	10:15	16:30	08:53	
Conductivity at 25°C [S/m]	0.0977	0.0982	0.1007	0.1002	0,0992
Measured temperature [°C]	16.0	14.6	16.9	14.7	

Tab. 9: Compensated conductivities and measured temperatures for the introduced water of the inner well 4.

The measured values of the introduced water remained nearly constant over the two days, displaying a mean value of 0.099 S/m at 25 °C. This value was temperature compensated after Eq. (10) and used as the maximum value for the conductivity display colour scale of the inversion results (Fig. 50). In Fig. 50 the inversion results of the monitoring measurements for each time step are displayed, whereby measurement Monitoring 0 indicates the original state before any irrigation. Considering the measurement was performed at the same profile as the measurement at 11/04/2018 (Fig. 48) the dominant subsurface features must remain the same. The only difference between them is the colour scale, which was modified to better highlight the different conductivity values for each monitoring measurement as a result of irrigation. Additional here the position of the gas well GB 76 3-16 is marked with a black line.

Field measurements

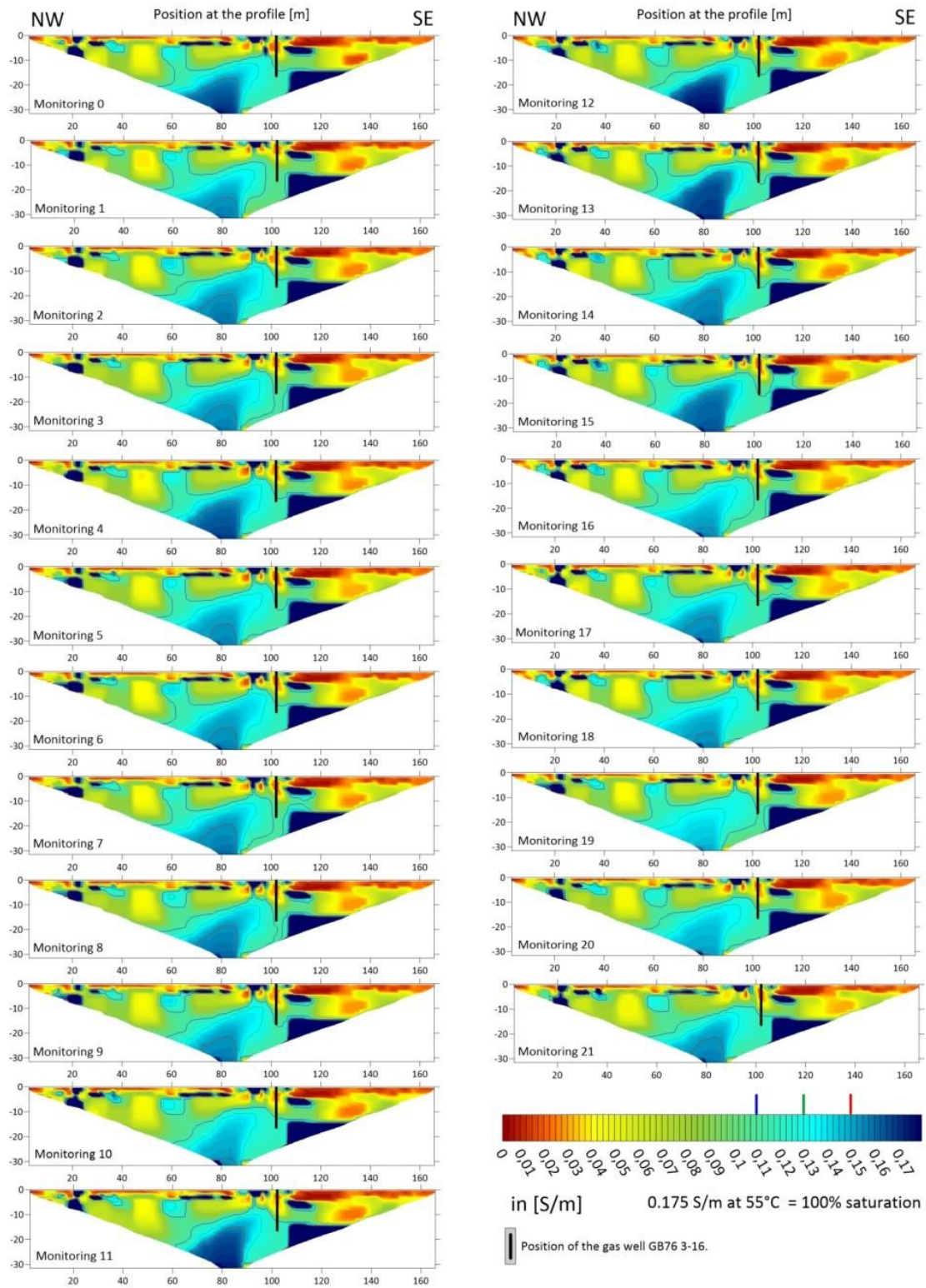


Fig. 50: Variation of the conductivity [S/m] along profile RW 7 for the monitoring measurements with a conductivity scale for 55 °C. The maximum value of the conductivity corresponds to 100% water saturation and a conductivity of 0 S/m equates to a water content of 0%.

The entire measurements indicate the same subsurface structures. Namely a very conductive zone at profile meter 20 (water lance) and profile meter 110 to 130 in a depth of about 20 m with a triangular shape at this 2D section. Further a moderate conductive quadratic structure (light yellow) at profile meter 50, a less conductive oval shaped structure at profile meter 135 in a depth of 15 m and three very shallow small structures with low conductivity at position 100 m in the profile. That's why the measurements are highly accurate and reproducible. The only small differences in the conductivity between the measurements are in the area where the water was introduced.

Since no major differences are visible in Fig. 50, Fig. 51 displays the conductivity changes in per cent. All constitute changes are related to the state before the start of irrigation (Monitoring 0). As the introduced water has a minor conductivity (0.10 S/m) compared to the one of the original state subsurface (around 0.13 S/m), the changes in conductivity around the gas well should be negative, if the original subsurface is filled with leachate water. Then the introduced water would mix with the leachate water and the conductivity change would be negative. But if the original subsurface consists of air-filled cavities the conductivity change would be positive when water is introduced.

Each single measurement indicates differences between -15 % and +15 % with no visible trend. Even between two contemporary measurements (Monitoring 1 and Monitoring 2) the trend reverses. As expected, at Monitoring 1 the conductivity change is negative, but in the following measurement (Monitoring 2) the change is positive. This behaviour is also noticeable in the following measurements (Monitoring 3 to Monitoring 20) and in the Monitoring 21 where two weeks lie between measurement and irrigation. However, the assumption would have been that with increasing time the difference becomes more visible as the introduced water heats up and gets more conductive.

Field measurements

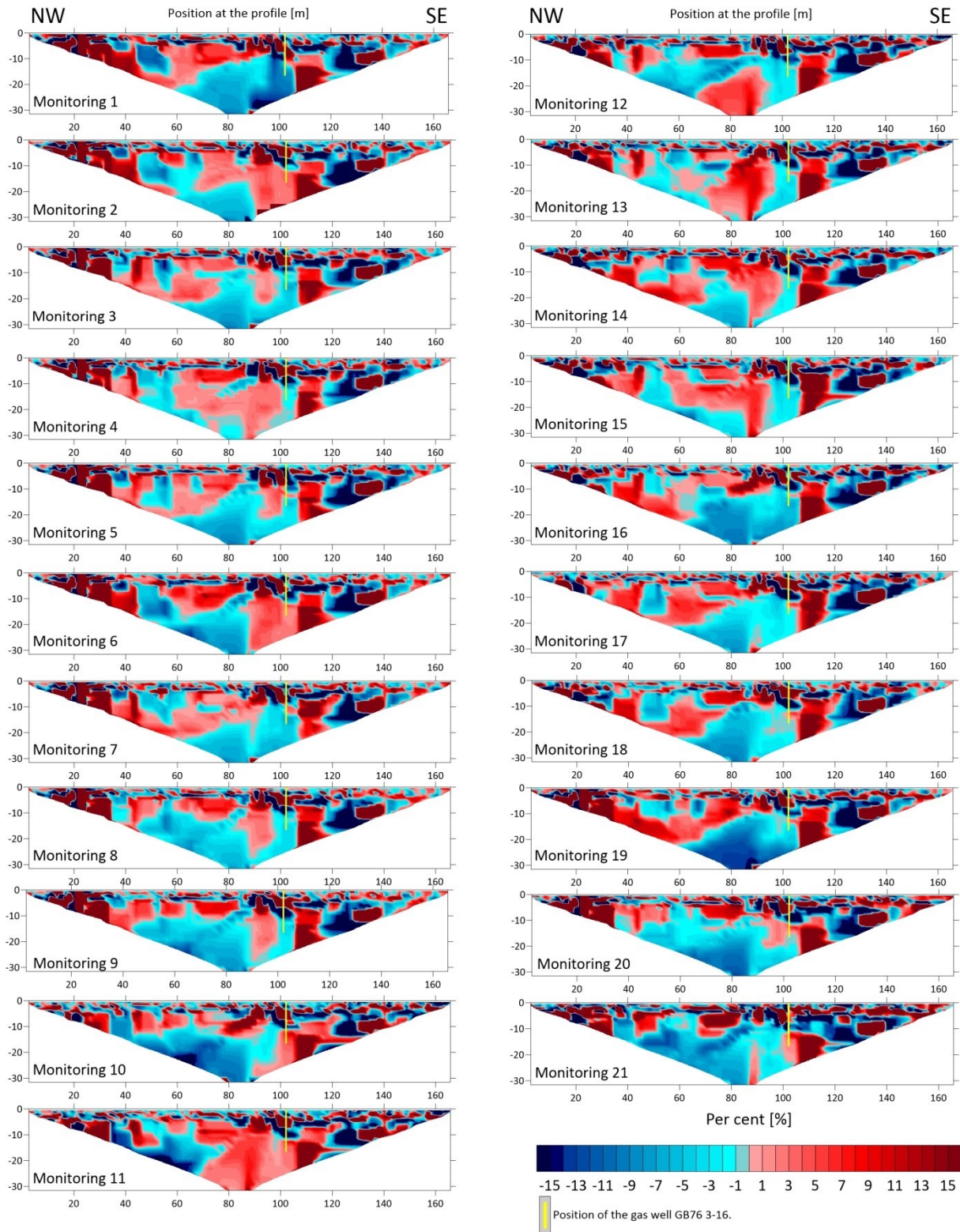


Fig. 51: Variation of the conductivity change in per cent along profile RW 7 for the monitoring inversion results. The changes are related to the original state before the start of irrigation.

Thus, in both previous figures the effect of the introduced water is not clearly visible, Fig. 52 displays the conductivity change in per cent of the measured raw data. For the first time the effect of the introduced water gets detectable, thus the highest negative changes are located at the bottom of the gas well (marked with a black line). Also, it is visible that with increasing time, the number of the negative conductivity changes is increasing. And compared with Fig. 51 Monitoring 21 indicates, as expected, the largest difference. At the same time, as the number of the negative conductivity changes is increasing a pants-leg structure at profile meter 130 is getting bigger and bigger up to Monitoring 18 and disappears at Monitoring 20. This is explainable by a leak in the fire hose, which had a direct influence on three electrodes. Although this presentation looks promising, one has to be careful, as the measurements have also many positive conductivity changes and are results before any inversion.

Field measurements

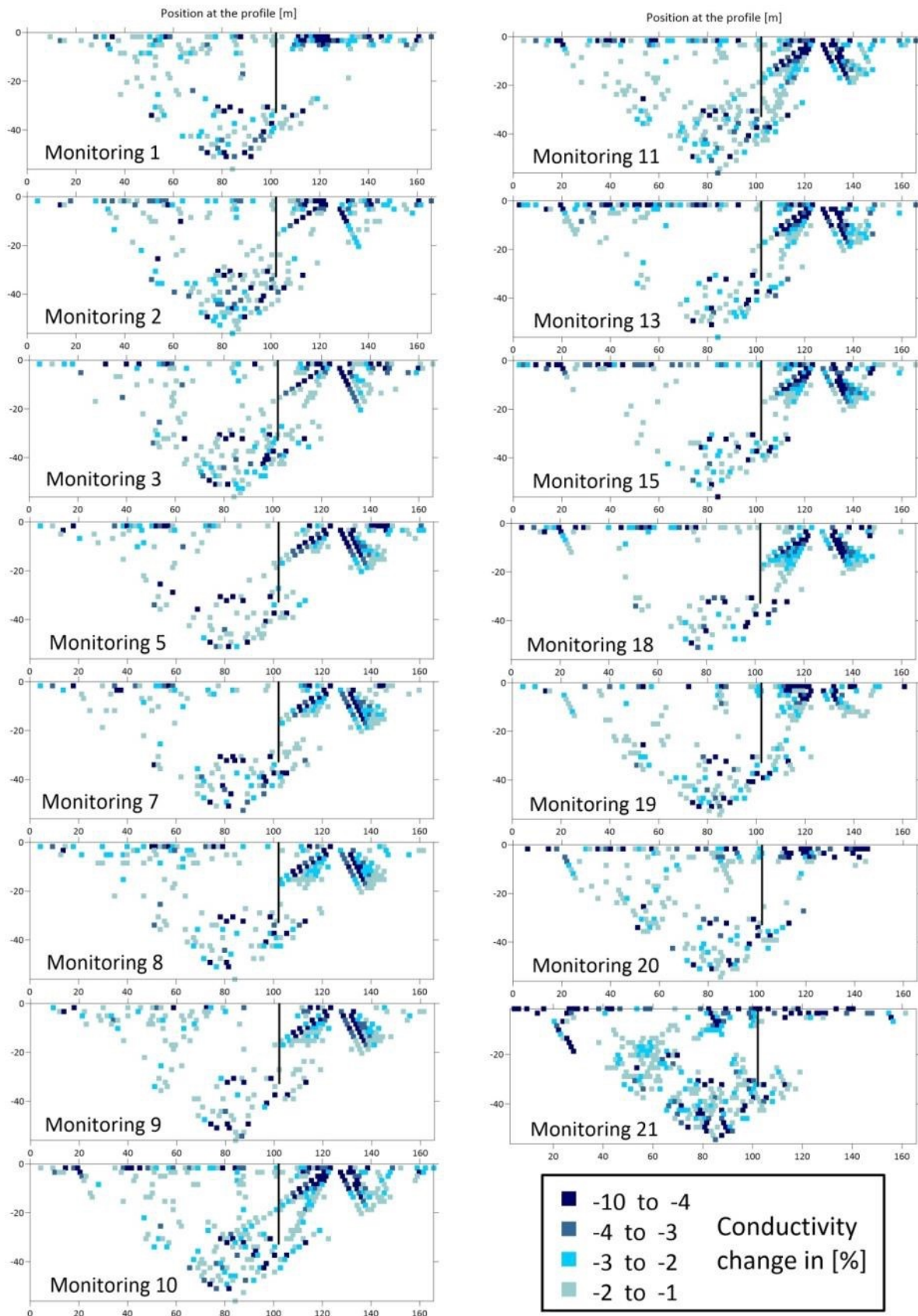


Fig. 52: Variation of the conductivity in per cent along profile RW 7 for the monitoring measured raw data. The changes are related to the original state before the start of irrigation.

Profile RW 1

For the monitoring the original profile RW 1 was a little bit adjusted, leading to a total length of 250 m with an electrode spacing of 2.50 m. This was done to obtain better monitoring results, since the gas wells are now located at the centre of the profile. At this profile water was introduced simultaneously at two gas wells: GB 101-A (profile meter 100) and GB 93-A (profile meter 175). The irrigation took place from 20/06/2018 starting at 14:05 until the 21/06/2018 ending at 10:40. In total 268 m³ of water were introduced at gas well GB 101-A and 110 m³ of water at gas well GB 93-A. In Tab. 10 the exact times for the measurements are depicted. Like for the monitoring survey of profile RW 7, the measurement Monitoring 0 indicates the original state of the subsurface and the following 5 measurement states during and after the irrigation. In contrast to profile RW 7 the last measurement of this profile was performed only 4 days after the end of irrigation.

Profile RW1	Day	Start Time	End Time
Monitoring 0	20.06.2018	12:02	13:43
Monitoring 1	20.06.2018	14:01	15:24
Monitoring 2	20.06.2018	16:01	17:25
Monitoring 3	21.06.2018	08:20	09:39
Monitoring 4	22.06.2018	11:35	12:52
Monitoring 5	25.06.2018	10:05	11:23

Tab. 10: Times for the time-lapse measurements with the start and end time for each measurement at profile RW 1.

The introduced water had a conductivity of 0.794 S/m at 25 °C, which is around 8 times higher than the conductivity of the water for profile RW 7. Hence, for this profile it was possible to identify the water flow paths. In Fig. 53 the time-lapse inversion results and in Fig. 54 the conductivity difference of the inversion results is displayed.

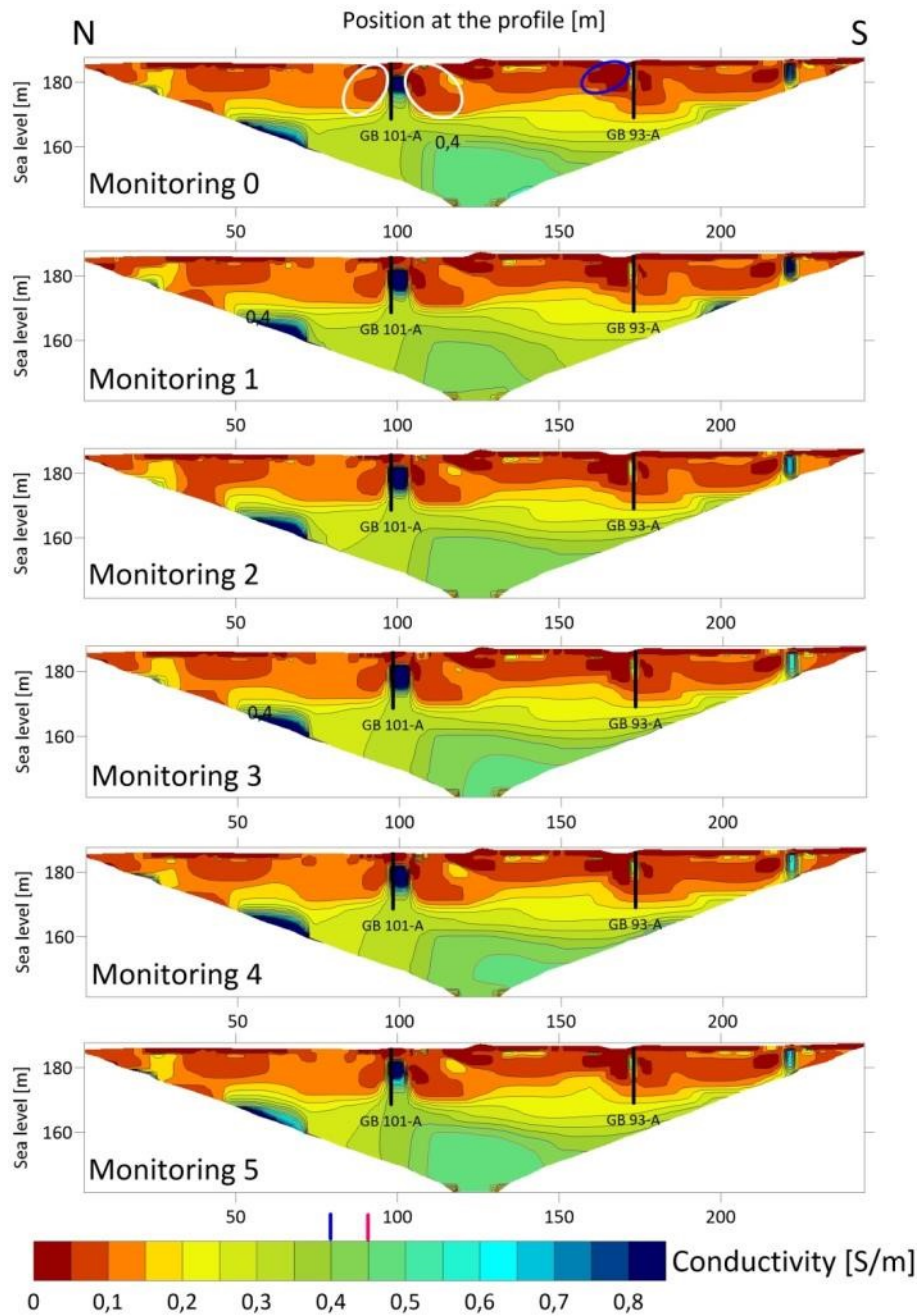


Fig. 53: Variation of the conductivity [S/m] along profile RW 1 for the monitoring measurements. The black lines indicate the positions of the gas wells, from where water was introduced. The blue and white circle indicates pants-leg structures.

The time-lapse inversion results indicate in Monitoring 0 to Monitoring 5 the same distinctive subsurface structures. Namely: two very good conductive zones and a non-conductive top layer with some interruptions. The first conductive zone appears in a quadratic form and is located next to the gas well GB 101-A. Additionally, to the left and right of this good conductive zone, a kind of a pants-leg structure, marked with a white circle is identifiable. A similar structure is marked with a blue circle at profile meter 175. At this profile position an around 1.5 m deep and 10 m wide depression is located. The second good

conductive zone is located at profile meter 60 in a depth of around 20 m. Below 20 m depth the subsurface displays medium conductivity values, which changes slightly from measurement to measurement as a result of irrigation.

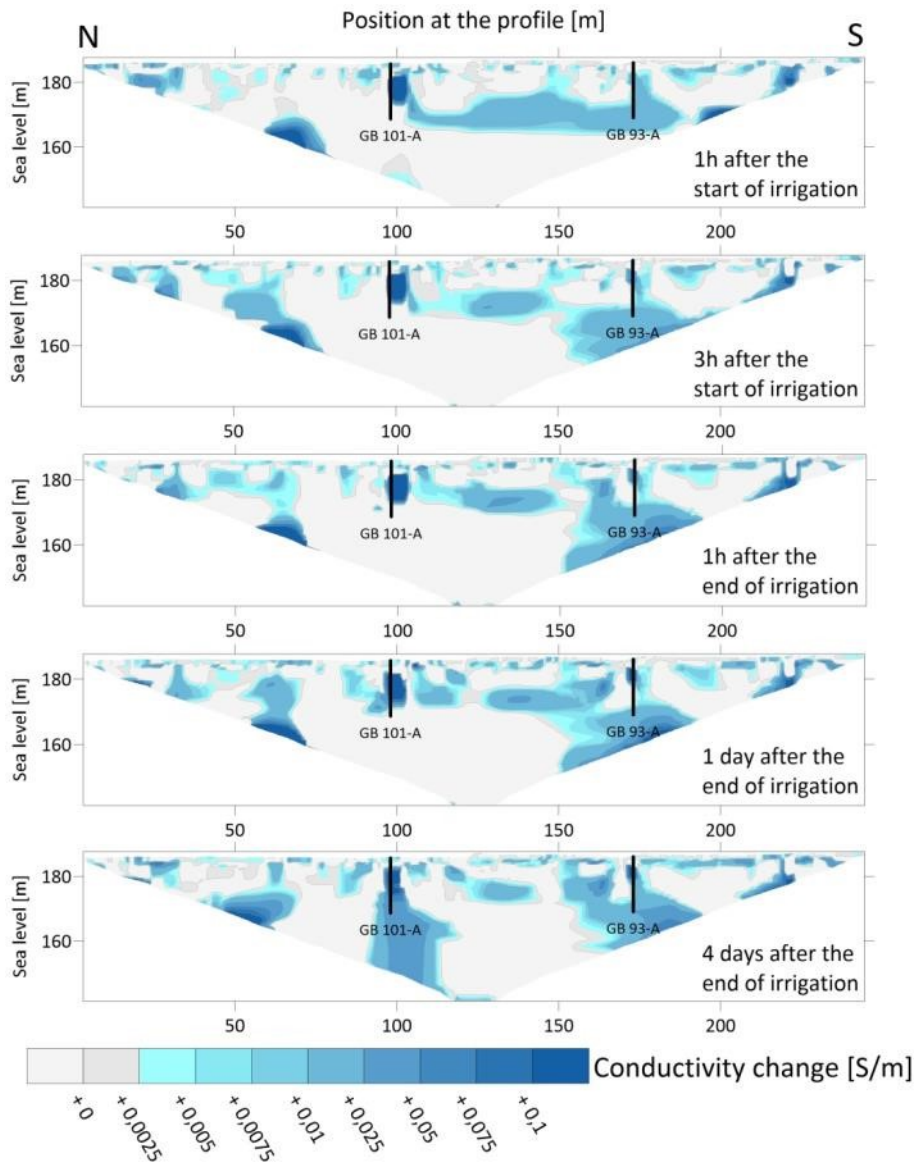


Fig. 54: Variation of the conductivity change along profile RW 1 for the monitoring inversion results. The changes are related to the original state before the start of irrigation. The black lines indicate the positions of the gas wells, from where water was introduced.

In Fig. 54 the conductivity changes are displayed. Since the conductivity difference of the introduced water (0.794 S/m) and the subsurface (around 0.3 S/m) is big enough, it was possible to identify the water flow paths, which are displayed in blue colours. One hour after the start of irrigation a water bridge between the two gas wells is recognizable which becomes smaller in the measurement three hours after the start of irrigation. One hour after

the end of irrigation the water bridge remained almost the same, but the water is now distributed more widely around gas well GB 93-A. The same is visible in the measurement one day after the end of irrigation. Four days after the end of irrigation, however, this water bridge almost disappeared and also the water zone around gas well GB 93-A got smaller. In contrast, around gas well GB 101-A a larger water zone has formed. In addition, there are other zones showing an increase in water content, but are located far away from the gas wells. These could be explained by the fact that the measured profile represents only a 2-D section of the subsurface, but the water spreads out 3 dimensionally and thus can leave the profile at the positions of the gas wells and could return elsewhere.

Profile RW 6

This profile was measured from 21/06/2018 until the 25/06/2018. In the first two days, from 21/06/2018 starting at 14:00 until the 22/06/2018 ending at 7:50 the irrigation took place at the gas wells GB 79 3-16 and GB 119 1-16 with a total amount of 464 m³ water per well. The exact times for each measurement are depicted in Tab. 11.

Profile RW6	Day	Start Time	End Time
Monitoring 0	21.06.2018	12:43	13:37
Monitoring 1	21.06.2018	14:00	14:53
Monitoring 2	21.06.2018	15:14	16:08
Monitoring 3	21.06.2018	16:23	17:17
Monitoring 4	22.06.2018	08:30	09:27
Monitoring 5	25.06.2018	12:38	13:34

Tab. 11: Times for the time-lapse measurements with the start and end time for each measurement at profile RW 6.

As the conductivities nearby the gas wells are maximum 0.3 S/m (Fig. 55) and the conductivity of the introduced water is 0.769 S/m at 25 °C, it was possible as for profile RW 1 to determine the water flow paths (Fig. 56).

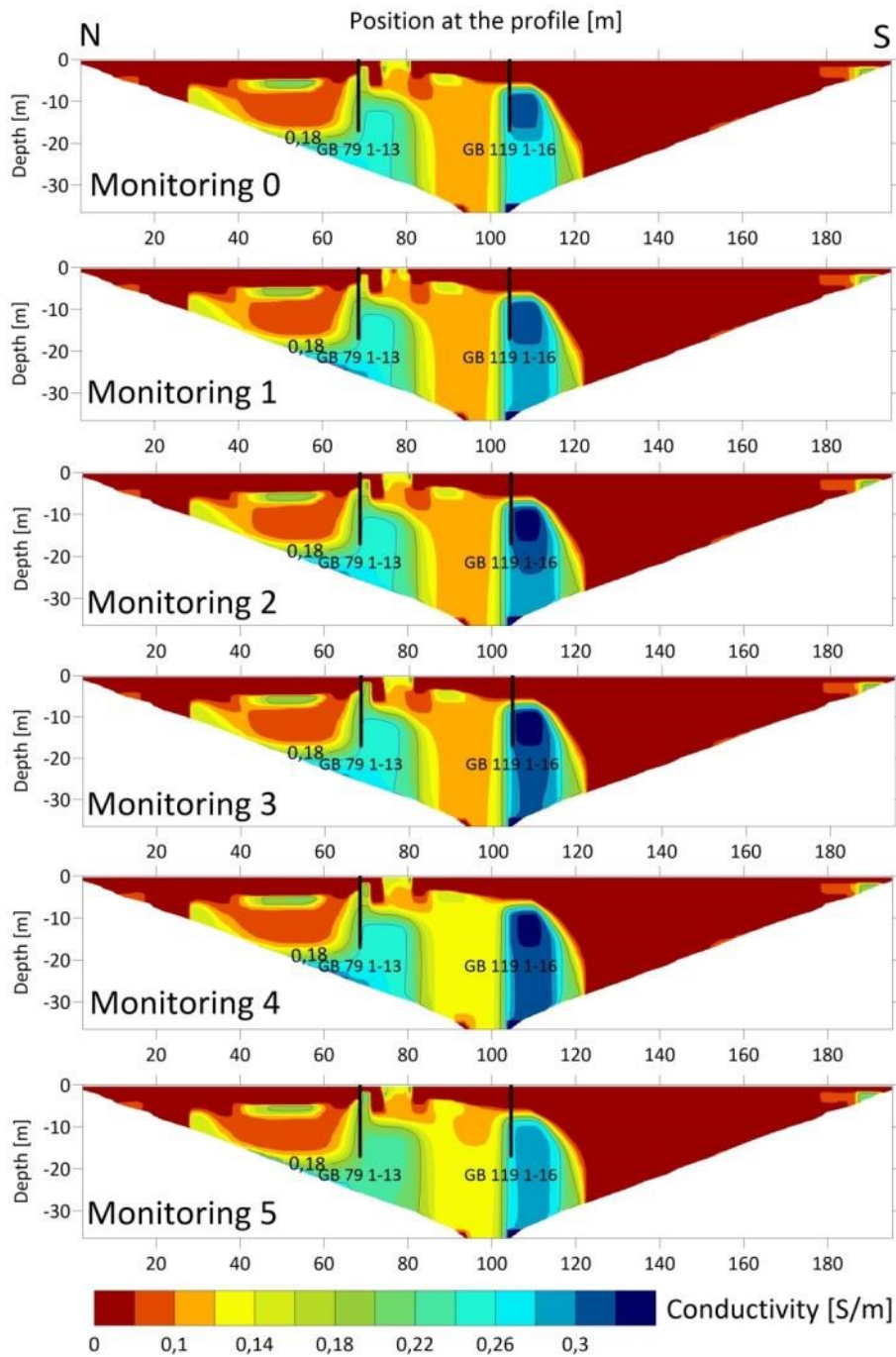


Fig. 55: Variation of the conductivity [S/m] along profile RW 6 for the monitoring measurements. The black lines indicate the positions of the gas wells, from where water was introduced.

In Fig. 55, Monitoring 0 indicates again the original state of the subsurface, before any irrigation. The gas well GB 119 1-16 displays like the gas well GB 101-A (Fig. 53) a conductive quadratic structure. Moreover, the profile indicates a very low conductive area south of the gas well GB 119 1-16 and a non-conductive top layer in the northern part. These structures are the same in all 6 measurements. Compared to profile RW 1 (Fig. 53) the conductivity change because of irrigation is better visible in this profile. Around gas well GB 119 1-16 the

conductivity increases each time step, since the conductivity of the introduced water is higher than that of the subsurface. This change is not so clearly recognizable around gas well GB 79 1-13, but in Fig. 56 it becomes detectable.

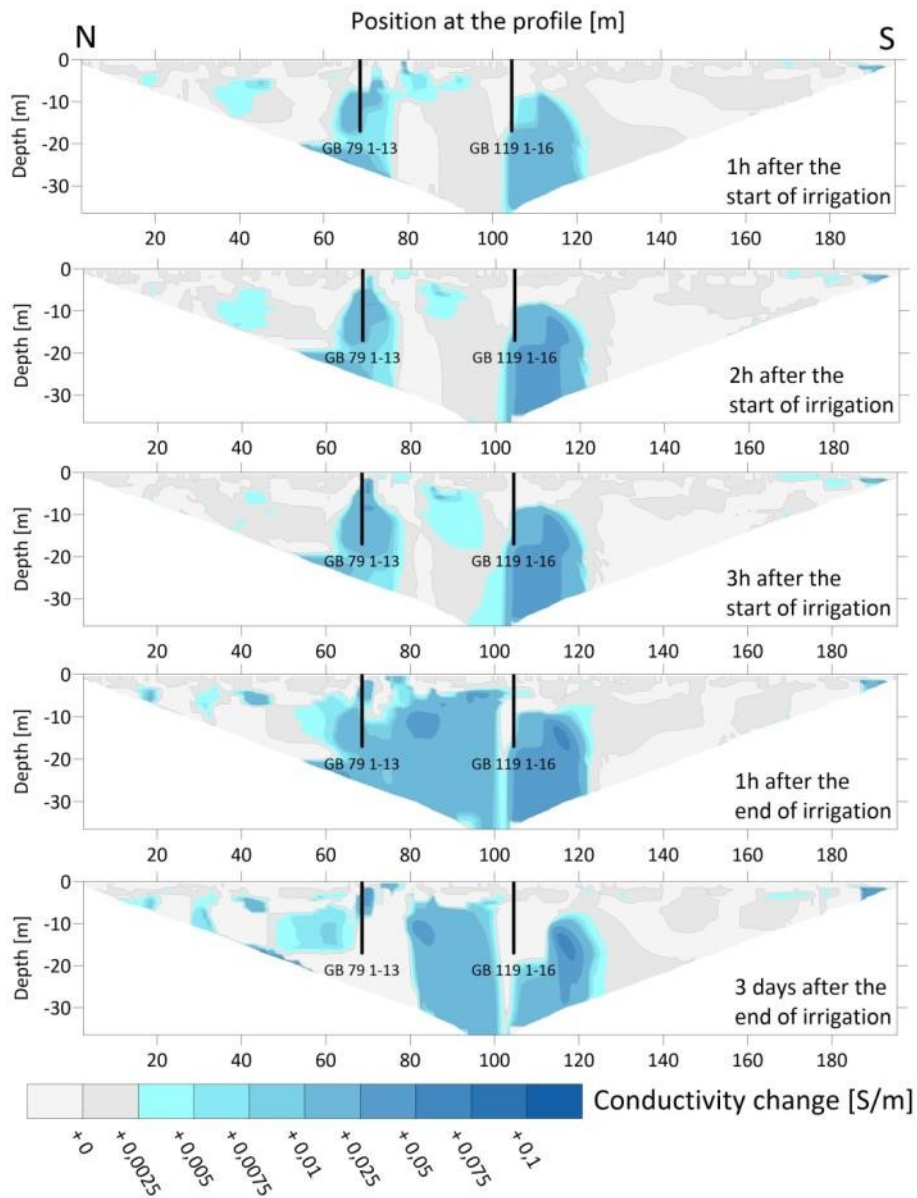


Fig. 56: Variation of the conductivity change along profile RW 6 for the monitoring inversion results. The changes are related to the original state before the start of irrigation. The black lines indicate the positions of the gas wells, from where water was introduced.

In Fig. 56 the absolute positive conductivity change due to irrigation is marked in blue colours. As expected the biggest changes are adjacent to the gas wells. Gas well GB 79 1-13 indicates in the first three hours after the start of irrigation a remarkable water increase in a droplet shape. At the time one hour after the end of irrigation, this droplet shape

disappeared and the whole area was filled up with water. This drastic difference between the two time steps is not surprising, as there were about 12 hours between the two measurements and thus the largest amount of water was pumped into the ground within this time. Around gas well GB 119 1-16, from the beginning on, a constant increase in water content is trackable up to the measurement one hour after the end of irrigation. At this measurement occurs a vertical aligned structure, separating the two water bodies which were introduced from the different gas wells. In the measurement three days after the end of irrigation, around both gas wells, the water body becomes smaller as expected.

3.3.7 Conclusions of the measurements at the Rautenweg landfill

In this section two measurement campaigns were described. The first one aimed at identification of wet and dry areas within the subsurface of the landfill and the second one to monitor the water flow paths of the introduced water via the gas wells. Both campaigns were successful with some limitations.

In the first one the water saturation is more a rough guess and not an exact determination, since no in-situ waste sample was accessible. Therefore, the computation after the Eq. (6) was not possible, which would lead to a more precise result. If it had been possible to measure the temperature within the landfill the result also would have been improved as it would no longer be necessary to specify a temperature range. And the last limitation is the conductivity of the leachate water. Here it was possible to obtain a sample from the fire pond and from a selected well (inner pipe 2), but the sampling point locations are several 100 m away from the profile lines. However, the samples are with great probability still representative, because the landfill has a closed water cycle and no water boundaries are installed inside the landfill. Therefore, the four plots (Fig. 45 to Fig. 48) of the profiles are a good basis to make statements about wet and dry areas, with potential for improvement of the water saturation determination.

In the second campaign the most obvious limitation is when the conductivity of the introduced water is nearly the same as of the subsurface. This can be clearly seen in Fig. 50 where the tracking of the water flow path was impossible. Whereas in Fig. 54 and Fig. 56 the monitoring was highly successful since the difference between the conductivities is big enough.

4 Results / Discussion

Selection of the proper array configuration

The experiments in Gams have shown that not every array configuration is well suited for the determination of wet and dry areas within the landfill and the monitoring of introduced water. The identification of the proper array configuration was done within a step by step process. First, Wenner, Schlumberger, Dipole-Dipole and Pole-Dipole measurements were performed at three parallel profiles and afterwards evaluated statistically. Overall, the statistical values of the measurement errors (dU in %) are good, except for the Pole-Dipole array. This array type shows higher maximum error values (up to 2490 %) for a homogenous subsurface compared with the other ones (up to a maximum value of 5.66 %).

As a second step, it was tried to determine the error source of the Pole-Dipole measurements. Therefore, Pole-Dipole measurements were performed with various software parameters and different locations of the remote electrode B (perpendicular to the profile or in line direction). Within this analysis, it can be demonstrated that the errors are randomly distributed and thus not bounded to a depth level, to a specific electrode number or to a defined electric current value. This leads to the assumption that the measurements cannot be improved to obtain fewer errors. Only the direction of the remote electrode B can be changed to perpendicular directions. However, the measurement errors are still very high with the remote electrode in perpendicular directions and therefore not suitable for the Rautenweg landfill survey campaign.

The third step was to compare the inversion results of the remaining three array types (Wenner, Schlumberger and Dipole-Dipole). This was done with selected depth slices, representing the resistivity change along the profile. While comparing these results some general trends are visible: (1) in the first depth slice all array types show nearly the same lateral variations in resistivity; (2) with increasing depth different results were obtained according to their sensitivity of horizontal resistivity changes in the subsurface; (3) in greater depths, these differences are getting smaller again. The results according to point (2) are in good compliance with the literature data (Loke, 2015), since the Wenner array configuration displays the smoothest result with less horizontal resistivity changes along the profile, followed by the Schlumberger and Dipole-Dipole array configuration. Therefore, these three

array configurations are applicable for the landfill survey, after the results from the test site Gams.

At the Rautenweg landfill these array configurations were used for the measurements from April 2018. There the Dipole-Dipole configuration failed completely, since it has a very low signal strength, which causes problems in noisy areas. The Wenner and Schlumberger array configuration show consistently good results, with the best results for the Wenner array. However, this is not surprising since it has the best signal to noise ratio of all array configurations. Thus, only the Wenner array type was used for the display of the inversion and monitoring results of the Rautenweg landfill.

Computation of the water saturation from the landfill body

For the determination of wet and dry areas within the Rautenweg landfill body 9 profiles were measured and analysed. During this analysis, some peculiarities and limitations became visible. The first one is the effect of gas wells on the measurements, if the distance between the well and the profile is only a few centimetres. Then, the iron pipe of the gas well acts as an electrical conductor and creates pants-leg structures in the apparent resistivity section and very conductive structures, at the locations of the wells in the profile, in the inversion results.

The inversion results are displayed in 2-D electrical conductivity profiles to determine the corresponding water content at four different temperature levels, since the conductivity is temperature dependent (Grellier et al., 2006; Hayley et al., 2007). Therefore, the temperature compensation of the leachate water samples (inner pipe 2 and fire pond) was done after the ÖNORM EN 27888. Each temperature level has its own conductivity scale, where the maximum value of the respective scale represents the conductivity value of the temperature compensated leachate water and indicates 100 % water saturation. The minimum value is 0.0 S/m and represents a water saturation of 0 %. Between the maximum and minimum water saturation the values were interpolated linearly. This approach indicates the next limitations. If it had been possible to measure the temperature inside the landfill, it would no longer be necessary to specify a temperature range. The proximate limitation is the conductivity of the leachate water, and the corresponding water content value of 100 %. Here it is not guaranteed that the conductivity of the leachate water within

the landfill has the same value, since the sampling point locations are several 100 m away from the profiles. However, the values are with great probability still representative, because the landfill has a closed water cycle. The last limitation is the exact determination of the water content, which was not feasible, since no in-situ waste samples, for the establishment of a water content conductivity relation, were available. Hence, the exact computation after Eq. (6) (Grellier et al., 2006) was not possible and the water saturation is more a rough guess. Nonetheless the conductivity plots are a good basis for statements about wet and dry areas inside the landfill, since the conductivity values of the leachate water and subsurface waste body is in good consent with the literature data (Bernstone et al., 2000; Georgaki et al., 2008; Hermozilha et al., 2010).

Water flow paths monitoring

To identify the proper settings and if any introduced water can be traced for the landfill survey, a model experiment was carried out at the test site Gams. In total 576 l water with a conductivity of 0.3 S/m were pumped, within 7 stages, into the subsurface. After each stage (introduction of approximately 72 l water for the first 6 stages and 144 l water for the last stage) a Wenner array measurement was performed to identify the water flow paths inside the subsurface. The measurements were evaluated with the time-lapse inversion settings of the software RES2DINVx64 with different parameters for the damping factor α (0.25 and 1.00). The results are displayed as resistivity changes in per cent referred to the original state measurement before any water introduction. There it can be clearly visible while using higher damping factors, smoother time-lapse plots are obtained, but they extinguish fine structures. Generally, this experiment demonstrated that a small amount of water can be successfully tracked inside the subsurface and even drainage corridors could be identified with a damping factor of 0.25. Therefore, the monitoring measurements at the landfill were performed with the same settings, since the model experiment in Gams was highly successful.

At the Rautenweg landfill three profiles (RW 1, RW 6 and RW 7) were monitored. All measurements at the landfill were successful with one limitation. If the conductivity difference between the introduced water and the subsurface is too small, it is not possible to

identify any water flow paths, which is the case at profile RW 7. There the measurements are highly accurate and reproducible (each single measurement indicates the same subsurface features). Thus, the non-traceability of the water must occur from the low conductivity difference between the introduced water (0.10 S/m) and the original subsurface (0.13 S/m).

The monitoring at the other two profiles (RW 1 and RW 6) were highly successful without any limitations, since the conductivity difference between the subsurface and the introduced water is around 8 times higher as for profile RW 7. At both profiles the biggest difference in conductivity compared to the original state occurs nearby the gas wells where water was introduced. Additionally, other areas showing an increase in water content, but are located far away from the gas wells. This fact is explained by the water flow paths inside the landfill. Since the profile represents only a 2-D section of the subsurface, but the water spreads out 3 dimensionally, the water can leave the profile and return elsewhere. This effect is clearly visible at profile RW 1 (Fig. 54). In addition, at this profile around gas well GB 93-A a small pants-leg structure is visible, caused by a small 1.5 m deep and 10 m wide depression. At profile RW 6, between time step 3h after the start of irrigation and 1h after the end of irrigation, around gas well GB 79 1-13 a huge increase in water content is identifiable (Fig. 56). This drastic difference can be explained by the time difference of about 12h or through an underground barrier that is broken during irrigation.

Overall the monitoring results of the profiles RW 1 and RW 6 are very good, since water flow paths are detectable and the biggest increase of water content is at the gas wells.

5 Summary / Outlook

The measurements at the test site Gams and at the Rautenweg landfill were successful with some limitations. In Gams, it was not possible to identify the error source for the Pole-Dipole measurements, but the determination of the proper measurement device settings and electrode array configuration worked well. The conclusion is, that for the measurements at the Rautenweg landfill the Wenner array, with default measurement instrument settings, except the maximum number of readings, is the preferred choice. Additionally, in Gams a water flow path monitoring experiment was conducted. The result of this experiment is, that the water monitoring at the landfill will work well and during time-lapse inversion of the measured data a damping factor α of 0.25 should be used.

At the Rautenweg landfill the greatest limitations are caused by the unknown subsurface temperature and leachate water conductivity and by the missing in-situ waste samples for the exact determination of the water saturation. Therefore, the water content estimation presented in this thesis is more a rough guess, but enough to make statements about the moisture content within the landfill. During the water flow path monitoring at the landfill the greatest limitation is when the conductivity difference between the subsurface and the introduced water is too small, leading to an impossibility of the water flow paths tracking. However, if the conductivity difference is sufficient the water monitoring indicates remarkable results. The spreading of the water in the subsurface could be traced very well and even the highest increase in water content was evident around the gas wells where the water was introduced.

Overall, this thesis presents notable results with the possibility for improvements. To obtain the best results while using the 4point light 10W device from Lippmann geophysical instruments, in future measurement campaigns at landfills the Wenner array configuration should be used. In addition, intensive efforts should be made to obtain further information about temperatures and leachate water conductivities within the subsurface. Finally, the presence of in-situ waste samples is necessary for the establishment of relationships between the measured electrical conductivity and water saturation.

6 References

- Ahmed, S.I., Johari, A., Hashim, H., Mat, R., Lim, J.S., Ngadi, N., Ali, A., 2014. Optimal landfill gas utilization for renewable energy production. *Environ. Prog. Sustain. Energy* 34, 289–296.
- Archie, G.E., 1942. The Electrical Resistivity Log as an Aid in Determining Some Reservoir Characteristics. *Trans. AIME* 146, 54–62.
- Bernstone, C., Dahlin, T., Ohlsson, T., Hogland, H., 2000. DC-resistivity mapping of internal landfill structures: two pre-excavation surveys. *Environ. Geol.* 39, 360–371.
- Binley, A., Kemna, A., 2005. DC Resistivity and Induced Polarization Methods, in: *Hydrogeophysics*.
- Blaschek, R., Hördt, A., Kemna, A., 2008. A new sensitivity-controlled focusing regularization scheme for the inversion of induced polarization data based on the minimum gradient support. *Geophysics* 73, F45–F54.
- Chelidze, T.L., Guéguen, Y., 1999. Electrical spectroscopy of porous rocks: a review-I. Theoretical models. *Geophys J Int* 137, 1–15.
- Chen, Y., Or, D., 2006. Geometrical factors and interfacial processes affecting complex dielectric permittivity of partially saturated porous media. *Water Resour. Res.* 42, 1–9.
- De Lima, O., Sharma, M., 1992. A generalized Maxwell-Wagner theory for membrane polarization in shaly sands. *Geophysics* 57, 431–440.
- deGroot-Hedlin, C., Constable, S., 1990. Occam's inversion to generate smooth, two-dimensional models from magnetotelluric data. *Geophysics* 55, 1613–1624.
- Dentith, M., Mudge, S., 2014. *Geophysics for the mineral exploration geoscientist*, Cambridge: Cambridge University Press.
- Dey, A., Morrison, H., 1979a. Resistivity modelling for arbitrary shaped two-dimensional structures. *Geophys. Prospect.* 27, 106–136.
- Dey, A., Morrison, H.F., 1979b. Resistivity modeling for arbitrarily shaped three-dimensional structures. *Geophysics* 44, 753–780.
- Frid, V., Doudkinski, D., Liskevich, G., Shafran, E., Averbakh, A., Korostishevsky, N., Prihodko, L., 2010. Geophysical-geochemical investigation of fire-prone landfills. *Environ. Earth*

- Sci. 60, 787–798.
- Georgaki, I., Soupios, P., Sakkas, N., Ververidis, F., Trantas, E., Vallianatos, F., Manios, T., 2008. Evaluating the use of electrical resistivity imaging technique for improving CH₄ and CO₂ emission rate estimations in landfills. *Sci. Total Environ.* 389, 522–531.
- Ghorbani, A., Cosenza, P., Ruy, S., Doussan, C., Florsch, N., 2008. Non-invasive monitoring of water infiltration in a silty clay loam soil using Spectral Induced Polarization. *Water Resour. Res.* 44, 1–18.
- Grellier, S., Robain, H., Bellier, G., Skhiri, N., 2006. Influence of temperature on the electrical conductivity of leachate from municipal solid waste. *J. Hazard. Mater.* 137, 612–617.
- Günther, T., n.d. www.resistivity.net [WWW Document]. 2007. URL <http://www.resistivity.net>
- Hayley, K., Bentley, L.R., Gharibi, M., Nightingale, M., 2007. Low temperature dependence of electrical resistivity: Implications for near surface geophysical monitoring. *Geophys. Res. Lett.* 34, 1–5.
- Hayley, K., Pidlisecky, A., Bentley, L.R., 2011. Simultaneous time-lapse electrical resistivity inversion. *J. Appl. Geophys.* 75, 401–411.
- Hermozilha, H., Grangeia, C., Matias, M.S., 2010. An integrated 3D constant offset GPR and resistivity survey on a sealed landfill - Ilhavo, NW Portugal. *J. Appl. Geophys.* 70, 58–71.
- Kemna, A., Binley, A., Kemna, A., Binley, A., Cassiani, G., Niederleithinger, E., Revil, A., Slater, L., Williams, K.H., Orozco, A.F., Haegel, F., Hördt, A., Kruschwitz, S., Leroux, V., 2012. An overview of the spectral induced polarization method for near-surface applications An overview of the spectral induced polarization method for near-surface applications. *Near Surf. Geophys.* 10, 453–468.
- Kim, J., Yi, M., Park, S., Gon, J., 2009. 4-D inversion of DC resistivity monitoring data acquired over a dynamically changing earth model. *J. Appl. Geophys.* 68, 522–532.
- Kumar, S., Mondal, A.N., Gaikwad, S.A., Devotta, S., Singh, R.N., 2004. Qualitative assessment of methane emission inventory from municipal solid waste disposal sites: A case study. *Atmos. Environ.* 38, 4921–4929.
- Leroy, P., Revil, A., Kemna, A., Cosenza, P., Ghorbani, A., 2008. Complex conductivity of water-saturated packs of glass beads. *J. Colloid Interface Sci.* 321, 103–117.

- Lippmann, E., 2014. 4point light 10W Earth resistivity meter Operating instructions. Lippmann Geophys. Messgeräte.
- Loke, M.H., 2017. RES2DINVx64 ver. 4.07 with multi-core and 64-bit support. Geotomo Softw. Malaysia.
- Loke, M.H., 2015. Tutorial: 2-D and 3-D electrical imaging surveys. Geotomo Softw. Malaysia.
- Loke, M.H., Chambers, J.E., Rucker, D.F., Kuras, O., Wilkinson, P.B., 2013. Recent developments in the direct-current geoelectrical imaging method. *J. Appl. Geophys.* 95, 135–156.
- Lorber, K.E., 2010. Deponiegasverwertung DEPONIE RAUTENWEG - Auswertungszeitraum 2013 – 2017 mit Prognose 2030 und Variantenvergleich. GUTACHTEN im Auftrag der MA 48.
- MA48, 2013. Waste to Energy – Treatment of Residual Waste.
- Majdinasab, A., Zhang, Z., Yuan, Q., 2017. Modelling of landfill gas generation: a review. *Rev. Environ. Sci. Biotechnol.* 16, 361–380.
- Marshall, D.J., Madden, T.R., 1959. Induced polarization, a study of its causes. *Geophysics* XXIV, 790–816.
- Merriam, J.B., 2007. Induced polarization and surface electrochemistry. *Geophysics* 72, F157–F166.
- Porsani, J.L., Filho, W.M., Elis, V.R., Shimeles, F., Dourado, J.C., Moura, H.P., 2004. The use of GPR and VES in delineating a contamination plume in a landfill site: A case study in SE Brazil. *J. Appl. Geophys.* 55, 199–209.
- Rettenberger, G., 1992. Der Deponiegashaushalt in Altablagerungen - Leitfaden Deponiegas. Landesanstalt für Umweltschutz Baden-Württemberg, Karlsruhe.
- Revil, A., Karaoulis, M., Johnson, T., Kemna, A., 2012. Review: Some low-frequency electrical methods for subsurface characterization and monitoring in hydrogeology. *Hydrogeol. J.* 20, 617–658.
- Rucker, D.F., Fink, J.B., Loke, M.H., 2011. Environmental monitoring of leaks using time-lapsed long electrode electrical resistivity. *J. Appl. Geophys.* 74, 242–254.
- Silvester, P.P., Ferrari, R.L., 1996. *Finite Elements for Electrical Engineers*, 3rd ed. Cambridge University Press, Cambridge.

- Soupios, P., Papadopoulos, I., Kouli, M., Georgaki, I., Vallianatos, F., Kokinou, E., 2007. Investigation of waste disposal areas using electrical methods: A case study from Chania, Crete, Greece. *Environ. Geol.* 51, 1249–1261.
- Themelis, N.J., Ulloa, P.A., 2007. Methane generation in landfills. *Renew. Energy* 32, 1243–1257.
- Tildy, P., Neduczka, B., Nagy, P., Kanli, A.I., Hegymegi, C., 2017. Time lapse 3D geoelectric measurements for monitoring of in-situ remediation. *J. Appl. Geophys.* 136, 99–113.
- Tintner, J., Kühleitner, M., Binner, E., Brunner, N., Smidt, E., 2012. Modeling the final phase of landfill gas generation from long-term observations. *Biodegradation* 23, 407–414.
- Titov, K., Komarov, V., Tarasov, V., Levitski, A., 2002. Theoretical and experimental study of time domain-induced polarization in water-saturated sands. *J. Appl. Geophys.* 50, 417–433.
- Vaudelet, P., Revil, A., Schmutz, M., Franceschi, M., Bégassat, P., 2011. Induced polarization signatures of cations exhibiting differential sorption behaviors in saturated sands. *Water Resour. Res.* 47, 1–21.
- Vinegar, H.J., Waxman, M.H., 1984. Induced polarization of shaly sands. *Geophysics* 49, 1267–1287.
- Walach, G., 1990. Deponieflächenerkundung mit geophysikalischen Methoden. *Österreichische Ingenieur- und Archit.* 135, 210–219.
- Yesiller, N., Hanson, J.L., 2003. Analysis of Temperatures at a Municipal Solid Waste Landfill. *Proc. Ninth Int. Waste Manag. Landfill Symp. Sardinia* 1–10.
- ÖNORM EN 27888: 1993 12 01 (Wasserbeschaffenheit – Bestimmung der elektrischen Leitfähigkeit (ISO 7888: 1985)).
- ÖNORM S 2084: 2012 04 15 (Anforderungen an Entgasungsmaßnahmen für Deponien und Altablagerungen)
- Implenia Baugesellschaft m. b. H., 2016. Errichtung von Gasbrunnen, Feuerlöschbrunnen und Inklinometern 2016 – Deponie Rautenweg, 1220 Wien.
- <http://atlas.noe.gv.at> (December 2017)

http://app.hydrographie.steiermark.at/bilder/Hochwasserzentrale/Source/SteiermarkOverview_Pub.htm (18/03/2018)

7 List of Figures

Fig. 1: Four electrode-measurement arrangement: Two current electrodes (A and B) and two potential electrodes (M and N) (modified after Revil et al., 2012).....	5
Fig. 2: The commonly used electrode arrays and plotting conventions for soundings and pseudosections: (a) pole–pole, (b) pole–dipole, (c) dipole–dipole, (d) Wenner, (e) Schlumberger and gradient arrays (Dentith and Mudge, 2014).....	8
Fig. 3: Example for an electrical resistivity tomography measurement. (a) real model, (b) pseudosection with apparent resistivity and (c) the inverted section. The triangles indicate the positions of the electrodes (Revil et al., 2012).	9
Fig. 4: Explanation of the pants-legs response using a dipole-dipole array (Dentith and Mudge, 2014).	10
Fig. 5: Resistivity ranges of typical waste materials and leachate waters from various publications (Bernstone et al., 2000; Georgaki et al., 2008; Hermozilha et al., 2010; Porsani et al., 2004; Soupios et al., 2007; Walach, 1990).	11
Fig. 6: Vertical electrical sounding curve for a constant thickness and variable resistivity of the upper layer (Dentith and Mudge, 2014).	13
Fig. 7: (a) Time-domain measurement with small rise and decay of the secondary voltage produced by polarization effects. (b) Frequency-domain measurement with the sine wave signal and the phase shifted obtained potential (Modified after Dentith and Mudge (2014)).	14
Fig. 8: Capacitive properties during charging and discharging of electrical charges. (a) Membrane polarization and (b) grain polarization (Modified after Dentith and Mudge (2014)).	15
Fig. 9: (a) 4point light 10W instrument (right side) with the remote controlling unit and power supply (left side). (b) Active switch box for multi electrodes surveys.	17

Fig. 10: (a) Base station with receiver and radio link. (b) Moving rover during measurements. 17

Fig. 11: Location of the profiles in Gams. (Abbreviations: P1 = profile 1 – P3 = profile 3). 20

Fig. 12: Rainfall statistics from 15/03/2018 12:00 o'clock until the 18/03/2018 08:00 o'clock. Before and after this period of time there was no rainfall (Modified after: Hydrographie Steiermark (18/03/2018)). 21

Fig. 13: Quality check of the calibration procedure at profile 1. (a) Modelled resistivity section before the calibration. (b) Modelled resistivity section after the calibration. (c) Resistivity change in percent obtained through the calibration procedure in the modelled sections. 22

Fig. 14: Comparison of measured resistivity values before (horizontal axis) and after (vertical axis) calibration. The nearly 45° line indicates no significant changes during calibration. 23

Fig. 15: Box-Whisker plot of the measurement error dU (in %) for profiles 1 to 3. The median is displayed for all measurements. The upper Whisker is located at IQR*1.5. (Abbreviations: IQR = interquartile rang; Q1 = lower quartile; Q3 = upper quartile; P1 = profile 1 to P3 = profile 3; WE = Wenner array; PDP = Pole-dipole array; PDP_In = pole-dipole array with remote electrode in-line direction; PDP_P = pole-dipole array with remote electrode perpendicular to the profile direction; _PL and _PHQ = see text above; SCHL = Schlumberger array and DPDP = dipole-dipole array). 26

Fig. 16: Box-Whisker plot of the measurement error dU [%] for profiles 1 to 3 for the pole-dipole array. The median is displayed for all 8 measurements. The upper Whisker is located at IQR*1.5. Perpendicular direction of the remote electrode show generally less errors compared to the in-line direction. (Abbreviations: IQR = interquartile range; Q1 = lower quartile; Q3 = upper quartile; HQ = high quality; PDP = pole-dipole array; _In = remote electrode in-line direction; _P = remote electrode perpendicular to profile direction; _PL and _PHQ = different settings which are explained in the previous text). 28

Fig. 17: The horizontal axis shows the measurement number and the vertical axis dU in % for profile 3 - P3_PDP_P. With increasing number of the measurements also the depth of the measurements increases. 29

Fig. 18: The horizontal axis shows the measurement number and the vertical axis dU in % for profile 3 - P3_PDP_PL. With increasing number of the measurements also the depth of the measurements increases. 30

Fig. 19: The horizontal axis shows the measurement number and the vertical axis dU in % for profile 3 - P3_PDP_PHQ. With increasing number of the measurements also the depth of the measurements increases. 30

Fig. 20: The horizontal axis shows the electrode number and the vertical axis dU in % for profile 3 - P3_PDP_P. The red circle marks one measurement with an error around 100 %. 31

Fig. 21: The horizontal axis shows the electrode number and the vertical axis dU in % for profile 3 - P3_PDP_PL. 31

Fig. 22: The horizontal axis shows the electrode number and the vertical axis dU in % for profile 3 – P3_PDP_PHQ. 32

Fig. 23: The horizontal axis shows the electric current in mA and the vertical axis dU in % for profile 3 - P3_PDP_P. 33

Fig. 24: The horizontal axis shows the electric current in mA and the vertical axis dU in % for profile 3 - P3_PDP_PL. 33

Fig. 25: The horizontal axis shows the electric current in mA and the vertical axis dU in % for profile 3 - P3_PDP_PHQ. 34

Fig. 26: Resistivity changes along the profile 1 at a depth level between (a) 0.0 m and 0.55 m, (b) 1.10 m and 1.65 m, (c) 2.20 m and 2.75 m, (d) 3.30 m and 3.85 m, (e) 4.95 m and 5.50 m. The horizontal axis indicates the 100 layers in x-direction and the vertical axis the resistivity values obtained with the SIRT inversion. 37

Fig. 27: (a) 1.0m deep well with garden hose at profile meter 15 for water introduction. (b) Containers for the provision of conductive (0.3 S/m) water. 39

Fig. 28: Results of the time-lapse inversion with a damping factor of 0.25. At time 0 the upper high resistivity zone (marked with a blue circle) lies at profile meter 15. Because of irrigation this becomes smaller and migrates leftwards. The grey line indicates the position and depth of the test well. 40

Fig. 29: Variation of the resistivity change in per cent for the monitoring inversion results. The changes are related to the basic measurement at time 0. Blue colours indicate negative values (water saturation). Water saturation especially at the well position (red line). Damping factor $\alpha = 0.25$ 41

Fig. 30: Variation of the resistivity change in per cent for the monitoring inversion results. The changes are related to the basic measurement at time 0. Blue colours indicate negative values (water saturation). Water saturation especially at the well position (red line). Damping factor $\alpha = 1.00$ 43

Fig. 31: Model of the Rautenweg landfill (Lorber, 2010). 45

Fig. 32: Schematic representation of the Vienna sealed-wall chamber system at the Rautenweg landfill (MA48, 2013). 46

Fig. 33: Gas well GB76 3-16, which exemplifies the design of the gas wells. (Modified after: Implenia Baugesellschaft m.b.H., 2016)..... 47

Fig. 34: Pinzgauer goats at the Rautenweg landfill. The right picture demonstrates how curious these animals are. 48

Fig. 35: Position of the nine profiles at the Rautenweg landfill. Additionally the locations of the gas wells are marked with black rectangles. (Base map: Digitaler Atlas GIS Niederösterreich (December 2017)). 49

Fig. 36: (a) Electrode skewers which had to be drilled into the concrete top layer at profile RW 8. Two gas wells are visible in the background. (b) Watering of the electrode skewers to obtain better contact resistances. 50

Fig. 37: Box-Whisker plot of the measurement error dU (%) for profiles RW1-RW9. The median is displayed in all nine profiles. Values over $Q3 + IQR \cdot 1.5$ are defined as outliers. (Abbreviations: Q1 = lower quartile; Q3 = upper quartile; IQR = interquartile range; WE = Wenner array). 51

Fig. 38: Apparent resistivity section of profile RW 4 with pants-leg structures caused by the insufficient distance between the profile and the gas wells. 52

Fig. 39: Apparent resistivity section of profile RW 5. Since the distance is big enough between the profile and the gas wells, no pants-leg structure occurs..... 52

Fig. 40: (a) measured apparent resistivity pseudosection, (b) calculated apparent resistivity pseudosection and (c) inverse model resistivity section of profile RW 4 with used RW4_WE inversion parameters. 54

Fig. 41: (a) measured apparent resistivity pseudosection, (b) calculated apparent resistivity pseudosection and (c) inverse model resistivity section of profile RW 4 with used RW4_WE_1 inversion parameters. 54

Fig. 42: IP inversion results for profile RW 4. (a) Measured phase angle, (b) calculated phase angle and (c) inverse model phase angle section. 56

Fig. 43: (a) Leachate water sample collection at the inner pipe 2. (b) Experimental setup for the determination of the relationship between temperature and conductivity..... 57

Fig. 44: Conductivity vs. temperature for the mean value of the two leachate water samples calculated after ÖNORM EN 27888. The temperature coefficient was set to 0.022..... 58

Fig. 45: Variation of the conductivity [S/m] along profile RW 1 with conductivity scaling at (a) 20 °C, (b) 30 °C, (c) 40 °C and (d) 55 ° C. The maximum value of the conductivity corresponds to 100% water saturation and a conductivity of 0 S/m equates to a water content of 0%. The black squares mark the position of the gas wells where the depths represent the mean depth of the steel filter pipe. 60

Fig. 46: Variation of the conductivity [S/m] along profile RW 4 with conductivity scaling at (a) 20 °C, (b) 30 °C, (c) 40 °C and (d) 55 ° C. The maximum value of the conductivity corresponds to 100% water saturation and a conductivity of 0 S/m equates to a water content of 0%. The black squares mark the position of the gas wells where the depths represent the mean depth of the steel filter pipe. 63

Fig. 47: Variation of the conductivity [S/m] along profile RW 6 with conductivity scaling at (a) 20 °C, (b) 30 °C, (c) 40 °C and (d) 55 ° C. The maximum value of the conductivity corresponds to 100% water saturation and a conductivity of 0 S/m equates to a water

content of 0%. The black squares mark the position of the gas wells where the depths represent the mean depth of the steel filter pipe. 64

Fig. 48: Variation of the conductivity [S/m] along profile RW 7 with conductivity scaling at (a) 20 °C, (b) 30 °C, (c) 40 °C and (d) 55 ° C. The maximum value of the conductivity corresponds to 100% water saturation and a conductivity of 0 S/m equates to a water content of 0%. The black squares mark the position of the gas wells where the depths represent the mean depth of the steel filter pipe. 65

Fig. 49: (a) Gas well GB76 3-16 with the fire hose and water counter for the introduction of water from the inner well 4. (b) Conductivity meter “Cond 3110” for temperature and conductivity control of the introduced water. 67

Fig. 50: Variation of the conductivity [S/m] along profile RW 7 for the monitoring measurements with a conductivity scale for 55 ° C. The maximum value of the conductivity corresponds to 100% water saturation and a conductivity of 0 S/m equates to a water content of 0%. 68

Fig. 51: Variation of the conductivity change in per cent along profile RW 7 for the monitoring inversion results. The changes are related to the original state before the start of irrigation. 70

Fig. 52: Variation of the conductivity in per cent along profile RW 7 for the monitoring measured raw data. The changes are related to the original state before the start of irrigation. 72

Fig. 53: Variation of the conductivity [S/m] along profile RW 1 for the monitoring measurements. The black lines indicate the positions of the gas wells, from where water was introduced. The blue and white circle indicates pants-leg structures. 74

Fig. 54: Variation of the conductivity change along profile RW 1 for the monitoring inversion results. The changes are related to the original state before the start of irrigation. The black lines indicate the positions of the gas wells, form where water was introduced.. 75

Fig. 55: Variation of the conductivity [S/m] along profile RW 6 for the monitoring measurements. The black lines indicate the positions of the gas wells, from where water was introduced. 77

Fig. 56: Variation of the conductivity change along profile RW 6 for the monitoring inversion results. The changes are related to the original state before the start of irrigation. The black lines indicate the positions of the gas wells, from where water was introduced.. 78

Fig. 57: (a) measured apparent resistivity pseudosection, (b) calculated apparent resistivity pseudosection and (c) inverse model resistivity section of profile RW 1..... 100

Fig. 58: (a) measured apparent resistivity pseudosection, (b) calculated apparent resistivity pseudosection and (c) inverse model resistivity section of profile RW 2..... 101

Fig. 59: (a) measured apparent resistivity pseudosection, (b) calculated apparent resistivity pseudosection and (c) inverse model resistivity section of profile RW 3..... 101

Fig. 60: (a) measured apparent resistivity pseudosection, (b) calculated apparent resistivity pseudosection and (c) inverse model resistivity section of profile RW 5..... 102

Fig. 61: (a) measured apparent resistivity pseudosection, (b) calculated apparent resistivity pseudosection and (c) inverse model resistivity section of profile RW 6..... 102

Fig. 62: (a) measured apparent resistivity pseudosection, (b) calculated apparent resistivity pseudosection and (c) inverse model resistivity section of profile RW 7..... 103

Fig. 63: (a) measured apparent resistivity pseudosection, (b) calculated apparent resistivity pseudosection and (c) inverse model resistivity section of profile RW 8..... 103

Fig. 64: (a) measured apparent resistivity pseudosection, (b) calculated apparent resistivity pseudosection and (c) inverse model resistivity section of profile RW 9..... 104

Fig. 65: Variation of the conductivity [S/m] along the profile RW 2 with conductivity scaling at (a) 20 °C, (b) 30 °C, (c) 40 °C and (d) 55 ° C. The maximum value of the conductivity corresponds to 100% water saturation and a conductivity of 0 S/m equates to a water content of 0%. The black squares mark the position of the gas wells where the depths represent the mean depth of the steel filter pipe. 105

Fig. 66: Variation of the conductivity [S/m] along the profile RW 3 with conductivity scaling at (a) 20 °C, (b) 30 °C, (c) 40 °C and (d) 55 ° C. The maximum value of the conductivity corresponds to 100% water saturation and a conductivity of 0 S/m equates to a water content of 0%. The black squares mark the position of the gas wells where the depths represent the mean depth of the steel filter pipe. 106

Fig. 67: Variation of the conductivity [S/m] along the profile RW 5 with conductivity scaling at (a) 20 °C, (b) 30 °C, (c) 40 °C and (d) 55 ° C. The maximum value of the conductivity corresponds to 100% water saturation and a conductivity of 0 S/m equates to a water content of 0%. The black squares mark the position of the gas wells where the depths represent the mean depth of the steel filter pipe. 107

Fig. 68: Variation of the conductivity [S/m] along the profile RW 8 with conductivity scaling at (a) 20 °C, (b) 30 °C, (c) 40 °C and (d) 55 ° C. The maximum value of the conductivity corresponds to 100% water saturation and a conductivity of 0 S/m equates to a water content of 0%. The black squares mark the position of the gas wells where the depths represent the mean depth of the steel filter pipe. 108

Fig. 69: Variation of the conductivity [S/m] along the profile RW 9 with conductivity scaling at (a) 20 °C, (b) 30 °C, (c) 40 °C and (d) 55 ° C. The maximum value of the conductivity corresponds to 100% water saturation and a conductivity of 0 S/m equates to a water content of 0%. The black squares mark the position of the gas wells where the depths represent the mean depth of the steel filter pipe. 109

8 List of Tables

Tab. 1: Geometric factors for different electrodes arrays (Dentith & Mudge, 2014). 6

Tab. 2: Statistical evaluation for the resistivity values of profile 1 to 3. (Abbreviations: P1 = profile 1 to P3 = profile 3; WE = Wenner array; PDP = Pole-dipole array; PDP_In = pole-dipole array with remote electrode in-line direction; PDP_P = pole-dipole array with remote electrode perpendicular to the profile direction; _PL and _PHQ = see text above; SCHL = Schlumberger array and DPDP = dipole-dipole array). 24

Tab. 3: Statistical evaluation for the measurements errors dU (in %) values of profile 1 to 3. (Abbreviations: P1 = profile 1 to P3 = profile 3; WE = Wenner array; PDP = Pole-dipole array; PDP_In = pole-dipole array with remote electrode in-line direction; PDP_P = pole-dipole array with remote electrode perpendicular to the profile direction; _PL and _PHQ = see text above; SCHL = Schlumberger array and DPDP = dipole-dipole array)..... 25

Tab. 4: dU values of profile 1-3 for the pole-dipole array. Minimum and maximum values, mean, standard deviation and median are calculated. (Abbreviations: P1 to P3 = profile 1 to profile 3; PDP = pole-dipole array; _In = remote electrode in-line direction; _P = remote electrode perpendicular to profile direction; _PL and _PHQ = different settings which are explained in the following text)..... 27

Tab. 5: Inversion parameters for the SIRT (simultaneous iterative reconstruction technique). 35

Tab. 6: RMS errors for the RES2DINVx64 inversion steps..... 53

Tab. 7: Major difference of the inversion parameters at profile RW 4. 53

Tab. 8: Times for the time-lapse measurements with the start and end time for each measurement. 66

Tab. 9: Compensated conductivities and measured temperatures for the introduced water of the inner well 4..... 67

Tab. 10: Times for the time-lapse measurements with the start and end time for each measurement at profile RW 1..... 73

Tab. 11: Times for the time-lapse measurements with the start and end time for each measurement at profile RW 6..... 76

Tab. 12: Statistical evaluation for the resistivity values for the profile RW1 to RW9. (Abbreviations: WE = Wenner; SCHL = Schlumberger; DPDP = Dipole-Dipole; PDP = Pole-Dipole). 99

Tab. 13: Statistical evaluation for the measurements errors dU in % for the profile RW1 to RW9. (Abbreviations: WE = Wenner; SCHL = Schlumberger; DPDP = Dipole-Dipole; PDP = Pole-Dipole)..... 100

9 Appendix A

9.1 Tables

Name	Amount of values	min. value [Ohmm]	max. value [Ohmm]	mean [Ohmm]	standard deviation [Ohmm]	median [Ohmm]	amount of neg values
RW1_WE	1614	3,73	99,89	10,68	10,87	6,13	0
RW1_SCHL	1686	1,90	97,29	11,82	11,25	7,49	0
RW1_PDP	1304	3,16	171,40	13,08	13,73	7,81	0
RW2_WE	1615	5,37	535,27	15,94	25,55	11,10	0
RW2_PDP	1645	4,19	902,52	15,45	30,90	9,98	0
RW3_WE	1616	4,69	81,33	15,41	14,59	7,70	0
RW4_WESCHL	2514	-1,40	78,91	12,01	9,06	8,92	1
RW4_WE	1617	4,23	79,67	10,96	7,85	8,65	0
RW4_DPDP	1695	-2,54	109,02	12,23	12,50	8,38	20
RW5_WE	1617	8,26	243,07	19,66	21,03	11,71	0
RW5_SCHL	1763	-5,86	243,26	20,45	21,37	12,09	1
RW5_DPDP	1695	-6,72	389,75	25,46	30,18	11,90	8
RW6_WE	1617	-6213,00	308,01	22,79	159,20	11,48	5
RW6_SCHL	1763	-52,58	312,30	28,97	36,42	14,80	10
RW7_WE	1617	4,64	201,78	18,89	21,95	11,03	0
RW7_SCHL	1763	-1,99	229,84	20,37	23,49	12,11	1
RW7_DPDP	1695	-7,72	322,71	25,26	34,81	12,91	3
RW8_WE	1617	3,99	446,46	21,12	42,67	6,69	0
RW8_SCHL	1763	2,60	421,76	22,95	44,01	7,63	0
RW9_WE	1617	2,08	264,70	20,70	33,71	7,08	0

Tab. 12: Statistical evaluation for the resistivity values for the profile RW1 to RW9. (Abbreviations: WE = Wenner; SCHL = Schlumberger; DPDP = Dipole-Dipole; PDP = Pole-Dipole).

Name	dU min. value [%]	dU max. value [%]	dU mean [%]	dU standard deviation [%]	dU median [%]	values above 2% dU	values equal 0% dU
RW1_WE	0	5,86	0,32	0,50	0,15	20	22
RW1_SCHL	0	4,98	0,62	0,80	0,32	84	16
RW1_PDP	0	4,94	0,53	0,85	0,14	73	47
RW2_WE	0	4,21	0,37	0,37	0,34	15	3
RW2_PDP	0	4,98	0,40	0,70	0,16	64	32
RW3_WE	0	3,50	0,35	0,33	0,31	9	10
RW4_WESCHL	0	138,76	0,45	2,95	0,20	19	46
RW4_WE	0	3,61	0,22	0,33	0,12	3	35
RW4_DPDP	0	1423,14	3,68	37,30	0,30	316	72
RW5_WE	0	2,62	0,27	0,33	0,14	1	22

RW5_SCHL	0	1325,87	1,22	31,56	0,27	24	21
RW5_DPDP	0	3899,05	5,22	96,28	0,28	307	66
RW6_WE	0	34,41	0,56	1,33	0,24	36	14
RW6_SCHL	0	114,90	0,84	3,75	0,29	92	20
RW7_WE	0	3,33	0,26	0,40	0,11	6	38
RW7_SCHL	0	519,47	0,78	12,38	0,21	48	36
RW7_DPDP	0	1133,82	3,85	35,58	0,21	296	47
RW8_WE	0	4,87	0,29	0,41	0,14	5	26
RW8_SCHL	0	28,51	0,63	1,27	0,28	64	26
RW9_WE	0	11,85	0,25	0,46	0,12	6	31

Tab. 13: Statistical evaluation for the measurements errors dU in % for the profile RW1 to RW9. (Abbreviations: WE = Wenner; SCHL = Schlumberger; DPDP = Dipole-Dipole; PDP = Pole-Dipole).

9.2 Figures

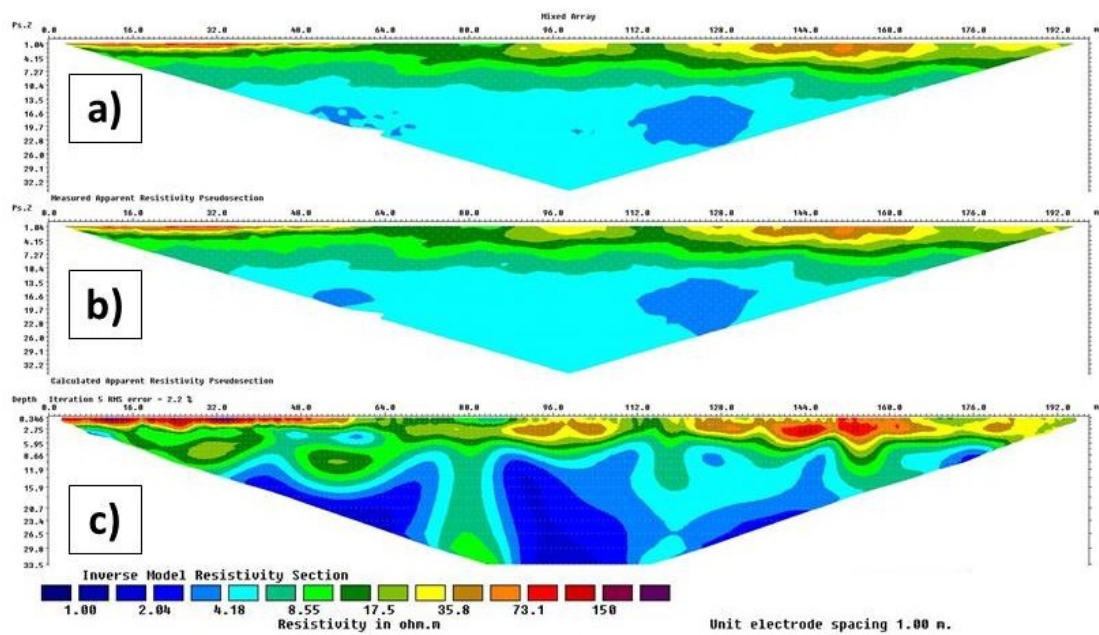


Fig. 57: (a) measured apparent resistivity pseudosection, (b) calculated apparent resistivity pseudosection and (c) inverse model resistivity section of profile RW 1.

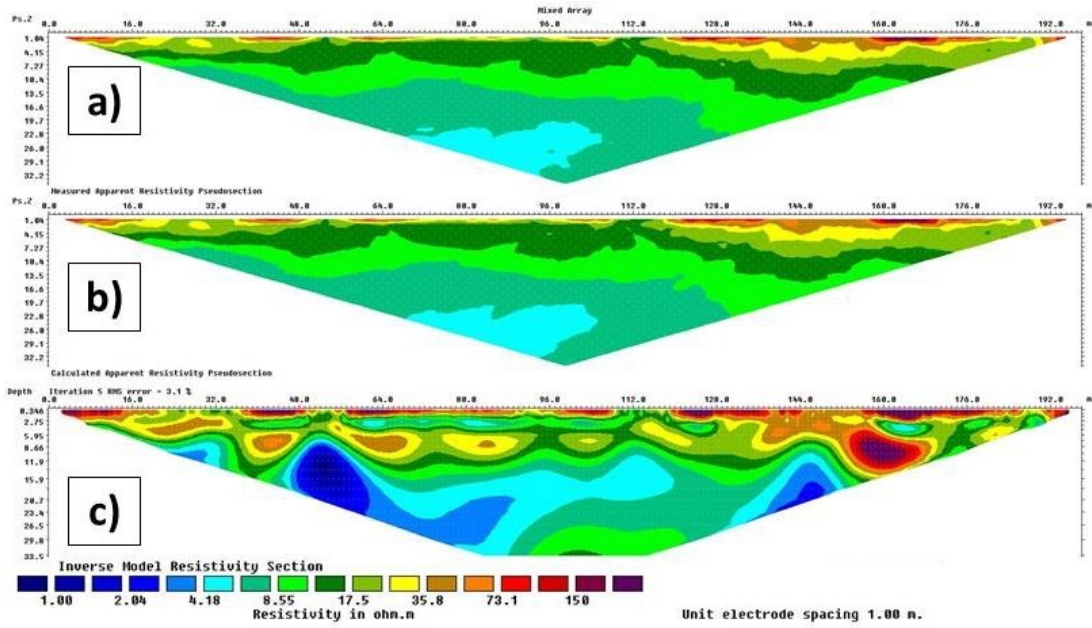


Fig. 58: (a) measured apparent resistivity pseudosection, (b) calculated apparent resistivity pseudosection and (c) inverse model resistivity section of profile RW 2.

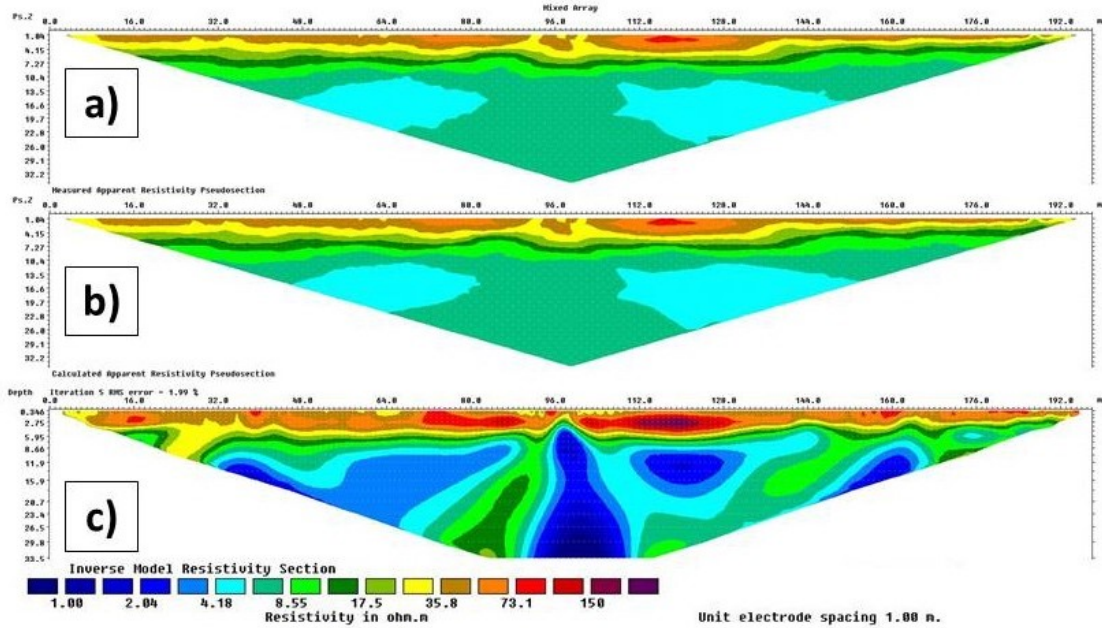


Fig. 59: (a) measured apparent resistivity pseudosection, (b) calculated apparent resistivity pseudosection and (c) inverse model resistivity section of profile RW 3.

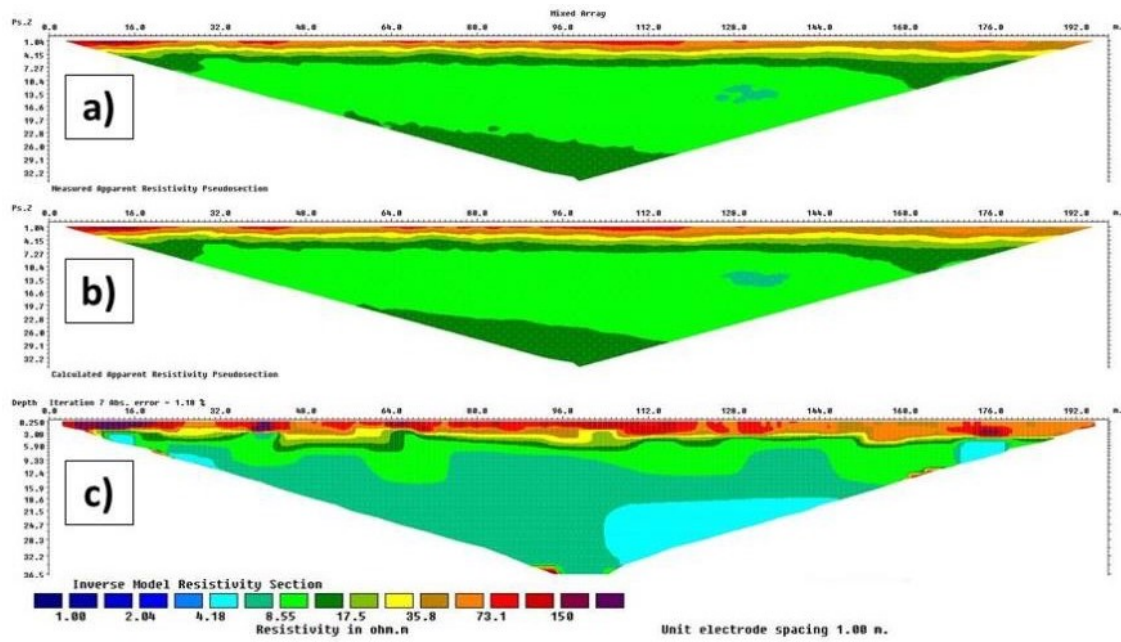


Fig. 60: (a) measured apparent resistivity pseudosection, (b) calculated apparent resistivity pseudosection and (c) inverse model resistivity section of profile RW 5.

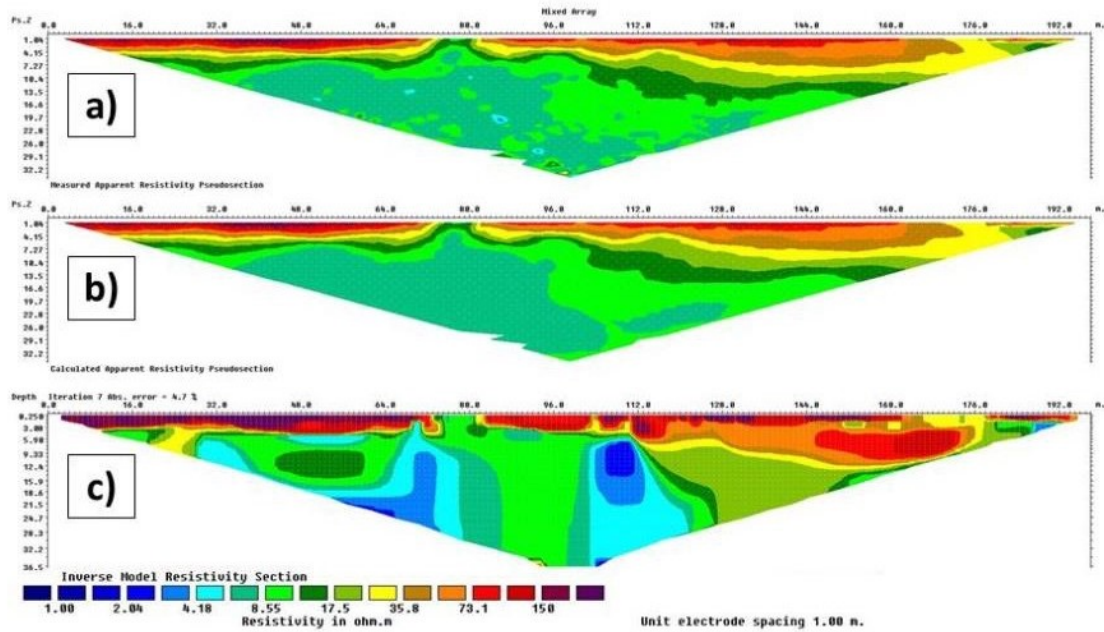


Fig. 61: (a) measured apparent resistivity pseudosection, (b) calculated apparent resistivity pseudosection and (c) inverse model resistivity section of profile RW 6.

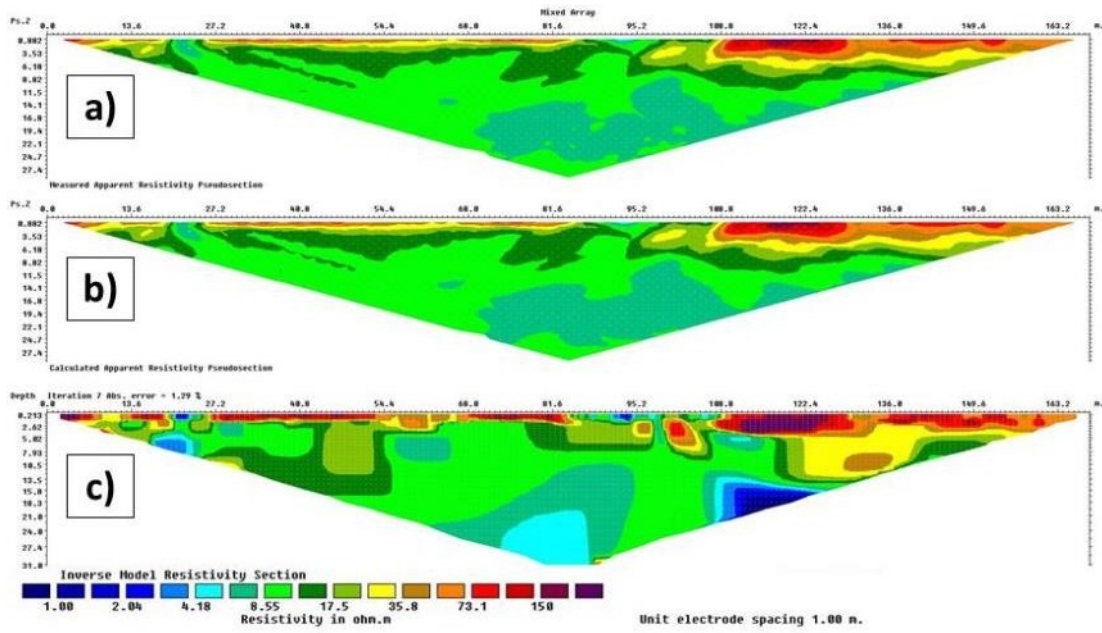


Fig. 62: (a) measured apparent resistivity pseudosection, (b) calculated apparent resistivity pseudosection and (c) inverse model resistivity section of profile RW 7.

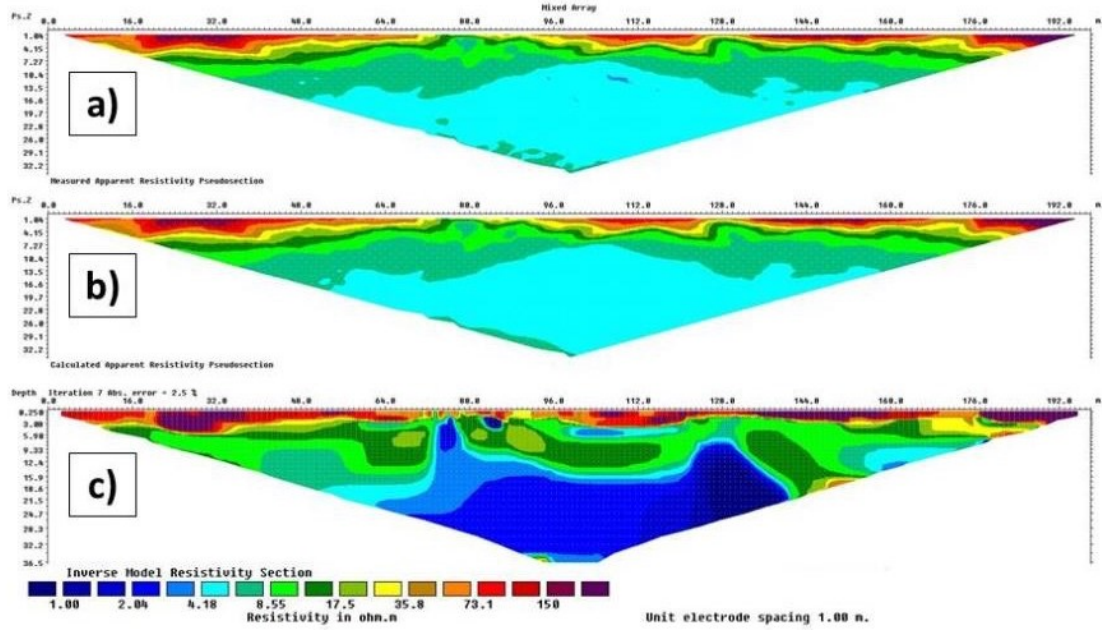


Fig. 63: (a) measured apparent resistivity pseudosection, (b) calculated apparent resistivity pseudosection and (c) inverse model resistivity section of profile RW 8.

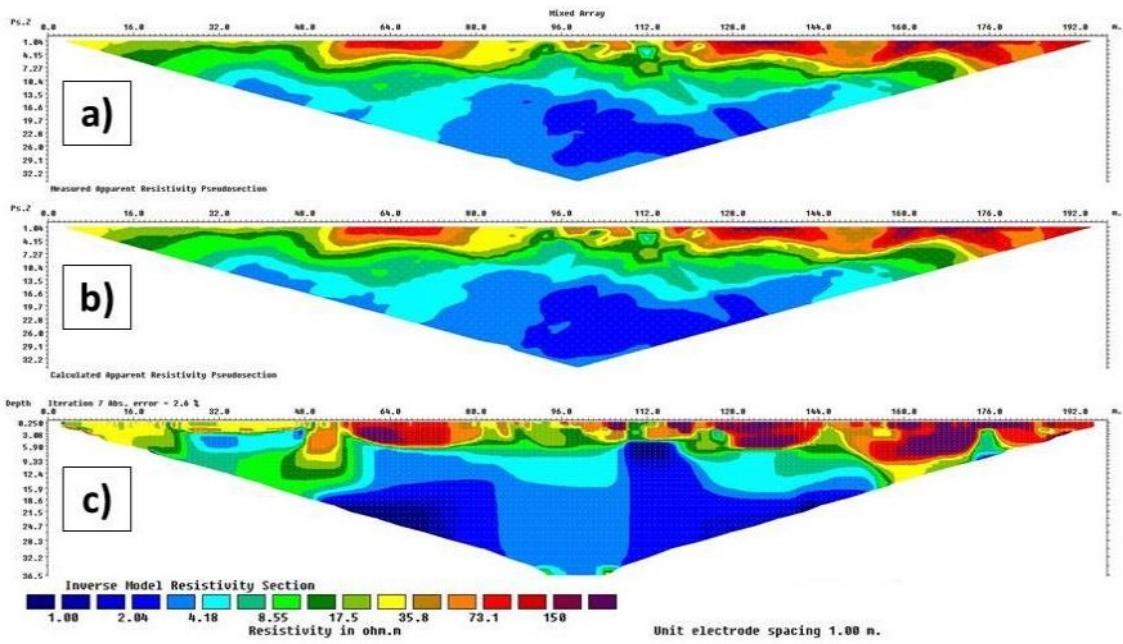


Fig. 64: (a) measured apparent resistivity pseudosection, (b) calculated apparent resistivity pseudosection and (c) inverse model resistivity section of profile RW 9.

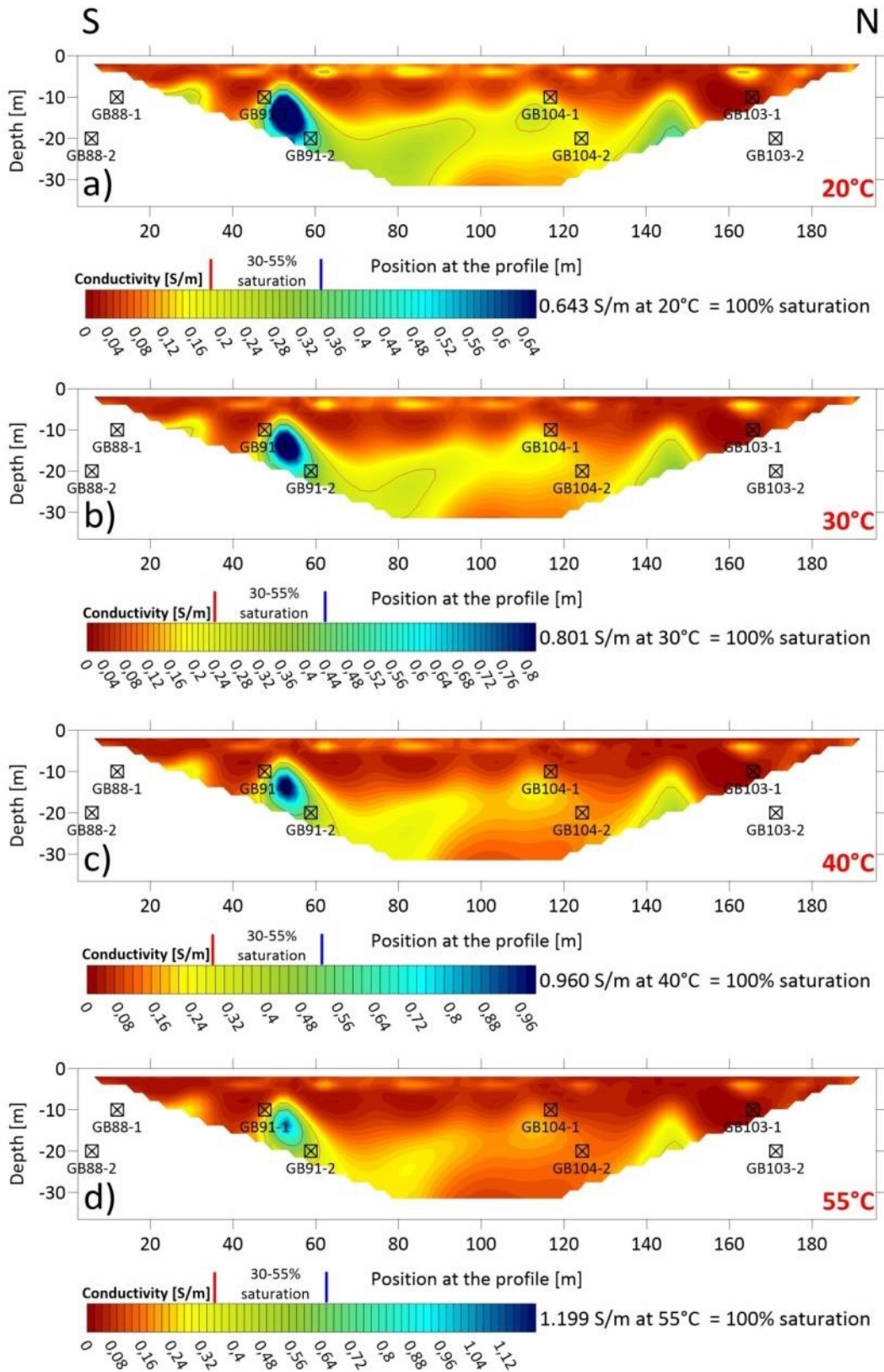


Fig. 65: Variation of the conductivity [S/m] along the profile RW 2 with conductivity scaling at (a) 20 °C, (b) 30 °C, (c) 40 °C and (d) 55 °C. The maximum value of the conductivity corresponds to 100% water saturation and a conductivity of 0 S/m equates to a water content of 0%. The black squares mark the position of the gas wells where the depths represent the mean depth of the steel filter pipe.

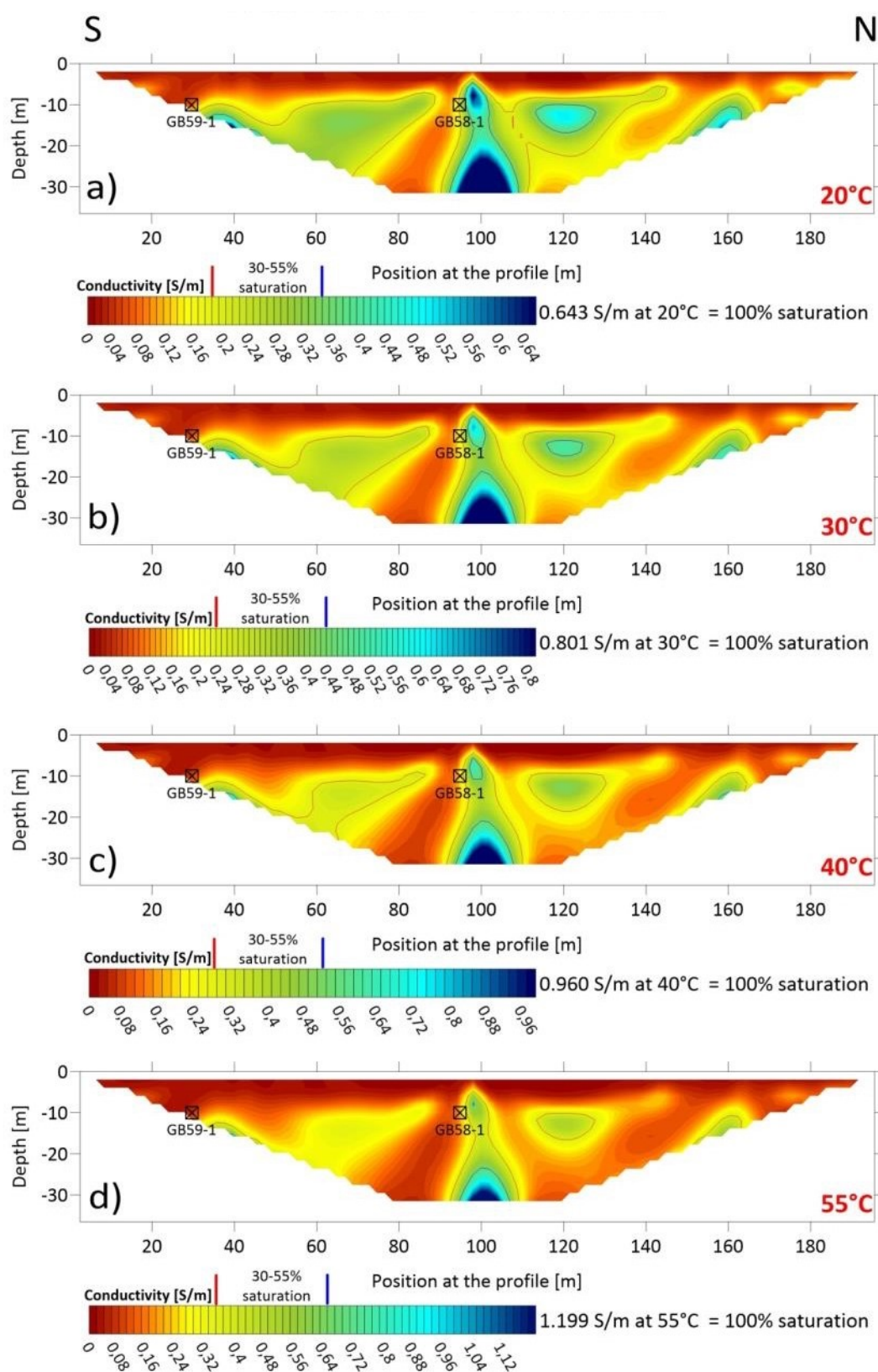


Fig. 66: Variation of the conductivity [S/m] along the profile RW 3 with conductivity scaling at (a) 20 °C, (b) 30 °C, (c) 40 °C and (d) 55 °C. The maximum value of the conductivity corresponds to 100% water saturation and a conductivity of 0 S/m equates to a water content of 0%. The black squares mark the position of the gas wells where the depths represent the mean depth of the steel filter pipe.

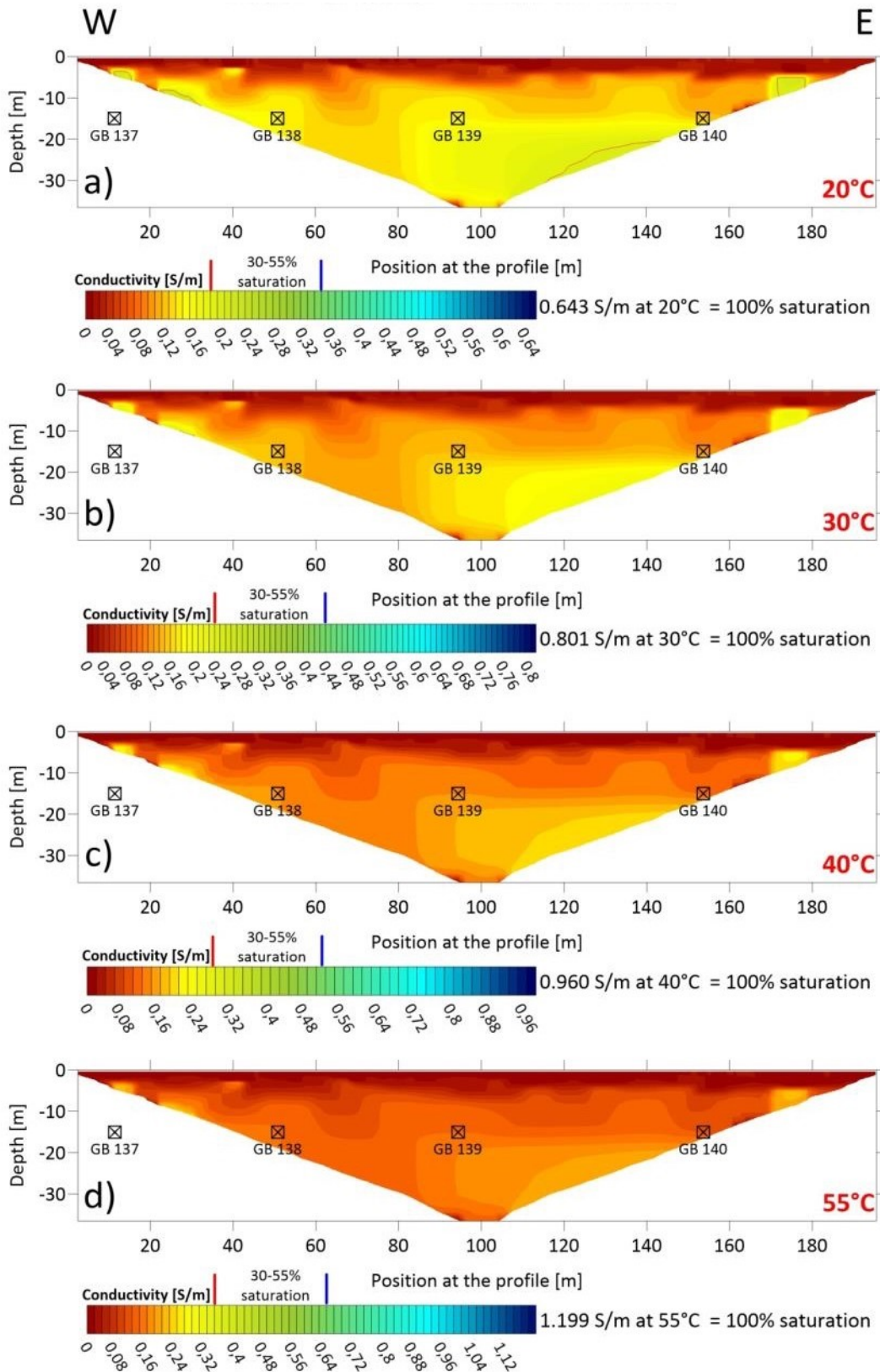


Fig. 67: Variation of the conductivity [S/m] along the profile RW 5 with conductivity scaling at (a) 20 °C, (b) 30 °C, (c) 40 °C and (d) 55 °C. The maximum value of the conductivity corresponds to 100% water saturation and a conductivity of 0 S/m equates to a water content of 0%. The black squares mark the position of the gas wells where the depths represent the mean depth of the steel filter pipe.

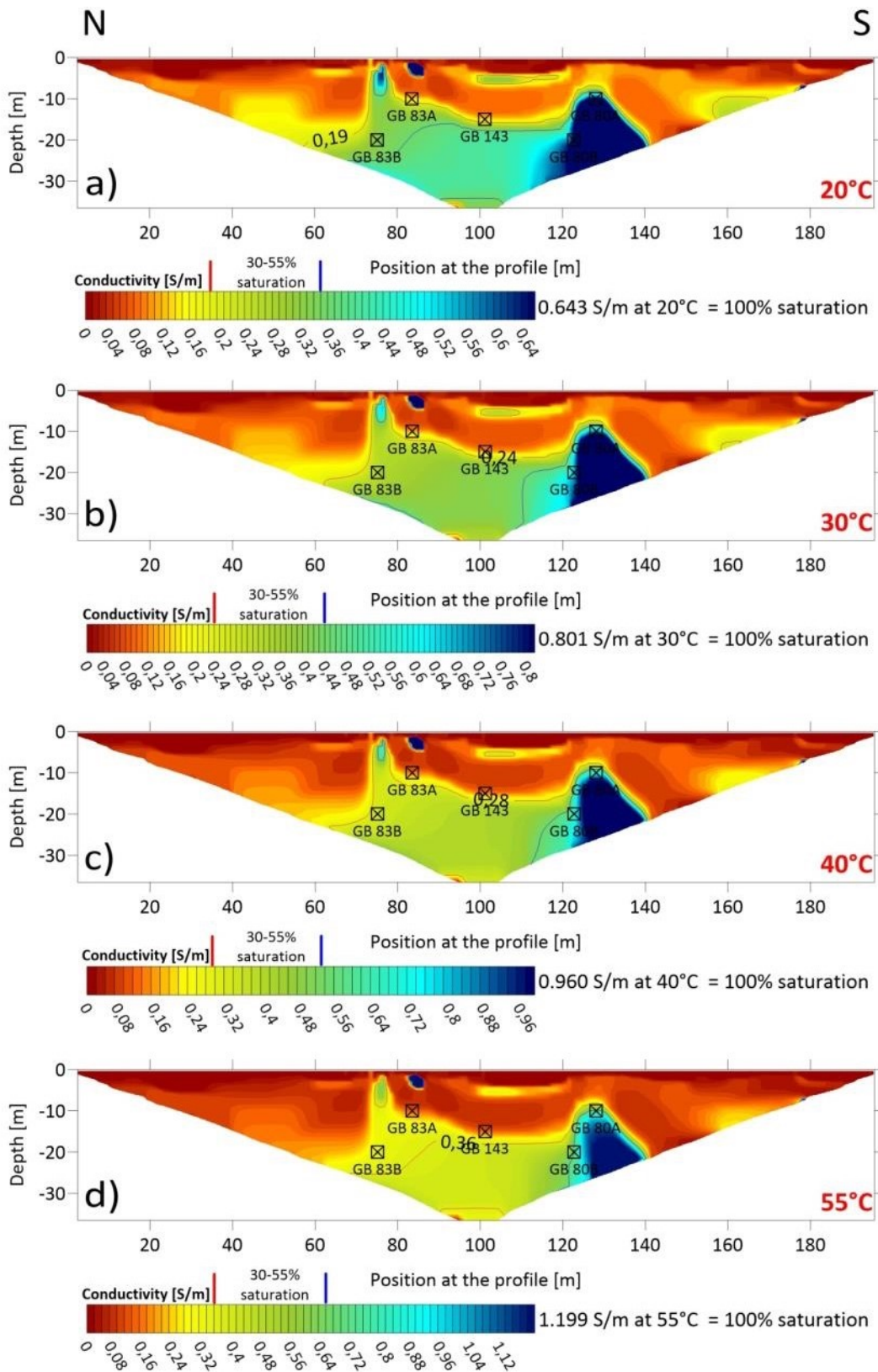


Fig. 68: Variation of the conductivity [S/m] along the profile RW 8 with conductivity scaling at (a) 20 °C, (b) 30 °C, (c) 40 °C and (d) 55 °C. The maximum value of the conductivity corresponds to 100% water saturation and a conductivity of 0 S/m equates to a water content of 0%. The black squares mark the position of the gas wells where the depths represent the mean depth of the steel filter pipe.

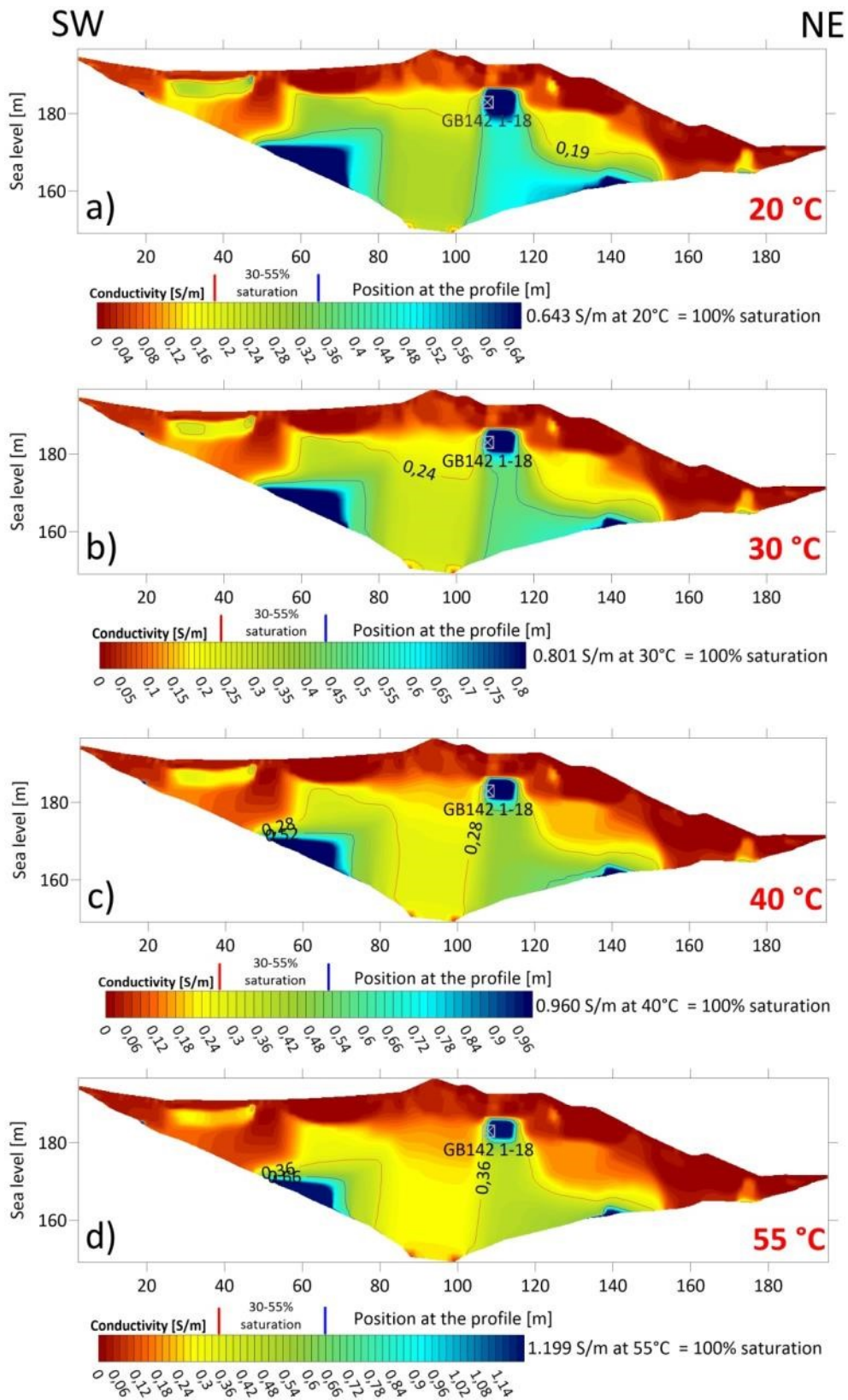


Fig. 69: Variation of the conductivity [S/m] along the profile RW 9 with conductivity scaling at (a) 20 °C, (b) 30 °C, (c) 40 °C and (d) 55 °C. The maximum value of the conductivity corresponds to 100% water saturation and a conductivity of 0 S/m equates to a water content of 0%. The black squares mark the position of the gas wells where the depths represent the mean depth of the steel filter pipe.